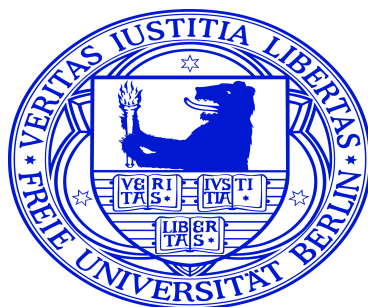


# Molecular Symmetry, Quantum Chemistry and Dynamics: Simulation of Laser Driven Molecular Torsion in the Presence of a Conical Intersection

INAUGURAL- DISSERTATION  
to obtain the academic degree  
Doctor rerum naturalium (Dr. rer. nat.)  
submitted to the Department of Biology, Chemistry and  
Pharmacy  
of Freie Universität Berlin

by  
**Salih J. I. Al-Jabour**  
from Hebron, Palestine



2011



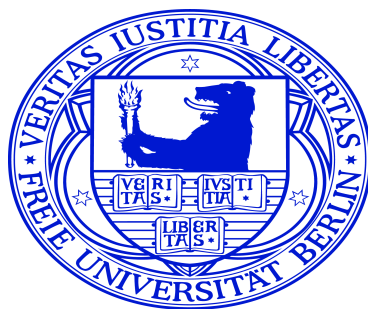
Erstgutachter : Prof. Dr. Jörn Manz  
Zweitgutachter : Prof. Dr. Leticia González  
Tag der Disputation : 16.2.2011



# Molekülsymmetrie, Quantenchemie und Dynamik: Modellsimulationen zur laser-induzierten Torsion in Anwesenheit von konischen Durchschneidungen

INAUGURAL- DISSERTATION  
zur Erlangung des Doktorgrades  
der Freien Universität Berlin  
Fachbereich Biologie, Chemie, Pharmazie

vorgelegt von  
**Salih J. I. Al-Jabour**  
aus Hebron, Palästina



2011



# Publication

*Molecular symmetry properties of conical intersections and non-adiabatic coupling terms: Theory and quantum chemical demonstration for cyclopenta-2,4-dienimine  $C_5H_4NH$ .*

Al-Jabour, S., Baer, M., Deeb, O., Leibscher, M., Manz, J., Xu, X., Zilberg, S., J. Phys. Chem. A. (2010) 114, 2991-3010.





# Abstract

Conical intersections (CIs) and the related non-adiabatic coupling terms (NACTs) are essential for the description of radiation-less processes involved in photochemistry. It was found that the molecular symmetry imposes constraints on CIs, NACTs and the transition dipole moments with respect to symmetry-adapted coordinates. These have consequences for ab initio quantum chemistry calculations of the NACTs, transition dipole moments and for the non-adiabatic reaction dynamics which is mediated by the NACTs. In this study, a new combination is presented of the three fields of research: quantum chemistry, quantum dynamics and theory of the molecular symmetry groups. This combination shows the importance of the molecular symmetry of the CIs, NACTs and transition dipole moments for the photo-induced nuclear dynamics. These investigations are demonstrated for the cis-trans isomerization of the model system Cyclopenta-2,4-Dienimine ( $C_5H_4NH$ ) which has  $C_{2v}(M)$  molecular symmetry, by photo-induced torsion of the H-atom versus the  $C_5H_4N$  fragment around the CN axis.



# Kurzfassung

Konische Durchschneidungen und die zugehörigen nicht-adiabatischen Kopplungsterme sind wesentliche Bestandteile bei der Beschreibung strahlungsloser Vorgänge in der Photochemie. In der vorliegenden Arbeit wird gezeigt, dass die molekulare Symmetrie Bedingungen an die Form der konischen Durchschneidungen, die nicht-adiabatischen Kopplungsterme und die Übergangsdipolmomente stellt. Diese wirken sich auf die quantenchemischen ab-initio-Berechnungen der nichtadiabatischen Kopplungsterme und der Übergangsdipolmomente sowie auf die nichtadiabatische Reaktionsdynamik aus, welche durch die Kopplungsterme beeinflusst wird. In dieser Arbeit werden drei Forschungsfelder kombiniert: Quantenchemie, Quantendynamik und Theorie der molekularen Symmetriegruppen. Diese Kombination begründet die Bedeutung der molekularen Symmetrie der konischen Durchschneidungen, der nichtadiabatischen Kopplungsterme und der Übergangsdipolmomente für die lichtinduzierten Kerndynamik. Die Untersuchungen erstrecken sich auf die cis-trans-Isomerisierung des Modelemoleküls Cyclopenta-2,4-dienimin ( $C_5H_4NH$ ), das zur molekularen Symmetriegruppe  $C_{2v}(M)$  gehört, durch lichtinduzierte Torsion des H-Atoms gegenüber dem  $C_5H_4N$ -Fragment um die CN-Achse.



# Acknowledgement

*I would like to express my deep and sincere gratitude to **Prof. Jörn Manz**. Your wide knowledge and your logical way of thinking have been of great value for me. Your perpetual energy and enthusiasm in research had motivated all your students, including me. In addition, you were always accessible and willing to help your students with their research. As a result, research life became smooth and rewarding for me.*

*I am deeply grateful to **Dr. Monika Leibscher** for her detailed and constructive comments, and for her important support throughout this work. Your kind guidance have been of great value in this study. It helped me in all the time of research and writing of this thesis.*

*I wish to express my sincere thanks to **Prof. Omar Deeb** for introducing me to the field of quantum chemistry. Your guidance and support was so important for me to continue this study.*

*I owe my most sincere gratitude to **Prof. Michael Baer**, your extensive discussions around my work and interesting explorations have been very helpful for this study. Also my great thanks go to **Prof. Shmuel Zilberg** and **Prof. Yehuda Haas** for their help and cooperation.*

*During this work I have collaborated with many colleagues for whom I have great regard, and I wish to extend my warmest thanks to all those who have helped me with my work, especially Steffen Belz, Thomas Grohmann, Shiren Alfalah, Axel Schild, Anatole Kenfack and Doreen Mollenhauer.*

*My thanks go to the Deutsche Forschungsgemeinschaft for the financial support in the frame of trilateral project MA 515/22-2.*

*I owe my loving thanks to **my parents**, for giving birth to me at the first place and supporting me spiritually throughout my life. My grateful thanks go to my brothers and sisters.*



# Contents

<b>1. Introduction</b>	<b>3</b>
<b>2. Models, Methods and Techniques</b>	<b>9</b>
2.1. Born-Oppenheimer Approximation . . . . .	10
2.2. Electronic Schrödinger Equation . . . . .	13
2.2.1. Variational Method and Hartree-Fock Theory . . . . .	13
2.2.2. Basis Sets . . . . .	16
2.2.3. Post Hartree-Fock Method . . . . .	17
2.2.4. Multi-Configuration Self Consistent Field (MCSCF) . . . . .	18
2.2.5. Complete Active Self Consistent Field (SCF) . . . . .	18
2.3. Conical Intersections (CIs) and Non-Adiabatic Coupling Terms (NACTs) .	19
2.4. Quantum Chemical Calculation of the NACTs . . . . .	21
2.5. Adiabatic-to-Diabatic Transformation (ADT) . . . . .	23
2.6. Interaction of Molecules with a Laser Field . . . . .	26
2.7. Numerical Methods for the Solution of the Nuclear Schrödinger Equation .	29
2.7.1. Solution of the Nuclear TISE: Fourier-Grid-Hamiltonian Method . .	29
2.7.2. Solution of the Nuclear TDSE: Split Operator Method . . . . .	32
2.8. Molecular Symmetry (MS) . . . . .	35
<b>3. The Model System</b>	<b>39</b>
3.1. Cyclopenta-2,4-dienimine $C_5H_4NH$ . . . . .	40
3.2. Quantum Chemistry of $C_5H_4NH$ . . . . .	41
<b>4. Quantum Chemistry and Molecular Symmetry Effects of <math>C_5H_4NH</math></b>	<b>45</b>
4.1. Introduction . . . . .	46
4.2. The Molecular Symmetry Group of Cyclopenta-2,4-dienimine . . . . .	47
4.3. Defining the Symmetry-adapted Nuclear Coordinates . . . . .	51
4.4. Calculating the Potential Energy Surfaces of $C_5H_4NH$ . . . . .	53
4.5. Symmetry of the NACTs . . . . .	57
4.5.1. Assigning the IREPs of NACTs . . . . .	65
4.5.2. Calculating the NACTs of $C_5H_4NH$ . . . . .	74
4.5.3. Assignment of the IREPs of NACTs of $C_5H_4NH$ . . . . .	77
4.6. Adiabatic-to-diabatic Transformation (ADT) . . . . .	78

---

4.7. Conclusion . . . . .	82
<b>5. Molecular Symmetry Effects and Non-adiabatic Nuclear Dynamics: Simulation of Photo-Induced Torsion of C<sub>5</sub>H<sub>4</sub>NH</b>	<b>85</b>
5.1. Introduction . . . . .	86
5.2. PES and the Related Non-adiabatic Coupling Terms of C <sub>5</sub> H <sub>4</sub> NH: Comparison between two cases . . . . .	86
5.3. Assigning the IREPs of the Transition Dipole Moments . . . . .	91
5.4. Photo-Excitation and Molecular Symmetry of the Initial Wavepacket . . .	93
5.5. Effect of the IREPs of the NACTs and Transition Dipoles on the Radiation-less Decay . . . . .	97
5.5.1. Isotope Effect on Radiation-less Decay . . . . .	97
5.5.2. Effects of the Symmetry of the Initial Wavefunctions . . . . .	99
5.5.3. Effects of the IREPs of the NACTs and Transition Dipole Moments	102
5.6. Interaction with a Laser Field . . . . .	110
5.7. Dipole Moments and Transition Dipole Moments . . . . .	112
5.8. Effect of Laser Pulse Parameters on Excitation . . . . .	115
5.9. Effects of the IREPs of the NACTs, Dipole and Transition Dipole Moments in Laser Pulse Induced Radiation-less Decay . . . . .	117
5.10. Radiation-less Decay in Diabatic and Adiabatic Representation . . . . .	120
5.11. Conclusion . . . . .	125
<b>6. Summary</b>	<b>127</b>
<b>Appendix:</b>	
<b>A. Appendix A</b>	<b>131</b>
<b>Bibliography</b>	<b>133</b>



# 1. Introduction

Photochemistry is the study of chemical changes made possible by energy of light. The first observation of a photochemical reaction was described by Trommsdorf in 1834 [1], when he noticed that  $\alpha$ -santonin crystals turn to yellow and burst when they are exposed to light. Nature involves a lot of fundamental processes which are triggered by photochemical reactions. Perhaps the most important photochemical reaction is photosynthesis where carbon dioxide and water are converted into starch. This process depends on the absorption of sunlight by chlorophyll in the leaves. The net result is that the energy absorbed is stored as chemical energy in the starch. In photochemical reactions, light can be either in the reactant, i.e. light absorption, or product (emission of light as fluorescence and phosphorescence or light transferred to another molecule or atom). When a molecule absorbs light, it enters an excited state whose physical and chemical properties differ from the initial state. The excited state then changes by reacting with other molecules or gives off its extra energy. The complete understanding of photochemical reactions and the abilities to control them will help to design artificial experimental photochemical systems mimicking the natural ones, such as motors, machines and switches in nano scale. Photochemical reactions involve electronic reorganization initiated by electromagnetic radiation. The reactions proceed on typical time scales from tens of femtoseconds ( $1\text{fs} = 10^{-15}\text{s}$ ) to picoseconds ( $1\text{ps} = 10^{-12}\text{s}$ ). These reactions are several orders of magnitude faster than thermal reactions. Contrary to thermal reactions, which proceed on a single potential energy surface, photochemical reactions involve at least two.

The Born-Oppenheimer approximation is the keystone to the visualization of chemical processes. It enables to picture molecules as a set of nuclei moving along a potential energy surface (PES) provided by the electrons. However, whereas the validity of the Born-Oppenheimer approximation for many chemical systems is not in doubt, it is now clear that in many other important cases the approximation breaks down [2, 3]. That is to say, the nuclear and electronic motions are coupled. This is mostly common in the photochemistry of polyatomic molecules where a large number of energetically close-lying electronic states and many nuclear degrees of freedom are involved. An important example of the result of coupling between nuclei and electrons is a conical intersection (CI) between electronic states, see Fig.1.1. Many investigations show that the most efficient transition from one electronic state to another is at a conical intersection. Perhaps the

earliest examples for the importance of coupling between the electronic states were found during the 1930s. In 1934 Renner wrote about the non-adiabatic coupling in electronically excited states in  $\text{CO}_2$  [4]. Teller in 1937 [5], showed that conical intersections are very important for the non-radiation decay in photochemical reaction, without performing any quantum dynamical simulation. He already discussed the possibility that one can "get a transition in a short time" by internal conversion via a conical intersection. Moreover, in a semi-classical framework L. Landau [7] and C. Zener [8] quantified the fast radiation-less decay that occur at a CI. The first quantum dynamics simulation of internal conversion via conical intersection was carried out by Köppel et al. [9], demonstrating internal deactivation on the sub-100-fs time scale. Since then, CIs known to provide ultrafast important mechanism for many photo-chemical reactions [10]. One area in which conical intersections are important is in biological systems. Nonadiabatic processes are common in photobiology, affecting essential processes, such as photosynthesis, light harvesting, vision and in the photochemical damage and repair of DNA [12]. For example, the stability of DNA with respect to the UV irradiation is due to such conical intersection [12, 13]. This comes from the very important role they play in non-radiative de-excitation transitions, where a molecular wavepacket which is excited to some excited electronic state by the UV photon follows the slope of the potential energy surface (PES) and reaches the conical intersection, see Fig.1.1. At this point the strong non-adiabatic coupling terms induces a non-radiative transition which leads the molecule back to its electronic ground state [14].

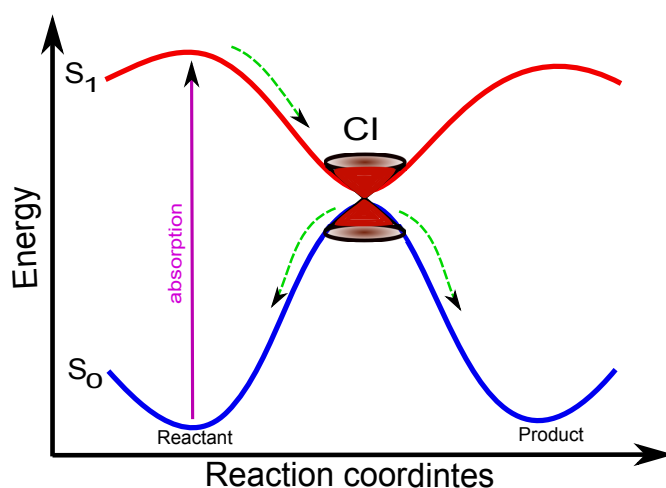


Figure 1.1.: Schematic view of the radiative excitation and its deactivation via conical intersection between the electronic states  $S_0$  and  $S_1$ . The arrows visualize the motion of a nuclear wavepacket.

---

A full understanding of photochemical reactions requires the knowledge about:

- 1- The location of the conical intersections.

The conical intersections are the set of molecular geometry points where the two potential surfaces of the same spatial irreducible representation and spin state intersect (see Fig.1.1). As a consequence, to give a precise explanation of photochemical reactions it is important to localize these conical intersections. Herzberg and Longuet-Higgins [15, 16] pointed out that the electronic wave function changes its sign when transported along a closed loop around a CI. This phase-change theorem is applied to localize the conical intersection in many system. This model, developed by Haas and Zilberg [17, 18], is one of several methods for locating the conical intersections and has been used to explain many different reactions. For this purpose the stationary points, i.e. the minima and transition states in the electronic ground states are considered as so called anchors. Each Longuet-Higgins (LH) loop consists of a unique pair of reaction paths from reactant via one of the transition states to the product. According to this model, a single CI exists within any LH-loop if the electronic wavefunction changes its sign when the system goes around the closed loop. Then the CIs can be located by interpolation of paths which connect the anchors of the surrounding LH loop [17, 18].

- 2- The potential energy surfaces (PES) and the non-adiabatic coupling terms (NACTs) which couple the potential energy surfaces.

The derivative coupling that couples two different electronic states is inversely proportional to the energy difference between the two electronic states [3]. Therefore, the smaller the energy difference, the larger the coupling. This phenomenon is a result of the break down of the Born-Oppenheimer approximation, where it is assumed that the non-adiabatic coupling terms are zero. So it is necessary to calculate these coupling terms for non Born-Oppenheimer processes, in particular if conical intersections are involved. The determination of the properties of conical intersections requires a high level of quantum chemical calculations of PESs and non-adiabatic coupling terms (NACTs), which are now possible by modern programs based on quantum chemistry [19, 20, 21, 22]. A common approach to determine the strength of coupling elements is the multi-mode vibronic coupling method, where the diabatic coupling are modelled by linear or higher order functions of the nuclear coordinates [23, 24, 25, 26]. The coupling elements can also be obtained by a quasi-diabatization procedure from the adiabatic potential energies [27, 28, 29]. Ab initio calculations of the non-adiabatic coupling terms which appear in the adiabatic representation of the molecular Hamiltonian have also been employed for the simulation and control

of non-adiabatic nuclear dynamics in the adiabatic representation [30, 31]. Accurate methods to calculate NACTs have now been implemented in quantum chemical packages like MOLPRO [32].

At conical intersection, the NACTs have poles, i.e. they approach infinity. The singularity of the NACTs at the CIs makes simulation of nuclear dynamics on coupled electronic states very difficult in the adiabatic representation. In order to remove these singularities an adiabatic-to-diabatic transformation (ADT) is applied [3, 10, 11, 33]. Moreover, the NACTs must fulfil quantization rules [3], i.e. the contour integrals of the NACTs evaluated along closed loops around a individual CI between two electronic states have to be equal to  $\pm\pi$ . The numerical agreement of the NACTs with these quantization rules in many systems demonstrate the quantum chemical accuracy in the calculations of the NACTs [3, 33, 34].

### 3- Quantum dynamics of the nuclear wavepackets on coupled surfaces.

A complete understanding of photochemical reactions requires a knowledge about the dynamics of the nuclear wavepackets evolving on the coupled PESs. The simulation of wavepacket dynamics requires quantum chemistry calculation of the transition dipole moments in order to evaluate the initial photo-excitation [2]. Since the 1980s, methods for time-dependent wavepackets have been employed to explore the quantum dynamics in the presence of conical intersection, both with ab initio based model and with simplified generic model Hamiltonians [23, 24]. Quantum dynamics make it possible to investigate for example photo-dissociation [2, 37, 38] and photo-isomerization [39, 40] processes. A prominent example is the isomerization around a C=C double bond [41]. The quantum dynamical simulations of photochemical reactions via conical intersections serve as a basis for developing methods for their control using special designed laser pulses. Numerical exact technique for quantum dynamics of nuclear wavepackets does not allow to simulate polyatomic photochemical in full dimensionality. As a consequence, the reaction dynamics is often simulated using models with reduced dimensionalities [10, 36].

### 4- Symmetry of the conical intersections and NACTs.

Longuet-Higgins [42] has pointed out that a powerful way of treating molecular symmetry properties begins not with the traditional concept of molecular point groups, but rather with concepts associated with the exchange of identical particles. The molecular symmetry operations are the operations that leave the Hamiltonian of the system invariant. This consists of the inversion of all nuclear and electronic coordinates and of the feasible permutations of identical nuclei [43, 44] and thus determines

equivalent configurations of a molecule. The molecular symmetry is a fundamental concept in chemistry, since it can predict or explain many chemical properties of a molecule such as selection rule for spectroscopic transition [43]. Moreover, by exploring the symmetry of a molecule one can simplify quantum chemical calculations. The relative phase of the electronic wavefunctions and thus the sign of the NACTs is, however, not easily obtained by traditional quantum chemistry methods. For symmetric molecules, which have several conical intersections, this phase can play an important role: The electronic wavefunctions and the NACTs transform according to the irreducible representations of the molecular symmetry of the molecule, which determines by the phase of the wavefunctions. We should emphasize here the difference between the molecular symmetry of an electronic state, which describes its global symmetry with respect to the nuclear coordinates, and the molecular point group which determines the local symmetry of an electronic wavefunction at a given nuclear configuration.

The goal of this thesis is to develop methods in order to determine the symmetry of the CIs and the related NACTs with the help of a combination of molecular symmetry and quantum chemical methods. Moreover, the importance of molecular symmetry for photo-induced nuclear dynamics is demonstrated with the help of quantum dynamics simulations. To achieve these aims, the photo-induced torsion around CN-bond of  $C_5H_4NH$  is considered as an example.

This work is sectioned into the main parts: First, the theoretical concepts used in this thesis are briefly summarized. The second part contains the assignment of the molecular symmetry of the conical intersections and related non-adiabatic coupling terms. Third, we investigate the effect of the irreducible representations (IREPs) of the NACTs on the nuclear dynamics. This is done by investigating the photo-induced cis-trans isomerization of  $C_5H_4NH$  by studying the H-atom movement on coupled electronic states. In more details, the structure of this thesis is as follows:

**CHAPTER 2** includes the theoretical concepts of quantum chemistry and quantum dynamics of isolated molecules. It provides a definition of conical intersections and non-adiabatic coupling terms. Quantum chemical approaches to calculate the PESs and NACTs are introduced. Also, all numerical methods used to solve the nuclear Schrödinger equation are presented. Moreover, the interaction between laser field and molecule are discussed. Finally, the chapter includes an introduction to the concept of the molecular symmetry.

**CHAPTER 3** includes a brief presentation of the model system,  $C_5H_4NH$  and its properties.

**CHAPTER 4:** In this chapter, we introduce the molecular symmetry properties of the CIs and the related NACTs in molecules with large amplitudes motion such as torsion, focusing on groups with only one-dimensional irreducible representation. These foundations are important for applications, e.g. we will show that locating one CI and the assignments of its IREPs generate automatically the complete set of analogous CIs at symmetry-related locations. Then, we present the PESs and related non-adiabatic coupling terms calculated using ab initio quantum chemical methods for the model system  $C_5H_4NH$  for three couple electronic states. Finally, this chapter is completed by calculating the adiabatic-to-diabatic transformation matrix which is applied to transform the adiabatic potentials and non-adiabatic coupling elements into a diabatic presentation.

**CHAPTER 5:** The CIs, NACTs and dipole and transition dipole moments which appear in the nuclear Schrödinger equation, determine the photo-induced process of a given system. The knowledge of symmetry properties should thus be important for adequate predictions of the non-adiabatic reaction dynamics, including interferences. In this chapter, we present the investigations of the effect of the molecular symmetry and the corresponding irreducible representations of the non-adiabatic coupling terms and transition dipole moments on photo-induced nuclear dynamics, with application to radiation-less decay and intra-molecular torsion. This chapter contains two parts for the quantum dynamics without and with considerations of the laser pulses.

**CHAPTER 6** includes the summery of this study and the conclusions.

## **2. Models, Methods and Techniques**

This chapter includes a brief description of the theoretical methods and techniques used to achieve the goals stated in the introduction. The total non-relativistic time-dependent Schrödinger equation (TDSE) will be separated into two parts: namely the electronic TISE and the nuclear TDSE. *Ab initio* quantum chemistry methods will be used to solve the electronic time-independent Schrödinger equation (TISE). The methods used to calculate the non-adiabatic coupling terms (NACTs) and the concept of conical intersections (CI) will be introduced in Section 2.3. The adiabatic-to-diabatic transformation (ADT) is discussed in Section 2.5. In Section 2.6, the interaction between molecules and light will be introduced. Numerical time-dependent and time-independent solution methods will be presented for the nuclear Schrödinger equation in Section 2.7. The last section will include a brief introduction to the molecular symmetry (MS).

## 2.1. Born-Oppenheimer Approximation

The time dependent Schrödinger equation which defines the total time dependent wavefunction  $\psi_{\text{tot}}$  is given by

$$i\hbar\frac{\partial}{\partial t}\psi_{\text{tot}} = H_{\text{tot}}\psi_{\text{tot}} \quad (2.1)$$

Here, the total Hamilton operator  $H_{\text{tot}}$  contains all system information, which for a molecular system consisting of  $N_{\text{el}}$  electrons and  $N_{\text{nuc}}$  nuclei has the form [51],

$$H_{\text{tot}} = T_{\text{el}} + T_{\text{nuc}} + V_{\text{el,el}} + V_{\text{nuc,nuc}} + V_{\text{el,nuc}} \quad (2.2)$$

The kinetic energy of the electrons has the following form

$$T_{\text{el}} = \sum_{j=1}^{N_{\text{el}}} \frac{\vec{P}_{ej}^2}{2m_e}, \quad (2.3)$$

where  $m_e$  is the electron mass, and  $\vec{P}_{ej}$  represents the momentum of the  $j$ -th electron. For the nuclei, the kinetic energy is

$$T_{\text{nuc}} = \sum_{n=1}^{N_{\text{nuc}}} \frac{\vec{P}_n^2}{2M_n}, \quad (2.4)$$



with the nuclear masses  $M_n$ , and nuclear momenta  $\vec{P}_n$ . The Coulomb interaction between the electrons is given in the following form:

$$V_{\text{el,el}} = \frac{1}{4\pi\epsilon_0} \sum_{j=1}^{N_{\text{el}}} \sum_{j<i} \frac{e^2}{|\vec{s}_{ei} - \vec{s}_{ej}|}, \quad (2.5)$$

where  $e$  and  $\vec{s}_e$  are the charge and the position of the electrons, respectively. The Coulomb interaction between the nuclei is

$$V_{\text{nuc,nuc}} = \frac{1}{4\pi\epsilon_0} \sum_{n=1}^{N_{\text{nuc}}} \sum_{n<m} \frac{Z_n Z_m e^2}{|\vec{s}_m - \vec{s}_n|} \quad (2.6)$$

Where  $Z_n e$  and  $\vec{s}_n$  represent the charge and the position of nuclei, respectively. Finally the Coulomb interaction between nuclei and electrons is given by:

$$V_{\text{el,nuc}} = -\frac{1}{4\pi\epsilon_0} \sum_{n=1}^{N_{\text{nuc}}} \sum_{j=1}^{N_{\text{el}}} \frac{Z_n e^2}{|\vec{s}_n - \vec{s}_{ej}|}. \quad (2.7)$$

The solution of the non-relativistic TDSE Eq.(2.1) with this Hamilton operator Eq. (2.2) is a complicated many-body problem. Fortunately, there are ways to simplify the many-body problem by mean of reasonable approximations so that the Schrödinger equation with total Hamiltonian can be solved numerically. The most well-known approximation is called Born-Oppenheimer method [52].

The Born-Oppenheimer approximation is based on the fact that there is a large difference between the masses of the nuclei and electrons, which implies that the nuclear motion is slow compared to the electronic motion [52]. The Born-Oppenheimer approximation simplifies the solution by separating nuclear and electronic motions. The physical picture of Born-Oppenheimer approximation is one where the fast-moving electrons are able to re-adapt instantaneously to new nuclear geometry, as a result of the light electron mass with respect to the nuclear one. Therefore, one first solves the TISE for the electronic Hamiltonian

$$H_{\text{el}} = T_{\text{el}} + V_{\text{el,el}} + V_{\text{el,nuc}} \quad (2.8)$$

with fixed nuclear coordinates. Here,  $H_{\text{el}}$  depends explicitly on the electronic coordinates  $\vec{s}_{e1}, \vec{s}_{e2}, \dots, \vec{s}_{eN_{\text{el}}}$ , while the nuclear coordinates  $\vec{s}_1, \vec{s}_2, \dots, \vec{s}_{N_{\text{nuc}}}$  are parameters.

The task of the quantum chemistry is to solve the associated electronic TISE

$$H_{\text{el}} |\psi_{\text{el}}^i\rangle = E_{\text{el}}^i |\psi_{\text{el}}^i\rangle \quad (2.9)$$

The solution of the electronic TISE Eq.(2.9)(the methods will be presented in the next

section) provides the electronic eigenfunctions or electronic states  $|\psi_{\text{el}}^i\rangle$  as well as the electronic energies  $E_{\text{el}}^i$  for the  $i$ -th electronic state (which will be dropped in next section for simplicity). The total energy of a given electronic state  $i$  with fixed nuclear geometry is equal to the electronic energy plus the nuclear repulsion energy  $V_{\text{nuc,nuc}}$ , i.e.

$$E^i = E_{\text{el}}^i + V_{\text{nuc,nuc}} \quad (2.10)$$

The electronic TISE Eq.(2.9) can be solved for various nuclear geometries, so that the electronic energies  $E_{\text{el}}^i(\vec{s}_1, \vec{s}_2, \dots, \vec{s}_{N_{\text{nuc}}})$  depend on the nuclear coordinates. Also the quantity  $E^i$ , is a function of  $\vec{s}_1, \vec{s}_2, \dots, \vec{s}_{N_{\text{nuc}}}$  and thus can be written as [51, 52]:

$$E^i = E_{\text{el}}^i(\vec{s}_1, \vec{s}_2, \dots, \vec{s}_{N_{\text{nuc}}}) + \frac{1}{4\pi\epsilon_0} \sum_{n=1}^{N_{\text{nuc}}} \sum_{n<m} \frac{Z_m Z_n e^2}{|\vec{s}_m - \vec{s}_n|}. \quad (2.11)$$

The quantity  $E^i$  is called potential energy (hyper)surface (PES) for the  $i$ -th electronic state. The solution of the electronic TISE with given nuclear geometry represent one point of the PES. It will be shown in Section 2.3 that  $E^i$  is the effective potential energy ( $V$ ) for the  $N_{\text{nuc}}$  nuclei and depending on the nuclear positions:

$$E^i(\vec{s}_1, \vec{s}_2, \dots, \vec{s}_{N_{\text{nuc}}}) = V_i(\vec{s}_1, \vec{s}_2, \dots, \vec{s}_{N_{\text{nuc}}}) \quad (2.12)$$

In the Born-Oppenheimer approximation, the nuclei move in the ground electronic state according to the Hamiltonian:

$$H_{\text{nuc}} = T_{\text{nuc}} + V_0(\vec{s}_1, \vec{s}_2, \dots, \vec{s}_{N_{\text{nuc}}}) \quad (2.13)$$

The solution of the nuclear TISE yields the nuclear eigenstate  $|\Phi_{\text{nuc}}^j\rangle$  and eigenenergies  $E_{\text{nuc}}^j$  describing the vibration, rotation and translation of the molecule.

$$H_{\text{nuc}} |\Phi_{\text{nuc}}^j\rangle = E_{\text{nuc}}^j |\Phi_{\text{nuc}}^j\rangle \quad (2.14)$$

Within the Born-Oppenheimer approximation the eigenfunction of the total Hamiltonian Eq. (2.2),  $\Phi_{\text{tot}}^j$  for the electronic ground state ( $j=0$ ) is expressed in the following formula:

$$\begin{aligned} \Phi_{\text{tot}}^0(\vec{s}_1, \vec{s}_2, \dots, \vec{s}_{N_{\text{nuc}}}, \vec{s}_{e1}, \vec{s}_{e2}, \dots, \vec{s}_{eN_{\text{el}}}) &= \Phi_{\text{nuc}}^0(\vec{s}_1, \vec{s}_2, \dots, \vec{s}_{N_{\text{nuc}}}) \\ &\times \psi_{\text{el}}^0(\vec{s}_{e1}, \vec{s}_{e2}, \dots, \vec{s}_{eN_{\text{el}}}, \vec{s}_1, \vec{s}_2, \dots, \vec{s}_{N_{\text{nuc}}}) \end{aligned} \quad (2.15)$$

The solution of the TDSE will be presented in Sections 2.3 and 2.7.2.

## 2.2. Electronic Schrödinger Equation

In this section we will focus on the solution of the electronic Schrödinger equation (Eq. 2.9) which provides a potential energy for nuclear motion. First, we show how to write the wave function approximately as a single Slater determinant consisting of spin orbitals which are a product of spatial and spin functions. Then we express the spatial function as a linear combination of basis functions. The variational method, Hartree-Fock and post Hartree-Fock methods will be discussed. The solution of the electronic Schrödinger equation will provide the framework to solve the nuclear Schrödinger equation.

### 2.2.1. Variational Method and Hartree-Fock Theory

The variational principle described in the following equation is the basis of quantum chemical methods for solving the electronic TISE:

$$\frac{\langle \psi_{\text{el}} | H_{\text{el}} | \psi_{\text{el}} \rangle}{\langle \psi_{\text{el}} | \psi_{\text{el}} \rangle} = E \geq E_{\text{el}}. \quad (2.16)$$

For a pure one-body system, like the hydrogen atom, it is possible to solve the Schrödinger equation (Eq.2.9) analytically. For systems with few electrons, such as helium, the "many-electron" problem can be solved nevertheless exactly. However, many-electron systems cannot be treated with such precision in general case.

The Hartree-Fock method is widely used as an approximation for many-electron problems. Accordingly, every electron moves in the potential created by the nuclei plus the average potential of the other electrons. This leads to what is known as the independent particle model which essentially reduces the many-electron problem to the solving a set of coupled single electron equations.

In the Hartree-Fock frame the N-particle wavefunction consisting of N single orbital functions  $\chi_j(\vec{x}_i, \vec{s})$  gives a so-called Slater determinant (SD):

$$| \psi_{\text{el}} \rangle \approx (N!)^{-\frac{1}{2}} \begin{vmatrix} \chi_1(\vec{x}_1, \vec{s}) & \chi_2(\vec{x}_1, \vec{s}) & \dots & \chi_N(\vec{x}_1, \vec{s}) \\ \chi_1(\vec{x}_2, \vec{s}) & \chi_2(\vec{x}_2, \vec{s}) & \dots & \chi_N(\vec{x}_2, \vec{s}) \\ \vdots & \vdots & & \vdots \\ \chi_1(\vec{x}_N, \vec{s}) & \chi_2(\vec{x}_N, \vec{s}) & \dots & \chi_N(\vec{x}_N, \vec{s}) \end{vmatrix} \quad (2.17)$$

where  $(N!)^{-\frac{1}{2}}$  is a normalization factor and  $\chi_j(\vec{x}_i, \vec{s})$  is called a spin-orbital, defined as

a product of a spatial orbital  $\phi_j(\vec{s}_{ei}, \vec{s})$  which represent the spatial part of the molecular spin orbital and a spin orbital,  $\alpha(\omega_i)$  or  $\beta(\omega_i)$  indicate spin up and spin down functions which depends only on the spin coordinates  $\omega$ :

$$\chi_j(\vec{x}_i, \vec{s}) = \chi_j(\vec{s}_{ei}, \omega_i, \vec{s}) = \phi_j(\vec{s}_{ei}, \vec{s}) \cdot \begin{Bmatrix} \alpha(\omega_i) \\ \beta(\omega_i) \end{Bmatrix} \quad (2.18)$$

here, the  $\phi_j$  also depends on the nuclear coordinates  $\vec{s}$ . Below, we shall use a simplifying notation which needs the spatial coordinates  $\vec{s}_e$ , but deletes the spin functions and coordinates.

In HF, we assume that the trial wavefunction consists of a single Slater determinant. Choosing the single determinant as a trial function, the variational principle can be used to derive the HF equations, by minimizing the energy subject to the boundary condition, that the  $\chi_j$  are orthonormal. This gives the HF equations which by considering the closed-shell case and after eliminating the spin coordinates read

$$f(\vec{s}_{e1}, \vec{s})\phi_j(\vec{s}_{e1}, \vec{s}) = \epsilon_j\phi_j(\vec{s}_{e1}, \vec{s}) \quad (2.19)$$

where  $\epsilon_j$  are the orbital energies and  $f$ ,  $\phi_j$  and  $\epsilon_j$  depend parametrically on nuclear position  $\vec{s}$ , which will be dropped out in the next part for simplicity. The Fock operator  $f$  consists of the one electron operator  $h(\vec{s}_{ei})$  and the Hartree-Fock potential  $V^{HF}$ ,

$$f(\vec{s}_{e1}) = h(\vec{s}_{e1}) + V^{HF} = h(\vec{s}_{e1}) + \sum_{j=1}^{N/2} \left( 2J_j(\vec{s}_{e1}) - K_j(\vec{s}_{e1}) \right) \quad (2.20)$$

where the one-electron operator  $h(\vec{s}_{e1})$  is given by

$$h(\vec{s}_{e1}) = -\frac{\vec{P}_e^2}{2m_e} - \frac{1}{4\pi\epsilon_0} \sum_{n=1}^{N_{\text{nuc}}} \frac{Z_n e^2}{|\vec{s}_{e1} - \vec{s}_n|}. \quad (2.21)$$

The one electron operator  $h(\vec{s}_{e1})$  describes the motion of a single electron in the field of the nuclei, while the Hartree-Fock potential ( $V^{HF}$ ) describes the interaction of each electron with the average field of the other electrons. It consists of the Exchange operators ( $K_j$ ) and the Coulomb operators ( $J_j$ ), i.e.

$$J_j(\vec{s}_{e1})\phi_i(\vec{s}_{e1}) = \left[ \int d\vec{s}_{e2} \phi_j^*(\vec{s}_{e2}) \frac{1}{|\vec{s}_{e1} - \vec{s}_{e2}|} \phi_j(\vec{s}_{e2}) \right] \phi_i(\vec{s}_{e1}) \quad (2.22)$$

$$K_j(\vec{s}_{e1})\phi_i(\vec{s}_{e1}) = \left[ \int d\vec{s}_{e2} \phi_j^*(\vec{s}_{e2}) \frac{1}{|\vec{s}_{e1} - \vec{s}_{e2}|} \phi_i(\vec{s}_{e2}) \right] \phi_j(\vec{s}_{e1}) \quad (2.23)$$

The Hartree-Fock equation (Eq.2.19) is an integro-differential problem which has to be solved numerically. *Roothaan – Hall* proposed to expanded the HF orbitals into a set of atom centred orbitals [53]. This will transform the HF equation into a linear algebra type problem. Specifically, the spatial orbitals  $\phi_i$  are expanded into a linear combination of basis function  $\eta_j$ . These are also called atomic orbitals (AO) given by

$$\phi_i(\vec{s}_{e1}) = \sum_{\mu=1}^k c_{i\mu} \eta_{\mu}(\vec{s}_{e1}) \quad (2.24)$$

where  $\vec{s}_{e1}$  denote the coordinates of an arbitrary electron (e.g. the "first" one labelled "1") and  $\eta_{\mu}$  also depends parametrically on nuclear position  $\vec{s}$ . Eq.(2.24) is also referred to as the linear combination of atomic orbitals (LCAO) method used to calculate molecular orbitals. The coefficient  $c_{i\mu}$  need to be calculated. Using the variational method and vary the expectation value of the energy with respect to these coefficient, we get a matrix eigenvalue equation. In matrix notation it reads

$$\mathbf{FC} = \mathbf{SC}\epsilon \quad (2.25)$$

Here  $\epsilon$  is a diagonal matrix of the orbital energies,  $F$  is the Fock matrix and  $S$  is the overlap matrix given by

$$\mathbf{S}_{\mu\nu} = \int d\vec{s}_{e1} \eta_{\mu}^*(\vec{s}_{e1}) \eta_{\nu}(\vec{s}_{e1}) \quad (2.26)$$

and the Fock matrix

$$F_{\mu\nu} = \int d\vec{s}_{e1} \eta_{\mu}^*(\vec{s}_{e1}) f(\vec{s}_{e1}) \eta_{\nu}(\vec{s}_{e1}). \quad (2.27)$$

The matrix  $\mathbf{C}$  contains the coefficients  $c_{i\mu}$  of the basis function  $\eta_{\mu}(\vec{s}_{e1})$ . The HF method may then be understood: It simply involves optimizing the orbitals (or in other words the coefficient  $c_{i\mu}$  defining the MOs in terms of the AOs). Even if a large basis set is employed, the HF method yields only an approximation to the exact solution of the electronic Schrödinger equation [51, 53]. For highly accurate results, one has to go beyond HF.

### 2.2.2. Basis Sets

In modern computational chemistry, quantum chemical calculations are typically performed within a finite set of basis functions. The linear combination of atomic orbitals (LCAO) is a superposition of atomic orbitals and technique for calculating molecular orbitals.

There are two commonly used types of functions to built the atomic orbitals: Slater-type-orbitals (STO's) and Gaussian-type-orbitals (GTO's). The STO's were used as basis functions due to their similarity to atomic orbitals of the hydrogen atom. They are described by a function depending on spherical coordinates [51, 55, 56]:

$$\eta_{\zeta,n,l,m}^{STO}(s_e, \theta, \phi) = N s_e^{n-1} e^{-\zeta s_e} Y_{lm}(\theta, \phi) \quad (2.28)$$

where N is a normalization constant, and  $\zeta$  the "orbital exponent". The  $s_e$ ,  $\theta$ , and  $\phi$  are spherical coordinates, and  $Y_{lm}$  is the angular momentum part which describes the shape. The n, l and m are the principal, angular momentum and magnetic quantum numbers, respectively.

Unfortunately, the STO function is not easy to apply for fast calculations of two-electron integrals. So there is a need to introduce another orbital type, such as the cartesian Gaussian-type-orbitals, which is given by

$$\eta_{\zeta,l_x,l_y,l_z}^{GTO}(x, y, z) = N \cdot x^{l_x} \cdot y^{l_y} \cdot z^{l_z} \cdot e^{-\zeta s_e^2} \quad (2.29)$$

here N is the normalization constant and x, y, and z are cartesian coordinates and  $s_e^2 = x^2 + y^2 + z^2$ . The triple  $l_x$ ,  $l_y$  and  $l_z$  are integers; the sum  $l = l_x + l_y + l_z$  is used to classify the primitive Gaussian-functions as s-type ( $l=0$ ), p-type ( $l=1$ ), d-type orbitals ( $l=2$ ), etc. Due to the exponential dependences on  $s_e^2$ , a GTO has zero slop at the nucleus while STO has discontinuous derivatives. As a consequence, a GTO does not represent a proper behaviour of the wavefunctions near the nucleus as well as parts far away from it. GTOs are usually optimized for atoms, not being able to provide an adequate description of chemical bonds. In order to achieve a certin accuracy as with STOs more GTOs are needed. So, contracted Gaussian-type-orbitals (CGTOs) are used as linear combination of the primitive GTOs, these are given in the following form:

$$\eta_{\zeta,l_x,l_y,l_z}^{CGTO}(x, y, z) = \sum_p d_{p\mu} \eta_{\zeta_p,l_x,l_y,l_z}^{GTO}(x, y, z). \quad (2.30)$$

The coefficients  $d_{p\mu}$  are chosen such that contractions describe electronic orbitals in most realistic way.

If only the least number of contracted basis functions per atom is used required to describe the occupied atomic orbitals of the atom, then a so called *minimal basis* set is employed. If more than one contraction is used the basis set is called *double zeta*, *triple zeta*, etc. [55, 56, 57, 58].

### 2.2.3. Post Hartree-Fock Method

The Hartree-Fock picture lacks *electronic correlation* as a result of insufficient taking into account the mutual interaction between electrons. As a result, there is an energy difference between the HF method for a complete basis set and the exact non-relativistic energy  $E_{\text{el}}$ , which is called *correlation energy*,

$$E_{\text{corr}} = \epsilon_{\text{el}} - E_{\text{HF}}. \quad (2.31)$$

Two types of electron correlation can be distinguished, the dynamical correlation, describing the interaction between electrons in the same spatial orbital and static correlation, accounting for inter-orbital interaction for two spatially close orbitals. Many *ab initio* methods have been developed in order to add correlation to the HF-method, and they are denominated by post HF methods. Generally, they try to calculate the  $E_{\text{corr}}$  via perturbation theory or configuration interactions.

In the *configuration interaction* method, the way to introduce the correlation energy is to expand the exact electronic wavefunction in a linear combination of Slater determinants. A set of  $2K$  spin orbitals describing a single determinant ground state wavefunction for  $N$  electrons, is given in the following expression [59, 60]:

$$|\psi_{\text{el}}^0\rangle \approx |\chi_1\chi_2 \cdots \chi_a\chi_b \cdots \chi_N\rangle. \quad (2.32)$$

Eq.(2.32) is used to generate determinants according to the number of electrons excited to the virtual orbitals. The number of determinants depend on the number of electrons promoted to virtual orbitals. If one electron is excited from its occupied spin orbital ( $a$ ) to the virtual spin orbital ( $v$ ), then the wavefunction has the following form:

$$|\psi_{\text{el},a}^v\rangle \approx |\chi_1\chi_2 \cdots \chi_v\chi_b \cdots \chi_N\rangle. \quad (2.33)$$

So, one can have single excitation where one electron is promoted to a virtual orbital (Eq. (2.33)) or double excitation where two electrons are promoted,  $\cdots$  etc. , see ref. [51, 59, 60]. The full configuration interaction expansion for the ground state wavefunction

[59, 60] is given by

$$|\psi_{\text{el}}^0\rangle \approx c_0 |\psi_0\rangle + \sum_{av} c_a^v |\psi_a^v\rangle + \sum_{a>b,v>r} c_{a,b}^{v,r} |\psi_{a,b}^{v,r}\rangle + \dots \quad (2.34)$$

where the subscript (occupied orbitals) denotes the electron promoted to the virtual orbitals (superscript). This method cannot be applied for large molecules where a large number of electrons must be taken into account.

#### 2.2.4. Multi-Configuration Self Consistent Field (MCSCF)

*Multi-Configuration Self-Consistent field* method uses a linear combination of *configuration state* functions (CSFs) or configuration determinants to approximate the electronic wavefunction of an atom or molecule. MCSCF is the most frequently used method to study excited states. In MCSCF calculations, the set of the coefficients in front of determinants and the basis function of the molecular orbitals are optimized to obtain the total electronic wavefunction with lowest energy. This method is considered as a combination of *configuration interaction* (where the molecular orbitals are not varied but the expansion of wavefunction) and HF (where there is only one determinant but molecular orbitals are varied). The multi-configuration wavefunction is given by

$$|\psi_{\text{el}}\rangle \approx |\psi^{\text{MCSCF}}\rangle = \sum_k C_k^{\text{MCSCF}} |\psi_k\rangle. \quad (2.35)$$

Here, the  $C_k^{\text{MCSCF}}$  are the *configuration interaction* expansion coefficients. MCSCF wavefunctions are often used as a reference states for *multireference-configuration interaction* (MRCI) or *multi-reference perturbation* theories. These methods can deal with complex chemical situations and may be used to reliably calculate molecular ground and excited states.

#### 2.2.5. Complete Active Self Consistent Field (SCF)

In quantum chemistry, a *Complete Active Space Self-Consistent Field* is a type of *configuration interaction* with an defined sub-set of molecular orbitals [61]. In the CASSCF method, orbitals are classified into three classes: core orbitals, which always hold two electrons (occupied), active orbitals which are partially occupied and virtual orbitals which always are assumed to hold zero electrons. That classification allows to develop a set of Slater determinants for description of the wavefunction as a linear combination of determinants. One can also extend the active classification to all the molecular orbitals to obtain the full



*configuration interaction* treatment, but this is limited due to high computational cost. The choice of the active orbitals is very difficult and it depends in our knowledge about the system and what kind of chemical process one needs to study. The chosen orbitals can be distributed in all different ways to give total spin and space symmetry of the system. A CASSCF wavefunction maybe constructed for any type of electronic structure, such as open or closed shell, ground or excited states,...etc. The only limitation is the size of the chosen active space. A common notation is (n,m)-CASSCF, which indicates that n electrons are distributed in all possible ways in m orbitals.

In the quantum chemistry part of this study, the state average CASSCF (SA-CASSCF) method is applied. Using that method orbitals are optimized for a suitable average of the desired states for a given symmetry and spin. In SA-CASSCF method all states are expressed using the same MO's, thereby ensuring the orthogonality.

## 2.3. Conical Intersections (CIs) and Non-Adiabatic Coupling Terms (NACTs)

The Born-Oppenheimer approximation is the keystone to the visualization of chemical processes by enabling to picture molecules as a set of nuclei moving along a PES provided by the electrons. However, whereas the validity of Born-Oppenheimer approximation for the many of chemical systems is not in doubt, it is now clear that in many important cases the approximation breaks down [2, 3]. That is to say, the nuclear and electronic motions are coupled. This is mostly common in photochemistry of polyatomic molecules where there are a large number of energetically close-lying electronic states and many nuclear degrees of freedom.

An important example of the result of coupling between the nuclei and electrons, named vibronic coupling, is a conical intersection (CI) between electronic states. CIs offer pathways for ultra-fast interstate crossing on the femtosecond time scale. Conical intersections have important consequences for the nuclear dynamics. A CI permits efficient non-adiabatic transitions between PESs. A derivative coupling that couples the different electronic states is inversely proportional to the energy difference of the two electronic states. Therefore, the smaller the difference, the larger the coupling. This phenomena is a result of the break down of the Born-Oppenheimer approximation, where it is assumed that the non-adiabatic coupling terms are zero. So it is necessary to calculate these coupling terms for non Born-Oppenheimer processes. In order to solve the Schrödinger equation for the total Hamiltonian  $H_{tot}$  describing both nuclear and electronic motion, the total wavefunction

is expanded into the  $i$  electronic states,

$$| \psi_{\text{tot}} \rangle = \sum \psi_{\text{nuc}}^i(\vec{s}, t) | \psi_{\text{el}}^i(\vec{s}_e, \vec{s}) \rangle \quad (2.36)$$

here  $\vec{s} = (\vec{s}_1, \vec{s}_2, \dots, \vec{s}_{N_{\text{nuc}}})$  denotes all nuclear coordinates, and  $\vec{s}_e = (\vec{s}_{e1}, \vec{s}_{e2}, \dots, \vec{s}_{en})$  denotes all electronic coordinates.

The total Hamiltonian Eq. (2.2) can be written as

$$H_{\text{tot}} = \sum_{n=1}^{N_{\text{nuc}}} -\frac{\hbar^2}{2M_n} \nabla_n^2 + H_{\text{el}} + V_{\text{nuc,nuc}} \quad (2.37)$$

The  $\nabla_n$  is a three dimensional gradient with respect to the nuclear coordinates. To solve the Schrödinger equation Eq.(2.1), the total Hamiltonian has to be applied to the wavefunction Eq.(2.36). Applying the  $\nabla_n$  operator to the wavefunction on the right hand side of Eq.(2.36) gives

$$\begin{aligned} \nabla_n^2 [\psi_{\text{el}}^i(\vec{s}_e, \vec{s}) \psi_{\text{nuc}}^i(\vec{s}, t)] &= \nabla_n [\nabla_n \psi_{\text{el}}^i(\vec{s}_e, \vec{s}) \psi_{\text{nuc}}^i(\vec{s}, t)] \\ &= \psi_{\text{el}}^i(\vec{s}_e, \vec{s}) \nabla_n^2 \psi_{\text{nuc}}^i(\vec{s}, t) + \psi_{\text{nuc}}^i(\vec{s}, t) \nabla_n^2 \psi_{\text{el}}^i(\vec{s}_e, \vec{s}) \\ &\quad + 2 \nabla_n \psi_{\text{nuc}}^i(\vec{s}, t) \nabla_n \psi_{\text{el}}^i(\vec{s}_e, \vec{s}), \end{aligned} \quad (2.38)$$

where  $\vec{s}_e$  denotes all electronic coordinates for simplicity.

Using expression (2.38), Eq.(2.8) and Eq.(2.9), the Schrödinger equation Eq.(2.1) can be multiplied from the left with the electronic state  $\psi_{\text{el}}^j$ , followed by integration over electronic coordinates. This leads to the following coupled equations:

$$\begin{aligned} i\hbar \frac{\partial}{\partial t} \psi_{\text{nuc}}^j(\vec{s}, t) &= \left[ T_{\text{nuc}} + V_j(\vec{s}) \right] \psi_{\text{nuc}}^j(\vec{s}, t) \\ &+ \left[ \sum_i \sum_{n=1}^{N_{\text{nuc}}} -\frac{\hbar^2}{2M_n} (2\tau_{ji,n}^{(1)} \nabla_n + \tau_{ji,n}^{(2)}) \right] \psi_{\text{nuc}}^i(\vec{s}, t) \end{aligned} \quad (2.39)$$

with

$$T_{\text{nuc}} = \sum_{n=1}^{N_{\text{nuc}}} -\frac{\hbar^2}{2M_n} \nabla_n^2, \quad (2.40)$$

$\tau_{ji}^{(1)}$  is the (first-order) non-adiabatic coupling (vector) matrix with the elements

$$\tau_{ji,n}^{(1)} = \langle \psi_{\text{el}}^j(\vec{s}) | \nabla_n \psi_{\text{el}}^i(\vec{s}) \rangle \quad (2.41)$$

and  $\tau_{ji}^{(2)}$  is the non-adiabatic (scaler) matrix of the second-order with the elements

$$\tau_{ji,n}^{(2)} = \langle \psi_{\text{el}}^j(\vec{s}) | \nabla_n^2 \psi_{\text{el}}^i(\vec{s}) \rangle \quad (2.42)$$

If a group of states forms a Hilbert space, so that the  $\tau$  matrix fulfil the divergence condition [3], then  $\tau_{ji,n}^{(2)}$  can be presented in terms of  $\tau_{ji,n}^{(1)}$  as follows:

$$\tau_{ji,n}^{(2)} = \tau_{ji,n}^{(1)2} + \nabla_n \tau_{ji,n}^{(1)} \quad (2.43)$$

In this thesis, we investigate the motion of a single atom in a molecule. Therefore, we consider only the nuclear coordinates of this atom ( $n=1$ ) in the nuclear Schrödinger Eq.(2.39). Writing  $M_1 = M$ ,  $\tau_{ji,1}^{(1)} = \tau_{ji}^{(1)}$ ,  $\tau_{ji,1}^{(2)} = \tau_{ji}^{(2)}$  and  $\nabla_1 = \nabla$ , Eq. (2.39) can be written as

$$\begin{aligned} i\hbar \frac{\partial}{\partial t} \psi_{\text{nuc}}^j(\vec{s}, t) &= \left[ T_{\text{nuc}} + V_j(\vec{s}) \right] \psi_{\text{nuc}}^j(\vec{s}, t) \\ &\quad - \frac{\hbar^2}{2M} \sum_i \left( 2\tau_{ji}^{(1)} \nabla + \tau_{ji}^{(2)} \right) \psi_{\text{nuc}}^i(\vec{s}, t) \end{aligned} \quad (2.44)$$

Substituting Eq.(2.43) in Eq.(2.44) yield

$$\begin{aligned} i\hbar \frac{\partial}{\partial t} \psi_{\text{nuc}}^j(\vec{s}, t) &= \left[ T_{\text{nuc}} + V_j(\vec{s}) \right] \psi_{\text{nuc}}^j(\vec{s}, t) \\ &\quad - \frac{\hbar^2}{2M} \sum_i \left( 2\tau_{ji}^{(1)} \nabla + \tau_{ji}^{(1)2} + \nabla \tau_{ji}^{(1)} \right) \psi_{\text{nuc}}^i(\vec{s}, t) \end{aligned} \quad (2.45)$$

If two state become close to each other, or degenerate, the mixing between them, i.e. the coupling terms Eq.(2.41) and (2.42) become larger. So one must consider the non-adiabatic coupling terms and the motion on several PES [3]. This is not easy task since the kinetic energy operator is not diagonal. For this reason the wavefunctions are transformed into the diabatic basis where the kinetic energy is diagonal, i.e. the non adiabatic coupling term vanish. The adiabatic-to-diabatic transformation will be described in Section 2.5. The way to calculate the non-adiabatic coupling terms quantum chemically will be explained in the next section.

## 2.4. Quantum Chemical Calculation of the NACTs

In order to calculate the non-adiabatic coupling terms we used the MOLPRO program package [32]. The method implemented in the program is based on the analysis of the

configuration interaction vectors. The basic assumption in this method is neglecting any change of the CASSCF orbitals as a function of geometry, since the configuration interaction vectors of diabtic states are approximately geometry independent. Using this assumption, the NACTs can be computed for state-average CASSCF (SA-CASSCF) wavefunction. The configuration interaction wavefunction of electronic states  $i$  is given by

$$|\psi_{\text{el}}^{i,MCSCF}\rangle = \sum_k C_{ik} |\psi_{\text{el}}^k\rangle \quad (2.46)$$

The pervious equation can be rewritten for two different electronic states  $i$  and  $j$  in the following form:

$$\langle\psi_{\text{el}}^i | \nabla\psi_{\text{el}}^j\rangle = \langle\sum_l C_{il}\psi_{\text{el}}^l | \nabla\sum_k C_{jk}\psi_{\text{el}}^k\rangle \quad (2.47)$$

simplifying Eq.(2.47) leads to

$$\begin{aligned} & \sum_l \sum_k C_{jl}(\nabla C_{ik})\langle\psi_{\text{el}}^l | \psi_{\text{el}}^k\rangle + \sum_l \sum_k C_{jl}C_{ik}\langle\psi_{\text{el}}^l | \nabla\psi_{\text{el}}^k\rangle \\ & = \sum_l C_{jl}(\nabla C_{il}) + \sum_l \sum_k C_{jl}C_{ik}\langle\psi_{\text{el}}^l | \nabla\psi_{\text{el}}^k\rangle \end{aligned} \quad (2.48)$$

The first term in Eq.(2.48) refer to the  $C_{ij}$ -term which involves differentiation of the configuration interaction coefficients. The second term contains derivatives of configuration or determinants.

The diabatic MCSCF orbitals can be generated by maximizing the overlap of CASSCF orbitals at displaced geometry with respect to the reference geometry (This can be done by using the invariance of the CASSCF and multi reference configuration interaction energies with respect to unitary transformations). As a result, the relative contribution of the orbitals and configuration interaction to the matrix elements of non-adiabatic coupling elements ( $\tau_{ij}^{(1)}$ ) are modified. This can be achieved by maximizing the overlap of the active CASSCF orbitals with those of reference geometry at which the wavefunction are assumed to be diabatic. As a result, the second term in Eq.(2.48) is minimized and to very good approximation the matrix elements of  $\tau_{ji}^{(1)}$  could be obtained from the configuration interaction vector ( $C_{ij}$ -term) alone.

MOLPRO has two procedures to calculate NACTs for the CASSCF: first-order and second-order algorithms. In both cases the displaced geometries must be calculated and stored in one of these order. In first-order algorithm the wavefunction of the reference geometry ( $\vec{s}$ ) and positively displaced geometry ( $\vec{s} + \Delta\vec{s}$ ) are calculated, while in the second order, the negatively displaced geometry must be calculated ( $\vec{s} - \Delta\vec{s}$ ). Then, the

transition densities matrix is computed from the configuration interaction vectors and these displacement geometries by the following formula

$$\langle \psi_{\text{el}}^i | \nabla \psi_{\text{el}}^j \rangle \approx \frac{1}{2\Delta\vec{s}} \langle \psi_{\text{el}}^i(\vec{s} + \Delta\vec{s}) | \psi_{\text{el}}^j(\vec{s} - \Delta\vec{s}) \rangle \quad (2.49)$$

where the left subscripts  $i, j$  refer to the two different states, and  $\Delta s$  refers to the small increment. The transformation matrix of the configuration interaction vectors between the  $s$  and  $s + \Delta s$ , is chosen such that non-adiabatic coupling matrix  $\langle \psi_{\text{el}}^i | \nabla \psi_{\text{el}}^j \rangle$  elements are minimized for all the internal coordinates.

## 2.5. Adiabatic-to-Diabatic Transformation (ADT)

In the following part we will introduce what is known as adiabatic-to-diabatic transformation (ADT). Through the ADT the diabatic nuclear wavefunctions  $\psi_{\text{nuc}}^{i,d}$  will be determined from the adiabatic ones  $\psi_{\text{nuc}}^i$  using a unitary transformation [3, 63, 67, 69].

The starting point of the adiabatic-to-diabatic picture is the nuclear Schrödinger equation Eq.(2.45) [3], which can be written in matrix form as

$$i\hbar \frac{\partial}{\partial t} \vec{\psi}_{\text{nuc}} = -\frac{\hbar^2}{2M} (\nabla + \tau^{(1)})^2 \vec{\psi}_{\text{nuc}} + \mathbf{V} \vec{\psi}_{\text{nuc}} \quad (2.50)$$

where

$$\vec{\psi}_{\text{nuc}} = \begin{pmatrix} \psi_{\text{nuc}}^N \\ \vdots \\ \psi_{\text{nuc}}^0 \end{pmatrix}, \quad (2.51)$$

the matrix

$$\tau^{(1)} = \begin{pmatrix} \tau_{ij}^{(1)} \end{pmatrix} \quad (2.52)$$

includes the NACTs, see Eq.(2.41), and

$$V = \begin{pmatrix} V_N & & 0 \\ & \ddots & \\ 0 & & V_0 \end{pmatrix} \quad (2.53)$$

is a diagonal matrix containing the PES of each electronic states.

In Eq.(2.50) the NAC terms  $\tau^{(1)}$  can be eliminated by performing adiabatic-to-diabatic transformations. This can be done by replacing the adiabatic wavefunction  $\vec{\psi}_{\text{nuc}}$  by the

diabatic basis function  $\vec{\psi}_{\text{nuc}}^d$ , where the two functions are related as follows

$$\vec{\psi}_{\text{nuc}} = \mathbf{A}\vec{\psi}_{\text{nuc}}^d \quad (2.54)$$

Here  $\mathbf{A}$  is a matrix to be determined by the requirement that the matrix  $(\tau^{(1)})$  will vanish in the Schrödinger equation for  $\vec{\psi}^d$ . In order to fulfil this condition [3], we evaluate the following expression

$$\begin{aligned} (\nabla + \tau^{(1)})^2 \mathbf{A}\vec{\psi}_{\text{nuc}}^d &= (\nabla + \tau^{(1)})(\nabla + \tau^{(1)})\mathbf{A}\vec{\psi}_{\text{nuc}}^d \\ &= (\nabla + \tau^{(1)})(\mathbf{A}\nabla\vec{\psi}_{\text{nuc}}^d + (\nabla\mathbf{A})\vec{\psi}_{\text{nuc}}^d + \tau^{(1)}\mathbf{A}\vec{\psi}_{\text{nuc}}^d) \\ &= 2(\nabla\mathbf{A}) \cdot \nabla\vec{\psi}_{\text{nuc}}^d + \mathbf{A}\nabla^2\vec{\psi}_{\text{nuc}}^d + (\nabla^2\mathbf{A})\vec{\psi}_{\text{nuc}}^d + (\nabla\tau^{(1)})\mathbf{A}\vec{\psi}_{\text{nuc}}^d \\ &+ 2\tau^{(1)}(\nabla\mathbf{A})\vec{\psi}_{\text{nuc}}^d + 2\tau^{(1)}\mathbf{A}(\nabla\vec{\psi}_{\text{nuc}}^d) + \tau^{(1)2}\mathbf{A}\vec{\psi}_{\text{nuc}}^d \end{aligned} \quad (2.55)$$

which can be rearranged to become

$$\begin{aligned} (\nabla + \tau^{(1)})^2 \mathbf{A}\vec{\psi}_{\text{nuc}}^d &= \mathbf{A}\nabla^2\vec{\psi}_{\text{nuc}}^d + 2(\nabla\mathbf{A} + \tau^{(1)}\mathbf{A}) \cdot \nabla\vec{\psi}_{\text{nuc}}^d \\ &+ \{(\tau^{(1)} + \nabla) \cdot (\nabla\mathbf{A} + \tau^{(1)}\mathbf{A})\}\vec{\psi}_{\text{nuc}}^d \end{aligned} \quad (2.56)$$

The grad operator, in the third term, does not act beyond the curled parentheses { }. Next, by choosing  $\mathbf{A}$  to be the solution of the following equation

$$\nabla\mathbf{A} + \tau^{(1)}\mathbf{A} = 0 \quad (2.57)$$

Eq.(2.56) becomes

$$(\nabla + \tau^{(1)})^2 \mathbf{A}\vec{\psi}_{\text{nuc}}^d = \mathbf{A}\nabla^2\vec{\psi}_{\text{nuc}}^d \quad (2.58)$$

Substituting Eq.(2.54) and Eq.(2.58) in Eq.(2.50) yield

$$\begin{aligned} i\hbar\frac{\partial}{\partial t}\mathbf{A}\vec{\psi}_{\text{nuc}}^d &= -\frac{\hbar^2}{2M}(\nabla + \tau^{(1)})^2\mathbf{A}\vec{\psi}_{\text{nuc}}^d + \mathbf{V}\mathbf{A}\vec{\psi}_{\text{nuc}}^d \\ i\hbar\frac{\partial}{\partial t}\mathbf{A}\vec{\psi}_{\text{nuc}}^d &= -\frac{\hbar^2}{2M}\mathbf{A}\nabla^2\vec{\psi}_{\text{nuc}}^d + \mathbf{V}\mathbf{A}\vec{\psi}_{\text{nuc}}^d \end{aligned} \quad (2.59)$$

Multiplying Eq.(2.59) by  $\mathbf{A}^\dagger$  (the conjugate matrix of  $\mathbf{A}$ ), we get the nuclear Schrödinger equation,

$$\begin{aligned} i\hbar\frac{\partial}{\partial t}\mathbf{A}^\dagger\mathbf{A}\vec{\psi}_{\text{nuc}}^d &= -\frac{\hbar^2}{2M}\mathbf{A}^\dagger\mathbf{A}\nabla^2\vec{\psi}_{\text{nuc}}^d + \mathbf{A}^\dagger\mathbf{V}\mathbf{A}\vec{\psi}_{\text{nuc}}^d \\ i\hbar\frac{\partial}{\partial t}\vec{\psi}_{\text{nuc}}^d &= -\frac{\hbar^2}{2M}\nabla^2\vec{\psi}_{\text{nuc}}^d + \mathbf{W}\vec{\psi}_{\text{nuc}}^d \end{aligned} \quad (2.60)$$

where  $\mathbf{W}$  is the diabatic potential given by

$$\mathbf{W} = \mathbf{A}^\dagger \mathbf{V} \mathbf{A}. \quad (2.61)$$

Eq.(2.60) represents the time-dependent Schrödinger equation in the diabatic representation. Here, the kinetic energy is diagonal, and the coupling has been transferred to the diabatic potential matrix which has off-diagonal elements. This equation will be used to simulate the nuclear dynamics. The value of  $\mathbf{A}$  depends on the contour  $L$  along which it is calculated. In general, the solution of  $\mathbf{A}$  in Eq.(2.57) for N-state model is given by

$$\mathbf{A}(\vec{s} | L) = \wp \exp \left[ - \int_{\vec{s}_0}^{\vec{s}} d\vec{s}' \cdot \tau^{(1)}(\vec{s}') \right] \mathbf{A}(\vec{s}_0) \quad (2.62)$$

where  $\wp$  is the ordering operator.  $\vec{s}_0$  and  $\vec{s}$  are the initial and final points of the contour  $L$ , respectively. Since in this study, we calculate the  $\mathbf{A}$ -matrix along a circle described by the angle  $\phi$  and the radius  $r$ , Eq.(2.62) can be simplified for constant  $r$

$$A(r, \phi) = \wp \exp \left[ - \int_{\phi_0}^{\phi} d\phi' \cdot \tau_{\phi'}(\phi') \right] A(r, \phi_0) \quad (2.63)$$

where

$$\tau_{\phi} = (\tau_{\phi}^{i,j}) \quad (2.64)$$

with

$$\tau_{\phi}^{i,j} = \langle \psi_{\text{el}}^j | \frac{\partial}{\partial \phi} \psi_{\text{el}}^i \rangle. \quad (2.65)$$

Numerically one can evaluate Eq.(2.63) by successively calculating the values of  $\mathbf{A}$  at point  $\phi_j$  from  $\phi_{j-1}$ :

$$A(r, \phi_j) = \exp \left[ - \int_{\phi_{j-1}}^{\phi_j} \tau_{\phi}(r, \phi') d\phi' \right] A(r, \phi_{j-1}) \quad (2.66)$$

where the grid point are chosen such that during the interval  $\Delta\phi = \phi_j - \phi_{j-1}$  the NACT-matrix  $\tau_{\phi}(r, \phi)$  is constant. Thus, Eq.(2.63) can be approximated by

$$A(r, \phi_j) = \exp \left[ - \tau_{\phi}(\tilde{\phi}_j) \Delta\phi \right] A(r, \phi_{j-1}) \quad (2.67)$$

where  $\tilde{\phi}_j = \frac{\phi_j - \phi_{j-1}}{2}$ .

The next step is to derive the value of the exponential matrix  $F = \exp[-\tau_{\phi}(\tilde{\phi}_j) \Delta\phi]$ . The

matrix  $\mathbf{F}$  can be written as

$$F = G^\dagger D G \quad (2.68)$$

where  $D = \exp(\lambda)$  and  $\lambda$  is diagonal matrix that contains the eigenvalues of  $[\tau_\phi(\tilde{\phi}) \Delta \phi]$ . Equation (2.66) can then be rewritten in the following form

$$A(\phi_j) = G^\dagger(\tilde{\phi}_j) D(\tilde{\phi}_j) G(\tilde{\phi}_j) A(\phi_{j-1}) \quad (2.69)$$

where

$$D(\tilde{\phi}_j) = \exp(\tilde{\lambda}(\tilde{\phi}_j) \Delta \phi) \quad (2.70)$$

and  $\tilde{\lambda}(\tilde{\phi}_j)$  is the matrix that contains the eigenvalue of  $\tau_\phi(\tilde{\phi}_j)$ .

If the  $\mathbf{A}$ -matrix is calculated along a closed circle, here from  $\phi_0$  to  $\phi_0 + 2\pi$ , the conditions

$$A_{ii}(\phi_0 + 2\pi) = \pm 1 \quad (2.71)$$

and

$$A_{ij}(\phi_0 + 2\pi) = 0 \quad (2.72)$$

for  $i \neq j$  must be fulfilled if the initial matrix  $\mathbf{A}(\phi_0) = 1$ . Otherwise the elements of the diabatic potential matrix  $\mathbf{W}$ , see Eq.(2.61), are not single-valued. The number of plus (+) and minus (-) in Eq.(2.71) is determined by the number of conical intersection CIs located inside closed loop [3]. In particular, the plus sign indicate that an even number of conical intersection are enclosed by closed loop  $L$  from  $\phi = 0$  to  $\phi = 2\pi$  [3, 71].

## 2.6. Interaction of Molecules with a Laser Field

In this thesis, the nuclear dynamics of photo-excited molecule is investigated. Therefore, we have to consider the interaction between a molecule and a laser field. The TDSE is therefore modified to

$$i\hbar \frac{\partial}{\partial t} | \Psi(t) \rangle = H(t) | \Psi(t) \rangle \quad (2.73)$$

The  $\Psi(t)$  represent the total wavefunction which consists of the sum over all orthonormal electronic and nuclear wavefunctions. The time-dependent Hamiltonian operator is given by [51]

$$H(t) = H_{tot} - \underbrace{\vec{\mu} \cdot \vec{E}(t)}_{E_{int}} \quad (2.74)$$



The above total Hamiltonian consists of two parts, total molecular Hamiltonian and the time-dependent potential energy as a result of interaction between the molecular dipole moment  $\vec{\mu}$  and the external electromagnetic field  $\vec{E}(t)$ . The interaction of the dipole moment with the external field gives a time-dependent potential energy term  $E_{int}$ .

The total dipole moment includes both the nuclear and electronic dipole moment and has the following form:

$$\vec{\mu} = \sum_{i=1}^{N_{el}} (-e) \vec{s}_{ei} \sum_{j=1}^{N_{nuc}} (Z_j e) \vec{s}_j \quad (2.75)$$

Since we treat more than one electronic state, the Hamiltonian operator should be written in the matrix form

$$i\hbar \frac{\partial}{\partial t} \begin{pmatrix} |\Psi_N(t)\rangle \\ \vdots \\ |\Psi_0(t)\rangle \end{pmatrix} = \begin{pmatrix} H_{NN}(t) & \cdots & H_{N0}(t) \\ \vdots & \ddots & \vdots \\ H_{0N}(t) & \cdots & H_{00}(t) \end{pmatrix} \begin{pmatrix} |\Psi_N(t)\rangle \\ \vdots \\ |\Psi_0(t)\rangle \end{pmatrix} \quad (2.76)$$

where the indexes  $0, 1, 2, \dots, N$  denote the electronic states. The time dependent Hamiltonian operator (assuming three electronic states  $0, 1, 2$ ) is given by the following equation:

$$H(t) = \begin{pmatrix} T_{nuc} + V_2 & 0 & 0 \\ 0 & T_{nuc} + V_1 & 0 \\ 0 & 0 & T_{nuc} + V_0 \end{pmatrix} + \begin{pmatrix} \Lambda_{22} & \Lambda_{21} & \Lambda_{20} \\ \Lambda_{12} & \Lambda_{11} & \Lambda_{10} \\ \Lambda_{02} & \Lambda_{01} & \Lambda_{00} \end{pmatrix} - \vec{E}(t) \begin{pmatrix} \vec{\mu}_{22} & \vec{\mu}_{21} & \vec{\mu}_{20} \\ \vec{\mu}_{12} & \vec{\mu}_{11} & \vec{\mu}_{10} \\ \vec{\mu}_{02} & \vec{\mu}_{01} & \vec{\mu}_{00} \end{pmatrix} \quad (2.77)$$

with

$$\Lambda_{ji} = -\frac{\hbar^2}{2M} \left( 2\tau_{ji}^{(1)} \nabla + \tau_{ji}^{(2)} \right)$$

and  $\tau_{ji}^{(1)}$  and  $\tau_{ji}^{(2)}$  defined in Eq.(2.41) and (2.42),  $T_{nuc}$  is the kinetic energy of the nuclei,  $V_0$ ,  $V_1$  and  $V_2$  are the ground and excited state PESs. The coupling with a laser field is treated using the dipole moments  $\vec{\mu}^{ii}$  of the electronic state  $S_0$ ,  $S_1$  and  $S_2$  and the transition dipole moments  $\mu^{ij}$ ,  $j \neq i$ .

As described in Section 2.5, it is easier to solve the TDSE in the diabatic basis. Thus one can write the matrix elements of the diabatic Hamiltonian, which is given in the following formula:

$$H^d(t) = \mathbf{A}^\dagger H(t) \mathbf{A} = \begin{pmatrix} T_{\text{nuc}} + W_{22} & W_{21} & W_{20} \\ W_{12} & T_{\text{nuc}} + W_{11} & W_{10} \\ W_{02} & W_{01} & T_{\text{nuc}} + W_{00} \end{pmatrix} - \vec{E}(t) \begin{pmatrix} \vec{\mu}_{22}^d & \vec{\mu}_{21}^d & \vec{\mu}_{20}^d \\ \vec{\mu}_{12}^d & \vec{\mu}_{11}^d & \vec{\mu}_{10}^d \\ \vec{\mu}_{02}^d & \vec{\mu}_{01}^d & \vec{\mu}_{00}^d \end{pmatrix} \quad (2.78)$$

The diabaticization scheme leads to the diabatic potentials with  $\mathbf{W} = \mathbf{A}^\dagger \mathbf{V} \mathbf{A}$  and also the diabatic dipole and transition dipole moments with  $\vec{\mu}^d = \mathbf{A}^\dagger \vec{\mu} \mathbf{A}$ . The diabatic terms arise as a result of using adiabatic-to-diabatic transformation where the unitary transformation matrix  $\mathbf{A}$  is used, which has been introduced in Section 2.5.

Equation (2.74) is a semi-classical dipole approximation which represent the operator for the interaction between molecule and laser field [72]. The electromagnetic field used to control intra-molecular motion is given by:

$$\vec{E}(\vec{r}, t) = \vec{\epsilon} \cdot E^0 \cdot f(t) \cdot \frac{e^{i(\vec{k}\vec{r}-\omega t)} + e^{-i(\vec{k}\vec{r}-\omega t)}}{2} \quad (2.79)$$

where  $E^0$  is the amplitude of the field with the carrier frequency  $\omega$ ,  $\vec{\epsilon}$  is the polarization vector,  $\vec{k}$  the wave vector and  $f(t)$  the shape function which describes the envelope of the laser pulse. The following expression can be expanded using Taylor series:

$$e^{i\vec{k}\vec{r}} \approx 1 + i\vec{k}\vec{r} + \dots \quad (2.80)$$

Since the laser pulse are considered which cover a range of wavelengths in the visible or UV range,  $\lambda \approx 400 \text{ nm}$  or  $400 \cdot 10^{-9} \text{ m}$ . If a molecule with dimension several  $\text{\AA}$  ( $10^{-10} \text{ m}$ ) are investigate  $\vec{k}\vec{r} \ll 1$ , so after first term the Taylor series can be truncated. As a result the expression for the position-independent field is given by:

$$\vec{E}(t) = \vec{\epsilon} \cdot E^0 \cdot f(t) \frac{e^{i\omega t} + e^{-i\omega t}}{2} = \vec{E}^0 \cdot f(t) \cos(\omega t) \quad (2.81)$$

where the shape function  $f(t)$  is given by:

$$f(t) = \sin^2 \left[ \frac{\pi(t - t_d)}{t_p} \right] \quad (2.82)$$

for  $t_d \leq t \leq t_d + t_p$  and  $s(t) = 0$  elsewhere. Here  $t_p$  is the pulse duration and  $t_d$  is the delay time.

## 2.7. Numerical Methods for the Solution of the Nuclear Schrödinger Equation

### 2.7.1. Solution of the Nuclear TISE: Fourier-Grid-Hamiltonian Method

The time independent nuclear Schrödinger equation for a single electronic state reads

$$H_{\text{nuc}} |\Phi_{\text{nuc}}^j\rangle = E_{\text{nuc}}^j |\Phi_{\text{nuc}}^j\rangle \quad (2.83)$$

where the nuclear Hamiltonian is given in Eq.(2.13), see Section 2.1.

The resulting eigen functions  $|\Phi_{\text{nuc}}^j\rangle$  describes the rotation, vibration and translation of the  $N_{\text{nuc}}$  nuclei. These eigenfunctions are used as an initial state for quantum dynamical calculation. In order to solve Eq.(2.83) or in general a time independent Schrödinger equation

$$H |\Phi^j\rangle = E^j |\Phi^j\rangle \quad (2.84)$$

a Fourier Grid Hamiltonian (FGH) is used [73, 74]. FGH uses the forward and backward Fourier Transform (FT) between momentum and position space for evaluating the position and momentum operator, with discretization of position and momentum space on series of equidistant  $N$  grid points. This method exploits the fact that the kinetic energy of the FGH is diagonal in momentum space while the potential energy is diagonal in position space [73, 74]. Assuming for simplicity the one dimensional case where a particle of mass  $m$  is moving in  $x$  direction with momentum  $p$  within a potential  $V(x)$ , the Hamilton operator  $H$  is written as the sum of kinetic and potentials energy:

$$H = T + V(\hat{x}) = \frac{\hat{p}^2}{2m} + V(\hat{x}) \quad (2.85)$$

The basis sets are chosen such that the Hamilton operator spans a subspace of the Hilbert

space. The basis for the position space is given by

$$\hat{x} | x \rangle = x | x \rangle \quad (2.86)$$

where the basis vectors form an orthonormal basis and fulfil the completeness relationship

$$\langle x | x' \rangle = \delta(x - x') \quad (2.87)$$

and

$$\hat{I}_x = \int_{-\infty}^{\infty} dx | x \rangle \langle x | \quad (2.88)$$

while the potential is diagonal in position space, and given in the following form:

$$\langle x' | V(\hat{x}) | x \rangle = V(x)\delta(x - x') \quad (2.89)$$

Equivalent expressions hold for the momentum space with the momentum operator,

$$\hat{p} | k \rangle = \hbar k | k \rangle \quad (2.90)$$

and analogous completeness and closure relations:

$$\langle k | k' \rangle = \delta(k - k') \quad (2.91)$$

$$\hat{I}_k = \int_{-\infty}^{\infty} dk | k \rangle \langle k' | \quad (2.92)$$

So, the kinetic energy operator is diagonal in momentum space, i.e.

$$\langle k' | T | k \rangle = T_k \delta(k - k') = \frac{\hbar^2 k^2}{2m} \delta(k - k') \quad (2.93)$$

with the eigenvalue  $\frac{\hbar^2 k^2}{2m}$ . The coordinate space can be transformed to the momentum space and vice versa by

$$\langle k | x \rangle = \frac{1}{\sqrt{2\pi}} \exp(-ikx) \quad (2.94)$$

From the above definition, the matrix elements of the total Hamilton operator in position space can be written in the following equation:

$$\begin{aligned}
 \langle x | H | x' \rangle &= \langle x | T | x' \rangle + V(x)\delta(x - x') \\
 &= \langle x | \left\{ \int_{-\infty}^{\infty} | k' \rangle \langle k' | dk' \right\} T \left\{ \int_{-\infty}^{\infty} | k \rangle \langle k | \right\} | x' \rangle dk + V(x)\delta(x - x') \\
 &= \int_{-\infty}^{\infty} \langle x | k \rangle T_k \langle k | x' \rangle dk + V(x)\delta(x - x') \\
 &= \frac{1}{2\pi} \int_{-\infty}^{\infty} e^{ik(x-x')} T_k dk + V(x)\delta(x - x') \tag{2.95}
 \end{aligned}$$

In this equation, the identity operator presented in Eq.(2.92) is inserted on the left and right sides of  $T$  in Eq.(2.93). The continuous variable  $x$  is now discretized into a series of  $N$  grid points with equal intervals

$$x_i = i\Delta x, \quad i = 1, 2, \dots, N \tag{2.96}$$

For even  $N$ , the eigenvectors of the discrete basis satisfy

$$\Delta x \langle x_i | x_j \rangle = \delta_{ij} \tag{2.97}$$

and

$$\hat{I}_x = \sum_{i=1}^N | x_i \rangle \Delta x \langle x_i | \tag{2.98}$$

The Hamiltonian matrix elements in the discrete basis are given by using the discrete basis in position space. The matrix elements are given by

$$H_{ij} = \langle x_i | H | x_j \rangle = \frac{1}{\Delta x} \left( \sum_{l=-(\frac{N}{2}-1)}^{\frac{N}{2}} \frac{e^{i2\pi(i-j)l/N}}{N} T_l + V(x_i)\delta_{ij} \right) \tag{2.99}$$

where

$$T_l = \frac{\hbar^2}{2m} \cdot (l\Delta k)^2 \quad (2.100)$$

and

$$\Delta k = \frac{2\pi}{N\Delta x} \quad (2.101)$$

The expectation value of the energy  $E^j$  is :

$$E^j = \frac{\langle \Phi^j | H | \Phi^j \rangle}{\langle \Phi^j | \Phi^j \rangle} \quad (2.102)$$

Minimizing this energy with respect to variation of the coefficients  $\Phi_i^j$  yields the standard set of secular equations, and its root corresponds to the bound state energies of the systems. Each root has an associated set of the coefficients  $\Phi_i^j$  that give the amplitude of the wavefunction  $|\Phi_i^j\rangle$  for each grid point.

### 2.7.2. Solution of the Nuclear TDSE: Split Operator Method

The TDSE is used to study the motion of the nuclear wavepacket. The TDSE can be written using the evolution operator  $U$  [51, 75]. The evolution operator is used to propagate the wavefunction for an interval of time, from  $t_0$  to  $t$ . The solution of the TDSE equation can be written in the following form:

$$|\psi(t)\rangle = \exp\left[-\frac{i}{\hbar}H(t)\right] |\psi(t_0)\rangle = U(t, t_0) |\psi(t_0)\rangle \quad (2.103)$$

In general, the Hamilton operator is time-independent, i.e.  $H(t) = H_{mol} - \vec{\mu} \cdot \vec{E}(t)$ . In this case, use discrete time  $t_i = i\Delta t$ , and approximate  $H(t) = H(t'_i) \approx \text{constant}$  for time intervals  $[t_{i-1}, t_i]$ . Then propagate from  $t_0$  to  $t_1$  using  $H(t'_0)$ , from  $t_1$  to  $t_2$  using  $H(t'_1)$ , etc. The approximate result is

$$\begin{aligned} |\psi(t)\rangle \approx & \exp\left[-\frac{i}{\hbar}H(\tilde{t}_n)\Delta t\right] \cdot \exp\left[-\frac{i}{\hbar}H(\tilde{t}_{n-1})\Delta t\right] \\ & \cdots \exp\left[-\frac{i}{\hbar}H(\tilde{t}_1)\Delta t\right] \cdot \exp\left[-\frac{i}{\hbar}H(\tilde{t}_0)\Delta t\right] |\psi(t_0)\rangle \end{aligned} \quad (2.104)$$

where  $\tilde{t}_i$  is chosen in the time interval  $[t_{i-1}, t_i]$  and  $\Delta t = t_i - t_{i-1}$ . Formally, Eq.(2.104) can be written as

$$\begin{aligned} |\psi(t)\rangle &\approx T_t \exp \left[ -\frac{i}{\hbar} \left( H(\tilde{t}_n)\Delta t + H(\tilde{t}_{n-1})\Delta t \cdots H(\tilde{t}_1)\Delta t + H(\tilde{t}_1)\Delta t \right) \right] |\psi(t_0)\rangle \\ &= T_t \exp \left[ -\frac{i}{\hbar} \sum_{i=0}^n H(\tilde{t}_i)\Delta t \right] |\psi(t_0)\rangle \\ &\approx T_t \exp \left[ -\frac{i}{\hbar} \int_0^t H(t') dt' \right] |\psi(t_0)\rangle = U(t, t_0) |\psi(t_0)\rangle \end{aligned} \quad (2.105)$$

where  $T_t$  is time ordering operator, which is necessary because  $H(t)$  do not commute if  $H(t)$  is time-dependent. If the system is conservative, i.e. the total energy of the molecule is constant, the Hamilton operator is time-independent ( $H \neq H(t)$ ) then the evolution operator can be written as follows:

$$U(t, t_0) = e^{-\frac{i}{\hbar} H(t-t_0)} \quad (2.106)$$

### The Split Operator

There are various propagation schemes to solve the TDSE, e.g. the *Second order differentiator* [76, 77], the *Chebyshev polynomial expansion* [78] or the *split operator*. The simulation in this work done using the split operator, therefore, in this section we will focus on the *split operator* method [79, 80]. Since the commutator between  $\mathbf{T}$  and  $\mathbf{V}$  is not equal to zero, the evolution operator  $e^{-\frac{i}{\hbar} H \Delta t}$  cannot be split into kinetic and potential term, i.e.

$$e^{-\frac{iH\Delta t}{\hbar}} = e^{-\frac{i(T+V)\Delta t}{\hbar}} \neq e^{-\frac{iT\Delta t}{\hbar}} e^{-\frac{iV\Delta t}{\hbar}} \quad (2.107)$$

Nevertheless, one can use an approximation where the propagator can be split into three parts, with error in third order of  $\Delta t$  [79, 80, 81, 82, 83]:

$$e^{-\frac{iH\Delta t}{\hbar}} = e^{-\frac{i(T+V)\Delta t}{\hbar}} \approx e^{-\frac{iT\Delta t}{2\hbar}} \cdot e^{-\frac{iV\Delta t}{\hbar}} \cdot e^{-\frac{iT\Delta t}{2\hbar}} + \mathcal{O}(\Delta t)^3 \quad (2.108)$$

or

$$e^{-\frac{iH\Delta t}{\hbar}} \approx e^{-\frac{iV\Delta t}{2\hbar}} e^{-\frac{iT\Delta t}{\hbar}} e^{-\frac{iV\Delta t}{2\hbar}} + \mathcal{O}(\Delta t)^3 \quad (2.109)$$

Each propagation step using the propagator specified in Eq. (2.108) consists of several Fourier Transforms (FT) between momentum and position space, and also of the evalua-

tions of  $V$  and  $T$ . First, a forward FT of  $|\Psi(\vec{s}, t_0)\rangle$  to the momentum space is performed, then result is multiplied with  $e^{-\frac{iT\Delta t}{2\hbar}}$ . Also the potential energy will be evaluated by multiplying with  $e^{-\frac{iV\Delta t}{2\hbar}}$  after applying the backward FT to obtain the wavefunction in position space. Using another forward FT to the momentum space will evaluate a new  $T$ . In order to obtain the wavefunction  $|\Psi(t)\rangle$  at  $t = t_0 + \Delta t$ , a backward FT to the position space applied. The information about the whole wavefunction  $|\Psi(t_0)\rangle$  from time  $t_0$  to  $t_f = t_0 + n\Delta t$  can be gained after performing a number  $n$  of the above steps.

In diabatic picture for more than one state, the propagation is more complicated since the potential matrix is not diagonal, the time evaluation operator for the diabatic picture has the following form [84]:

$$\begin{aligned} & \exp \left[ -\frac{i}{\hbar} \begin{pmatrix} T_{\text{nuc}} + W_{22} & W_{21} & W_{20} \\ W_{12} & T_{\text{nuc}} + W_{11} & W_{10} \\ W_{02} & W_{01} & T_{\text{nuc}} + W_{00} \end{pmatrix} \Delta t \right] \\ &= \exp \left[ -\frac{i}{\hbar} \begin{pmatrix} T_{\text{nuc}} & 0 & 0 \\ 0 & T_{\text{nuc}} & 0 \\ 0 & 0 & T_{\text{nuc}} \end{pmatrix} \Delta t - \frac{i}{\hbar} \mathbf{W} \Delta t \right] \end{aligned} \quad (2.110)$$

In the split operator method, Eq. (2.110) is approximated by

$$\begin{aligned} \exp \left[ -\frac{i}{\hbar} (T_{\text{nuc}} + \mathbf{W}) \Delta t \right] &\approx \exp \left[ -\frac{i}{\hbar} \frac{T_{\text{nuc}} \mathbf{1}}{2} \Delta t \right] \exp \left[ -\frac{i}{\hbar} \mathbf{W} \Delta t \right] \\ &\quad \exp \left[ -\frac{i}{\hbar} \frac{T_{\text{nuc}} \mathbf{1}}{2} \Delta t \right] + \mathcal{O}(\Delta t)^3 \end{aligned} \quad (2.111)$$

The exponential containing the diabatic potential matrix can be written as

$$\exp \left[ -\frac{i}{\hbar} \mathbf{W} \Delta t \right] = \exp \left[ -\frac{i}{\hbar} \mathbf{A}^\dagger \mathbf{V} \mathbf{A} \Delta t \right] \quad (2.112)$$

$$\begin{aligned} &= \sum_{n=0}^{\infty} \frac{1}{n!} \left( -\frac{i}{\hbar} \mathbf{A}^\dagger \mathbf{V} \mathbf{A} \Delta t \right)^n \\ &= \sum_{n=0}^{\infty} \frac{1}{n!} \left( -\frac{i\Delta t}{\hbar} \right)^n \mathbf{A}^\dagger \mathbf{V}^n \mathbf{A} \\ &= \mathbf{A}^\dagger \exp \left[ -\frac{i}{\hbar} \mathbf{V} \Delta t \right] \mathbf{A} \end{aligned} \quad (2.113)$$



Therefore, the nuclear wavefunction can be propagated as follows:

$$|\psi(t + \Delta t)\rangle = \exp\left[-\frac{i}{\hbar}\frac{T_{\text{nuc}}\mathbf{1}}{2}\Delta t\right]\mathbf{A}^\dagger \exp\left[-\frac{i}{\hbar}\mathbf{V}\Delta t\right]\mathbf{A} \exp\left[-\frac{i}{\hbar}\frac{T_{\text{nuc}}\mathbf{1}}{2}\Delta t\right]|\psi(t)\rangle \quad (2.114)$$

The time step must be very small in order to get reliable results. In accordance of uncertainty principle, the time step  $\Delta t$  must not exceed a critical time step  $\Delta t_c$  which is related to the maximum energy of the system by

$$\Delta t_c = \frac{\hbar}{E_{\text{max}}} \quad \text{with} \quad E_{\text{max}} = T_{\text{max}} + V_{\text{max}} \quad (2.115)$$

The maximum potential energy  $V_{\text{max}}$  is given by the potential energy surface on the respective grid. For the maximum kinetic energy on the same grid the following expression is used:

$$T_{\text{max}} = \frac{\hbar^2\left(\frac{\pi}{\Delta x}\right)^2}{2m} \quad (2.116)$$

where  $\Delta x$  is constant spacing of  $N$  grid points in the position space and  $m$  is the mass. This method is unconditionally stable and norm preserving [89].

## 2.8. Molecular Symmetry (MS)

Molecular symmetry is a fundamental concept in chemistry, as it can predict or explain many molecular properties, such as selection rules for spectroscopic transitions [43]. The symmetry operations which define the molecular symmetry (MS) group are the operations that leave the Hamiltonian of the system globally invariant, i.e. operator that commute with the Hamiltonian. In contrast, molecular point group only describes the local structure like minima, transition states and conical intersections.

The symmetry operations include the permutation of identical nuclei and the inversion of a molecule in space [43]. For example, Figure 2.1 shows the water molecule which consist two protons labelled "1" and "2" and oxygen atom (labelled 3). The nuclear permutation operation of the two identical protons (12) is shown in Figure 2.1a. This operation shows that the two proton position and spin are interchanged without effect the electrons in the molecule. Figure 2.1b shows the effect of the second symmetry operation i.e. the inversion of molecule in it is center of mass. This operation inverts the spatial coordinates of all nuclei and electrons in the molecule [43].

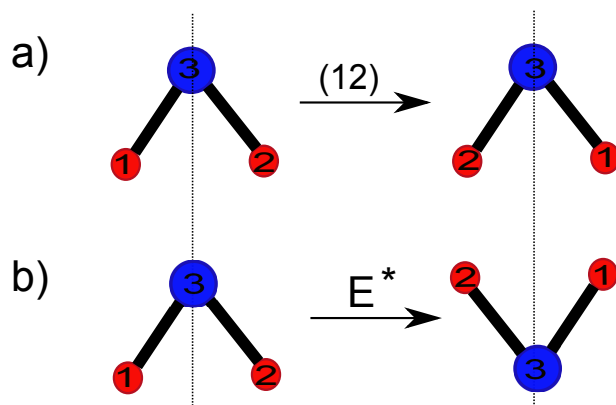


Figure 2.1.: The effect of symmetry operation on water molecule a) the effect of  $(12)$  operation b) The effect of  $E^*$  operation [43].

For every molecule one can define the complete permutation group which contains all possible permutation of identical nuclei. The direct product of the complete permutation and inversion group  $\{E, E^*\}$  yield the complete nuclear permutation inversion group (CNPI). The order of the permutation group is  $n!m!\dots$ , where  $m, n, \dots$  are the number of identical nuclei. As a consequence, the CNPI can be extremely large. It may be reduced to what is known as molecular symmetry (MS) group, which consists of only the feasible elements of the CNPI group.

The character table (for each symmetry group) summarizes information on its symmetry operations and on its irreducible representation (*IREPs*). The number of irreducible representations is always equal to the number of classes of symmetry operation. The table itself consists of characters of the irreducible representations. Any operation in a MS group leaves the molecular Hamiltonian unchanged. For simple groups without degenerate IREPs, the characters are either 1 or -1, where 1 means that the sign or phase (of the vector or orbital) is unchanged by the symmetry operation (*symmetric*) and -1 denotes a sign change (*anti-symmetric*). Character tables also include information about how the Cartesian basis vectors and quadratic function of them transform if the symmetry operations of the group are applied. The following character table shows the  $C_{2v}(M)$  molecular symmetry group:

$C_{2V}(M)$	$E$	$(12)$	$(12)^*$	$E^*$	
$A_1$	1	1	1	1	$r, Z$
$A_2$	1	1	-1	-1	$\phi(\hat{R}_\phi)$
$B_1$	1	-1	1	-1	$y$
$B_2$	1	-1	-1	1	$x$

Table 2.1.: The character table for the  $C_{2v}$  (M) MS group [43].

Later in this study we will implement the molecular symmetry to the non-adiabatic coupling terms. This will determine the IREPs of the NACTs. Besides that, the effect of IREPs of NACTs in the nuclear dynamics will be investigated.



## **3. The Model System**

In this chapter, the model system used in these investigations will be presented. The Cyclopenta-2,4-dienimine  $C_5H_4NH$  will serve as model for assigning the IREPs of the NACTs, locating the CIs and for investigation of molecular symmetry effects on nuclear dynamics.

### 3.1. Cyclopenta-2,4-dienimine $C_5H_4NH$

The Cyclopenta-2,4-dienimine  $C_5H_4NH$  is a challenging model since it is a rather larger exocyclic analogue of methylene-imine  $CH_2NH$ . The  $C=N$  double bond provides two different reaction pathways from reactant (the planar syn-configuration) along a large amplitude motion via three different transition state to the planar anti-configuration of the product (see Figs. 3.1 and 3.2)[71]. In this study, the three lowest electronic states are considered in quantum chemistry calculations and for the investigation of the symmetry properties of  $C_5H_4NH$ . The three electronic state are the electronic ground state  $S_0$  which has a potential minima for the planar syn-configuration and anti- configuration and the two lowest excited singlet states  $S_1$  and  $S_2$ . For purposes of this investigation, i.e. for describing large amplitude motion, the "global" notation  $S_j$ , with  $j = 0, 1, 2$  which indicates the energetic order of the adiabatic potential  $V_j$  is used (instead of employing the notation for the local symmetry). At equilibrium configuration, traditional quantum chemistry assign the notation  $S_0=1A'$ , according to the local *IREPs*  $A'$  of the corresponding molecular point group  $C_s$ . Moreover, the next two excited singlet states for the same geometry have a local  $A'$  symmetry,  $S_1 = 2A'$  and  $S_2 = 3A'$ .

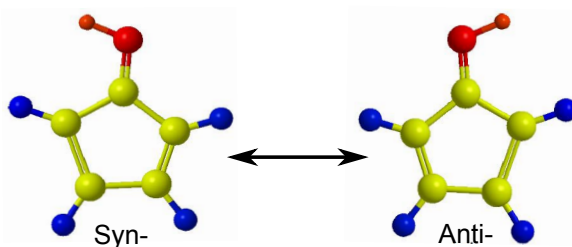


Figure 3.1.: The minimum structures of the syn- and anti-configuration of Cyclopenta-2,4-dienimine geometry.

Conical intersections of  $C_5H_4NH$ , which are related to the syn-anti isomerization, have been located by the group of S. Zilberg (Hebrew University of Jerusalem) [71] with help

of the Longuet-Higgins sign change theorem [15, 16, 17]. The structures of the CIs are shown in fig. 3.2. A  $S_0/S_1$  CI with local  $1A'/1A''$  symmetry has been located 2.80 eV above the ground state for a twisted geometry. Moreover, a triple CI between the states  $S_0$ ,  $S_1$  and  $S_2$  has been discovered with energy of 3.46 eV.

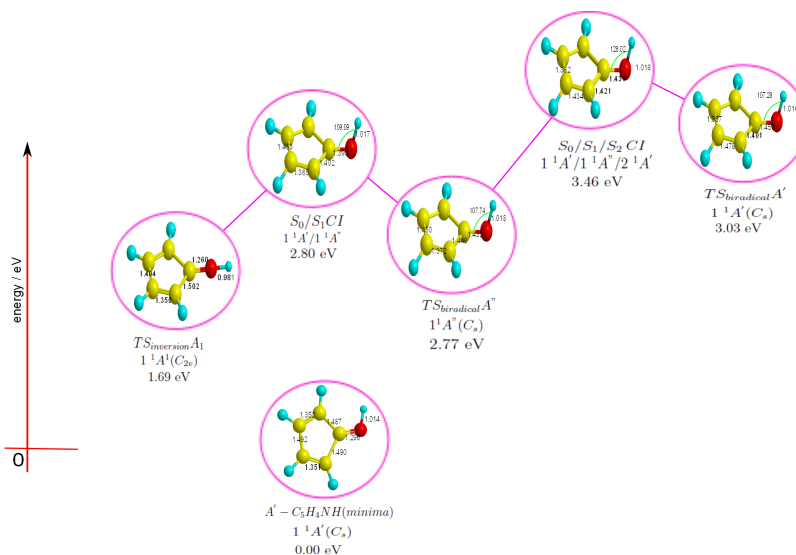


Figure 3.2.: The optimized structures of the ground state minimum (syn-configuration) and the  $S_0/S_1$  CI and  $S_0/S_1/S_2$  CI, with energy relative to the minimum structure. The figure also shows the three transition states which have been used to locate the CIs. The IREPs for the local molecular point groups (NOT the molecular symmetry group) are shown. The geometries are plotted against their relative energy to the minimum of the adiabatic potential  $V_0$  in the electronic ground state. The figure is adapted from ref. [71].

## 3.2. Quantum Chemistry of C<sub>5</sub>H<sub>4</sub>NH

The structures shown in Fig.3.2 (see also Fig.3.3) have been calculated with quantum chemistry methods. All calculations are done using CAS(10,9)/cc-pVDZ level of theory, the CASSCF methodology [126] as implemented in the GAMESS [99] and MOLPRO [32] program. The active space of the CASSCF calculations includes 9 molecular orbitals (MO) occupied by 10 electrons, see Fig. 3.4. The molecular orbitals include 6 $\pi$  orbitals (three occupied  $\pi$  ones and three unoccupied  $\pi^*$  orbitals), together with three  $\sigma$ -type MOs. The  $\sigma$  MOs include the occupied one for the lone electronic pair of the N atom,

the occupied N-H bond MO, and the virtual  $\sigma^*$  (mainly N-H) MO. These  $\sigma$ -MOs were taken into account because the syn-anti isomerization involves a change in hybridization of the N-atom. The full  $\pi$ -active space together with these  $\sigma$ -orbitals provide an adequate description for this part of the PES, using the standard cc-pVDZ basis set. The quantum chemical calculation of the one-dimensional PESs, NACTs and dipole- and transition dipole moments which are required for the present study are performed in the same way.

The CASSCF calculations employ the "local" molecular point groups of these stationary states, as it is adequate for quantum chemistry. The resulting planar geometry of  $C_5H_4NH$  at the potential minimum (it is called the syn- $A'$  form of  $C_5H_4NH$ , with IREP  $A'$  for the local  $C_s$  symmetry) and the three transition states are shown in Fig. 3.3.

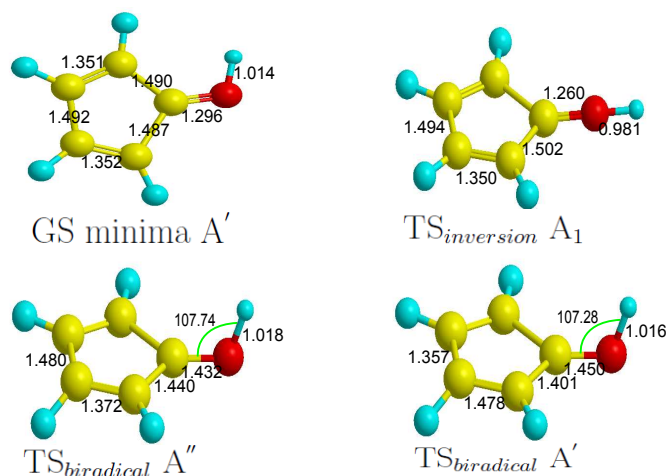


Figure 3.3.: Geometries of the syn-form of  $C_5H_4NH$  in the electronic ground state  $S_0$  (GS), three transition states (TS) with different local IREPs  $A'$  and  $A''$  between the syn- and anti-forms. The results are obtained by performing CAS(10/9)/cc-pVDZ calculations. Here, the IREPs are for the local molecular point groups NOT the molecular symmetry group.



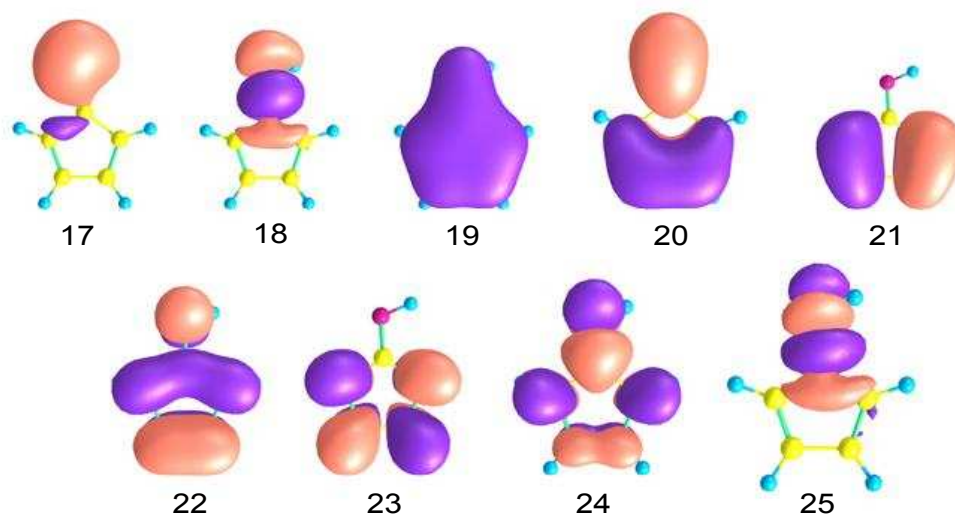


Figure 3.4.: The 9 molecular orbitals (MOs) occupied by 10 electrons used as an active space of the CASSCF calculations. In quantum chemistry calculations the first 16 MOs are assumed frozen while the orbitals from 17 to 25 are assumed to be active.

The "global" molecular symmetry  $C_{2v}(M)$  implies that  $C_5H_4NH$  possesses an equivalent minimum of the PES for the anti-form. The anti-configuration form has the same local IREP  $A'$ . The geometries of the reactant, products and the three transition states are similar except for:

- 1- The hybridization angle (CNH bond angle).
- 2- The CN and NH bond lengths, which are shorter for the  $TS_{inversion}$  than for the minima, due to  $sp$ -hybridization, see Fig. 3.3.
- 3- The torsion angle ( $\phi$ ), i.e. the torsion of the H-atom around the axis of the CN bond in  $C_5H_4NH$ , which is used in this study as one of the adapted coordinate in order to calculate the 1D PES, see Section 4.3.

In the following, we shall use a one-dimensional model of  $C_5H_4NH$  which only includes the torsion angle while keeping the other complementary coordinates frozen. The structures shown in Fig.3.3 have the similar  $C_5H_4N$ -fragments so its reasonable to freeze the coordinates of the  $C_5H_4N$ -fragments in a  $C_{2v}$  symmetry-adapted manner, see Section 4.4.



## 4. Quantum Chemistry and Molecular Symmetry Effects of $C_5H_4NH$

## 4.1. Introduction

The purpose of this chapter is to discover the molecular symmetry properties of conical intersections and related non-adiabatic coupling terms in molecules which allow large amplitude motions such as torsion, focusing on molecular symmetry groups with only one-dimensional irreducible representations. This goal is not only fundamental but also important for application. The NACTs and CIs determine the nonadiabatic processes [45, 10, 101]. If a molecule has CIs at symmetry configuration, the knowledge of the symmetry properties is important for the adequate prediction of the nonadiabatic reaction dynamics, including interferences. Also, the quantum chemical calculations of the NACTs, sepecificly in domains far a way from conical intersection where the absolute values of the NACTs may drop possibly below the level of accuracy of the applied method. In such cases, the symmetry properties of the NACTs determine their relative signs in analogous symmetry-related locations, even far away from each other. The chapter aims to achieve the following points:

- 1- Assigning the molecular symmetry group for C<sub>5</sub>H<sub>4</sub>NH, which undergoes large amplitude motion, i.e. torsion of the proton (H) around the CN axis (Section 4.2).
- 2- Defining the irreducible representations of the symmetry-adapted nuclear coordinates used to generate the one-dimensional PESs. As consequence, their derivatives should transform as the IREPs of MS group (Section 4.3).
- 3- Calculating the adiabatic potential energy surfaces, the conical intersections and the related non-adiabatic coupling terms for the related symmetry-adapted nuclear coordinates (Section 4.4 and 4.5.2).
- 4- Deriving two general theorems which relate to the IREPs of different NACTs to each other.
- 5- Discovering the molecular symmetry properties of conical intersections and related non-adiabatic coupling terms in a molecule (C<sub>5</sub>H<sub>4</sub>NH) which allow large amplitude motion, such as torsion. This will be done in the frame of the relevant molecular symmetry group (Section 4.5).
- 6- Determination of symmetric nodes of the NACTs, together with the (relative) signs of the NACTs in different symmetry-related domains, even far away from the CIs (Section 4.5).
- 7- Defining the signs of the conical intersections and assign their corresponding IREPs (Section 4.5).
- 8- Adiabatic-to-diabatic transformation of adiabatic potential energy surfaces of C<sub>5</sub>H<sub>4</sub>NH

at related symmetry-adapted coordinates (Section 4.6).

## 4.2. The Molecular Symmetry Group of Cyclopenta-2,4-dienimine

The goal of this chapter is to discover molecular symmetry properties of the CIs and the related non-adiabatic coupling terms of  $C_5H_4NH$  in the frame of molecular symmetry groups [43].

In this section, the molecular symmetry group of the model system  $C_5H_4NH$ , see Fig. 3.1, will be defined. In general the MS group consists of  $G$  symmetry operations  $\hat{S}_g$ , with  $g = 1, 2, \dots, G$ . The symmetry operations of a MS group generally include:

- 1- The identity  $\hat{S}_1 = E$ .
- 2- All feasible permutations  $P$  of identical nuclei.
- 3- The inversion  $E^*$  of all nuclear coordinates  $\vec{s}$  and electronic coordinates  $\vec{s}_e$ .
- 4- The inversion-permutations  $P \circ E^*$ .

Applying these symmetry operations to a set of coordinates, say  $\vec{s}_e, \vec{s} = [\vec{s}_e, \vec{s}]_1$  generates a set of other values of the coordinates,

$$[\vec{s}_e, \vec{s}]_g = \hat{S}_g[\vec{s}_e, \vec{s}]_1 \quad \text{with} \quad g = 1, 2, \dots, G. \quad (4.1)$$

These will be called symmetry-related coordinates. They may be far away from each other. Nevertheless, large amplitude motions may provide feasible paths from nuclear coordinates  $[\vec{s}]_1$  to the symmetry-related ones  $[\vec{s}]_g$  [43].

A molecular symmetry group with only one-dimensional IREPs possesses  $G$  IREPs denoted as  $\Gamma_g$ , with  $g = 1, \dots, G$ , say  $\Gamma_1 = A_1, \Gamma_2 = A_2, \Gamma_3 = B_1, \dots$  etc. For one-dimensional IREPs, the symmetry projection operators  $\hat{P}^{\Gamma_g}$  with associated characters  $\chi_{g,h}$  are given by

$$\hat{P}^{\Gamma_g} = \frac{1}{G} \sum_{h=1}^G \chi_{g,h} \hat{S}_h. \quad (4.2)$$

These symmetry projection operators  $\hat{P}^{\Gamma_g}$  commute with each other, and also with the

total Hamiltonian of the system,

$$H_{\text{tot}} = T_{\text{nuc}} + \tilde{H}_{\text{el}} \quad (4.3)$$

where  $T_{\text{nuc}}$  is the nuclear kinetic energy operator and  $\tilde{H}_{\text{el}} = H_{\text{el}} + V_{\text{nuc,nuc}}$ , where  $H_{\text{el}}$  is the electronic Hamiltonian as defined in Eq.(2.8). Moreover, they commute also with the electronic Hamiltonian  $H_{\text{el}}$ . As a consequence, the (real-valued) electronic eigenfunctions  $\psi_{\text{el}}^j(\vec{s}_e, \vec{s})$  of  $H_{\text{el}}$ , satisfying the time-independent electronic Schrödinger equation,

$$\tilde{H}_{\text{el}}\psi_{\text{el}}^j(\vec{s}_e, \vec{s}) = V_j(\vec{s})\psi_{\text{el}}^j(\vec{s}_e, \vec{s}) \quad (4.4)$$

transform according to the IREPs of the MS group. The adiabatic potential energy surfaces  $V_j(\vec{s})$  transform according to the totally symmetric IREP. Due to the invariance of  $\tilde{H}_{\text{el}}$  with respect to the  $\hat{S}_g$ , quantum chemistry calculations would yield the same absolute values of the wavefunctions

$$|\psi_{\text{el}}^j([\vec{s}_e, \vec{s}]_1)| = |\psi_{\text{el}}^j([\vec{s}_e, \vec{s}]_2)| = \dots = |\psi_{\text{el}}^j([\vec{s}_e, \vec{s}]_G)|, \quad (4.5)$$

but the relative signs of the  $\psi_{\text{el}}^j([\vec{s}_e, \vec{s}]_g)$  are not provided automatically. It is indeed exceedingly difficult to determine those signs quantum chemically. This deficit is due to the fact that different domains close to the symmetry-related  $[\vec{s}, \vec{s}_e]_g$  with large values of  $|\psi_{\text{el}}^j([\vec{s}, \vec{s}_e]_g)|$  may be separated by rather large domains where the absolute values of the  $|\psi_{\text{el}}^j([\vec{s}, \vec{s}_e]_g)|$  may drop even below the level of accuracy of the quantum chemical method. These may be due to two reason: symmetric nodes which implying sign change or just tunnelling without any change in sign. Quantum chemistry methods fail to discriminate these two cases. As consequence, it is difficult to assign the IREPs of the related NACTs and CIs. This provides one of the motivations for this study, i.e. assigning the IREPs of NACTs and CIs without knowing the IREPs of the wavefunctions. The investigations presented here are restricted to a finite number of electronic states, i.e. the ground state  $S_0$  and few excited states  $S_1, S_2, \dots, S_{j_{\text{max}}}$ .

The model system C<sub>5</sub>H<sub>4</sub>NH allows large amplitude motions, where the H-atom of the NH bond moves around the CN axis, see Fig. 4.1. The C<sub>5</sub>H<sub>4</sub>NH molecule shows only four symmetry operation  $\hat{S}_g$ . They are shown in Fig. 4.1 and consist of:

- 1- The identity  $E$ .
- 2- The inversion  $E^*$ .
- 3- The permutation (12), which shows the simultaneous permutation of the four nuclei of one of the fragments H-C=C-H (labelled "1") of the C<sub>5</sub>H<sub>4</sub>NH ring with the opposite one (labelled "2"), see Fig. 4.1.

4- Inversion permutation  $(12)^* = (12) \circ E$ .

The four ( $G=4$ ) symmetry operations  $\hat{S}_1 = E$ ,  $\hat{S}_2 = (12)$ ,  $\hat{S}_3 = E^*$  and  $\hat{S}_4 = (12)^*$  constitute the molecular symmetry group  $C_{2v}(\text{M})$ , where the notation (M) reminds of the molecular symmetry. The MS group  $C_{2v}(\text{M})$  is isomorphic to the molecular point group  $C_{2v}$ , with corresponding IREPs  $A_1$ ,  $A_2$ ,  $B_1$ , and  $B_2$ . The character table of  $C_{2v}(\text{M})$  is shown in the Table 4.2.

$C_{2v}(\text{M})$	<b>E</b> $\phi$	<b>(12)</b> $\phi - \pi$	<b>E*</b> $-\phi$	<b>(12)*</b> $\pi - \phi$
<b>A<sub>1</sub></b>	1	1	1	1
<b>A<sub>2</sub></b>	1	1	-1	-1
<b>B<sub>1</sub></b>	1	-1	-1	1
<b>B<sub>2</sub></b>	1	-1	1	-1

Table 4.1.: Character table of the molecular symmetry group  $C_{2v}(\text{M})$  of  $\text{C}_5\text{H}_4\text{NH}$ , which is isomorphic to the molecular point group  $C_{2v}$ . The table also shows the effect of the symmetry operations on the torsion angle  $\phi$  as defined in Fig. 4.1.

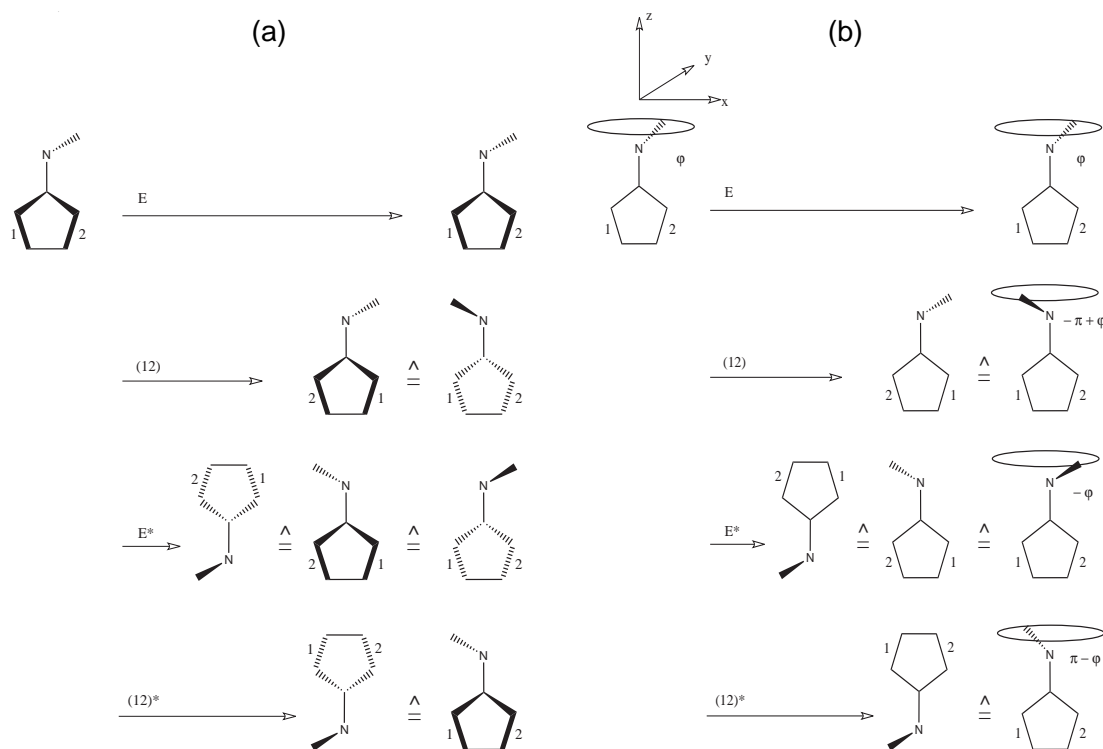


Figure 4.1.: Effects of the four symmetry operations  $E$ ,  $(12)$ ,  $E^*$ , and  $(12)^*$  of the molecular symmetry group  $C_{2v}(M)$  on the model system, with arbitrary configurations (panel (a) courtesy of Prof. Dr. D. Haase), and with constraints to a planar fragment  $C_5H_4N$  with the molecular point group  $C_{2v}$  (panel b). The ring-type trajectory in panel b illustrates the torsion of the NH bond along the torsional angle  $\phi$  and with constant radius  $r$ . The effects of the symmetry operations on  $\phi$  are also illustrated in panel b (see Table 4.2), while  $r$  remains unaffected. Also shown are the orientations of the x- and y-axes for the related coordinates  $x = r \cos \phi$  and  $y = r \sin \phi$ . Adapted from Ref. [71].



### 4.3. Defining the Symmetry-adapted Nuclear Coordinates

The corresponding sets of the molecular symmetry-adapted nuclear coordinates  $\vec{s} = \{s_k\}$ , together with the  $\partial/\partial s_k$  derivatives must be defined. These should be transformed as the IREPs of the MS group, and they should allow to describe the characteristic large amplitude motions of the molecular, as well as vibrations with small amplitudes. In principle, accurate presentations of all coupled vibrations and rotations of a non-linear molecular with  $N_{\text{nuc}}$  nuclei would call for  $3N_{\text{nuc}} - 3$  coordinates  $s_k$ , subtracting 3 coordinates for the motion of the molecular center of mass. Subsequently, the molecule is assumed in the rotational ground state such that the wavefunction does not depend on the rotational Euler angles. All the subsequent results are valid, therefore, for arbitrary re-orientations of the molecule; this assumption has been used implicitly for the molecular rotation which are illustrated in Fig. 4.1. For simplicity, one may also employ models of reduced dimensionality, with explicit considerations of a smaller number of molecular symmetry-adapted coordinates  $s_k$ ,  $k = 1, 2, \dots, n$  (including those which account for the large amplitude motions) while freezing the other ones.

The derivation of the molecular Hamiltonian in reduced dimensionality has been explained in Ref. [107]. These types of n-dimensional models imply constraints on the molecular geometries but not automatically exactly equal to the equilibrium structures. In other words, the reduced dimensionality describes configurations which are close to the reactants, products, transition states, conical intersections and corresponding large amplitude motions between these configurations. It depends on the purpose of the specific investigations, whether the model of reduced dimensionality suffices to provide satisfactory semi-quantitative results, or whether one prefers to include additional degrees of freedom for higher accuracy, at the expense of higher computational demands.

One of the aims of this study is to demonstrate the molecular symmetry properties of the CIs and NACTs. For this case, it is sufficient to use reduced dimensionality and consider only two symmetry adapted coordinates  $\vec{s} = \{s_1, s_2\}$  while freezing the other  $3 \times 11 - 3 - 2 = 28$  coordinates. The fragment  $\text{C}_5\text{H}_4\text{N}$  which includes CN bonds and cyclopentadienyl ring, is frozen in the planar configuration corresponding to the local  $C_{2v}$  molecular point group symmetry, see Fig. 4.2. In this study we restricted our investigation to only two symmetry-adapted coordinates. The chosen coordinates are:

- 1- One of our molecular symmetry-adapted coordinates should describe torsional motion. The torsion angle values cover all space from syn-form of  $\text{C}_5\text{H}_4\text{NH}$  to the anti-form, i.e.  $s_1 = \phi$  with  $-\pi \leq \phi \leq \pi$  which describe the isomerization by torsion of the NH around the axis of the CN bond of the frozen fragment.

- 2- The second symmetry-adapted coordinate is  $s_2 = r$  with  $0 \leq r \leq \infty$  which describes the distance of the proton of the NH bond from the axis of torsion (CN bond axis).

In C<sub>2v</sub>(M) symmetry, the torsion angle  $\phi$  (or more precisely the related torsion  $\hat{R}_\phi$ ) and  $r$ , as well as their derivatives  $\partial/\partial\phi$  and  $\partial/\partial r$ , transform as A<sub>2</sub> and A<sub>1</sub>, respectively, see Table 4.3. Alternatively, one may also employ the related symmetry-adapted Cartesian coordinates:

$$\begin{aligned} x &= r \cos \phi \\ y &= r \sin \phi. \end{aligned} \quad (4.6)$$

These and their derivatives  $\partial/\partial x$  and  $\partial/\partial y$  transform as B<sub>2</sub> and B<sub>1</sub>, respectively, see Table 4.3. Rigorously, the Cartesian coordinates refer to the heavy C<sub>5</sub>H<sub>4</sub>N fragment. The relation (4.6) yields the values of these coordinates depending on the values of the coordinates  $\{r, \phi\}$  which describe the motion of the light proton of the NH-bond relative to C<sub>5</sub>H<sub>4</sub>N.

The effect of applying the symmetry operations  $E$ , (12),  $E^*$ , and (12)\* on the system model C<sub>5</sub>H<sub>4</sub>NH in a constrained configuration space of the two symmetry adapted coordinates  $\phi$  and  $r$  are illustrated in Fig. 4.1(b). As an example, it is assumed that the original configuration is specified by  $[\vec{s}]_1 = [\{r, \phi\}]_1$ , where  $0 \leq \phi \leq \pi/2$ . While keeping the radius  $r$  constant, one readily sees that this transform into symmetry-related structures with torsional angles  $\phi$ ,  $-\pi + \phi$ ,  $-\phi$ , and  $\pi - \phi$ , respectively, covering the entire torsional domain from  $-\pi$  to  $\pi$ , see Table 4.2 and Fig. 4.1. For this reason, the investigation of the symmetry properties of the NACTs and the related CIs is done using arbitrary values of  $\phi$ , while the radius  $r$  is kept as a free but constant parameter. For the present example, Eq.(4.1) reads:

$$\begin{aligned} [\{r, \phi\}, \vec{s}_e]_1 &= E[\{r, \phi\}, \vec{s}_e]_1 = [\{r, \phi\}, \vec{s}_e] \\ [\{r, \phi\}, \vec{s}_e]_2 &= (12)[\{r, \phi\}, \vec{s}_e]_1 = [\{r, -\pi + \phi\}, C_2(z)\vec{s}_e] \\ [\{r, \phi\}, \vec{s}_e]_3 &= E^*[\{r, \phi\}, \vec{s}_e]_1 = [\{r, -\phi\}, \sigma_{xz}\vec{s}_e] \\ [\{r, \phi\}, \vec{s}_e]_4 &= (12)^*[\{r, \phi\}, \vec{s}_e]_1 = [\{r, \pi - \phi\}, \sigma_{zy}\vec{s}_e] \end{aligned} \quad (4.7)$$

see Table 3.3, and Eq.(4.5) is specified as

$$\begin{aligned} |\psi_{\text{el}}^j([\{r, \phi, \vec{s}_e\})| &= |\psi_{\text{el}}^j([\{r, -\pi + \phi, C_2(z)\vec{s}_e\})| = \\ |\psi_{\text{el}}^j([\{r, -\phi, \sigma_{xz}\vec{s}_e\})| &= |\psi_{\text{el}}^j([\{r, \pi - \phi, \sigma_{zy}\vec{s}_e\})|. \end{aligned} \quad (4.8)$$

C <sub>2v</sub> (M)	<b>E</b>	<b>(12)</b>	<b>E*</b>	<b>(12)*</b>	coord. (rotation)	derivatives
<b>A<sub>1</sub></b>	1	1	1	1	r	$\partial/\partial r$
<b>A<sub>2</sub></b>	1	1	-1	-1	$\phi(\hat{R}_\phi)$	$\partial/\partial\phi$
<b>B<sub>1</sub></b>	1	-1	-1	1	y	$\partial/\partial y$
<b>B<sub>2</sub></b>	1	-1	1	-1	x	$\partial/\partial x$

Table 4.2.: Character table of the molecular symmetry group C<sub>2v</sub>(M) of C<sub>5</sub>H<sub>4</sub>N, which indicates the transformation of the relevant coordinates, rotation, and derivatives of the symmetry adapted coordinates.

## 4.4. Calculating the Potential Energy Surfaces of C<sub>5</sub>H<sub>4</sub>NH

The LH theorem helps locating the CIs, which will provide a convenient way to generate the PES. As shown in the previous section, in order to describe the motion along the path of the cis-trans isomerization ( i.e. the paths connecting different reaction pathways between syn- and anti-forms of C<sub>5</sub>H<sub>4</sub>NH, the three TSs and the located CIs) one needs many molecular symmetry-adapted coordinates  $\vec{s} = \{s_k\}$ , see Section 4.3.

To demonstrate MS effects on NACTs and CIs as a proof of principle, it is enough to choose only two coordinates  $\vec{s} = \{s_1, s_2\}$ . The other complementary coordinates are considered to be frozen. The structures shown in Fig. 3.3 have the similar C<sub>5</sub>H<sub>4</sub>N-fragments- so it will be reasonable to freeze the coordinates of the C<sub>5</sub>H<sub>4</sub>N-fragment in a C<sub>2v</sub> symmetry-adapted manner, see Fig. 4.2. This fragment is planar and has local C<sub>2v</sub> symmetry. In contrast, for the S<sub>0</sub>/S<sub>1</sub> CI (1A'/1A''), the five-membered carbon ring turns out to be not exactly planar. More specifically, the shape of the C<sub>5</sub>H<sub>4</sub>NH fragment reminds of the symmetrical (C<sub>s</sub>) wings of a butterfly. These wings are folded away from the planar reference plane by just 0.037 radians (2.1°), with the CN- bond as head of the butterfly, in the (local) vertical symmetry plane between the wings. The two limiting albeit very similar geometries of the C<sub>5</sub>H<sub>4</sub>N fragment for the syn-, anti-forms and for S<sub>0</sub>/S<sub>1</sub> CI suggest, as a compromise, that this fragment should be frozen, the frozen fragment has local C<sub>2v</sub> symmetry, see Fig. 4.2, with the nuclear coordinates close to those of the limiting forms.

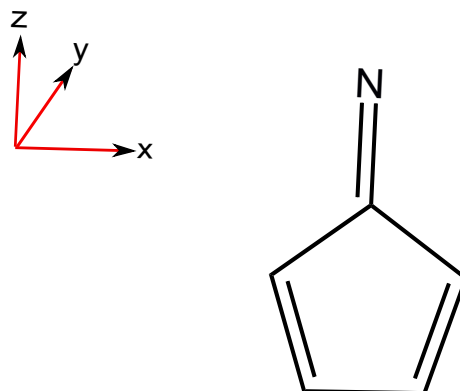


Figure 4.2.: The frozen C<sub>5</sub>H<sub>4</sub>N-fragment in a C<sub>2v</sub> symmetry adapted manner.

For simplicity, all bond lengths and angles of the "butterfly" form of  $S_0/S_1$  CI are frozen, except for the wings which are rotated just slightly by those 0.0367 radians such that the C<sub>5</sub>H<sub>4</sub> ring becomes planar. Moreover, the CN bond is also rotated by just 0.004 radians into the plane of the C<sub>5</sub>H<sub>4</sub> fragment. As a consequence, the local symmetry of the C<sub>5</sub>H<sub>4</sub>N fragment becomes  $C_{2v}$ , with the CN axis as (local)  $C_2$  axis. The distance of the proton of the NH bond from this CN axis is  $r \approx 1.0$  Å. Figure 3.3 shows that all geometries of the C<sub>5</sub>H<sub>4</sub>N fragment are similar to this  $C_{2v}$  structure, not only for  $S_0/S_1$  CI but also for all the other stationary points.

Furthermore, Fig. 4.1 shows that this  $C_{2v}$  geometry is robust with respect to all symmetry operations E, (12),  $E^*$  and (12)\* of  $C_{2v}(M)$ . With this implicit definition of the frozen coordinates, the symmetry-adapted torsional angle  $\phi$  and the complementary radial coordinates  $r$  are defined as two cylindrical coordinates for rotation of the proton of the NH bond around the CN axis, relative to the C<sub>5</sub>H<sub>4</sub>N ( $C_{2v}$ ) fragment. Their (global) IREPs are  $A_2$  and  $A_1$ , respectively, see Table 4.3.

The prize for this reasonable and rather simple choice of just two  $C_{2v}(M)$ -adapted coordinates is that motions along  $\vec{s} = \{r, \phi\}$  may approach geometries of the syn- and anti-forms of C<sub>5</sub>H<sub>4</sub>NH as well as  $S_0/S_1$  CI rather closely but not perfectly. For example, the syn-, anti-forms and the  $S_0/S_1$  CI are approximated for  $\{r, \phi\} = \{r, 0\}$ ,  $\{r, \pm\pi\}$  and  $\{r, \pi/2\}$ , respectively, with  $r \approx 1.0$  Å. As consequence, the energy of the approximated syn-, anti-forms and the  $S_0/S_1$  CI geometries are 0.47 eV and 2.69 eV which differ from the energy of the structure shown in Fig. 3.2, which are 0.00 eV and 2.80 eV, respectively.

The two symmetry-adapted coordinates  $\{r, \phi\}$  are used to calculate the PESs and related NACTs. In this study, three different values of  $r$  are used, i.e.  $r \approx 1.0$ , 0.8 and 1.2 Å, while the range of the torsion angle is  $-\pi \leq \phi \leq +\pi$ , see Fig. 4.3.

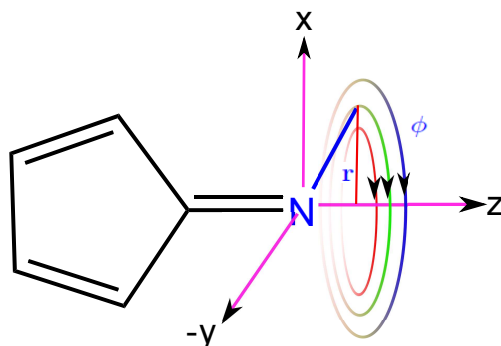


Figure 4.3.: The two symmetry-adapted coordinates  $\vec{s} = \{r, \phi\}$  of Cyclopenta-2,4-dienimine compound, which are used to calculate the PESs and related NACTs.

The resulting adiabatic PES  $V_j$  ( $j=0,1,2$ ) as function of  $\phi$  for  $r \approx 0.8 \text{ \AA}$  is shown in Fig. 4.4. The PES shows two symmetry-adapted avoided crossings between  $V_0$  and  $V_1$  at  $\phi = \pi/2$  and  $-\pi/2$ . The energy gap  $V_1(r \approx 0.8 \text{ \AA}, \phi = \pi/2) - V_0(r \approx 0.8 \text{ \AA}, \phi = \pi/2) = 0.381 \text{ eV}$ . In addition, Fig. 4.4 shows a near degeneracy located between  $V_1$  and  $V_2$  at the coordinates  $[\{r \approx 0.8 \text{ \AA}, \phi \approx 1.047(60^\circ)\}]_1$ , which will be called  $CI_1^{1,2}$ . Applying the symmetry operations of  $C_{2v}(M)$ , i.e. E, (12), E\* and (12)\* to  $CI_1^{1,2}$  will generate a complete set of symmetry-adapted CIs including  $CI_2^{1,2}$  at  $[\{r \approx 0.8 \text{ \AA}, \phi \approx -\pi + 1.047 \approx -2.0946(-120^\circ)\}]_2$ ,  $CI_3^{1,2}$  at  $[\{r \approx 0.8 \text{ \AA}, \phi \approx -1.047(-60^\circ)\}]_3$  and  $CI_4^{1,2}$  at  $[\{r \approx 0.8 \text{ \AA}, \phi^{1,2} \approx \pi - 1.047 \approx 2.0946(120^\circ)\}]_4$ .

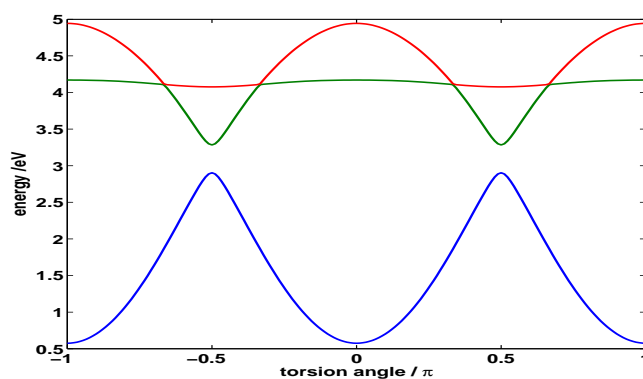


Figure 4.4.: Cut through the PESs with symmetry-adapted coordinates  $\{r \approx 0.8 \text{ \AA}, \phi\}$ , for the ground state energy  $V_0$  (blue line), first excited state  $V_1$  (green line) and the second excited state  $V_2$  (red line).

Figure 4.5 shows the PES for  $r \approx 1.0 \text{ \AA}$ . The figure shows a near degeneracy of  $V_0$  and  $V_1$  with the mean energy  $(V_0+V_1)/2 = 2.69 \text{ eV}$  and with energy gap  $V_1 - V_0 \leq 0.03 \text{ eV}$ , located at  $\{r \approx 1.0 \text{ \AA}, \phi = \pi/2\}$ . This CI named  $CI_1^{0,1}$  confirms the signature of the  $S_0/S_1$  CI which has been located using LH theorem. Applying the symmetry operation generates the second symmetry adapted conical intersection  $CI_2^{0,1}$  at the location  $\{r \approx 1.0 \text{ \AA}, \phi = -\pi/2\}_2$ . Figure 4.5 also shows a near degeneracy of  $V_1$  and  $V_2$ , with the mean energy  $(V_1+V_2)/2 = 3.96 \text{ eV}$  and energy gap  $V_2 - V_1 \leq 0.02 \text{ eV}$ , located at the coordinates  $\{r \approx 1.0 \text{ \AA}, \phi = 0.628(36^\circ)\}$ . By extrapolation, we conclude that this is a signature of a conical intersection  $CI_1^{1,2}$  located at  $\{r \approx 1.0 \text{ \AA}, \phi = 0.628(36^\circ)\}_1$ . The other three conical intersections  $CI_2^{1,2}$ ,  $CI_3^{1,2}$  and  $CI_4^{1,2}$  can be located by applying MS operations. We find that  $CI_2^{1,2}$  is located at  $\{r \approx 1.0 \text{ \AA}, \phi = -\pi + 0.628 = -2.513(-144^\circ)\}_2$ ,  $CI_3^{1,2}$  at  $\{r \approx 1.0 \text{ \AA}, \phi = -0.628(-36^\circ)\}_3$  and  $CI_4^{1,2}$  at  $\{r \approx 1.0 \text{ \AA}, \phi = \pi - 0.628 = 2.513(144^\circ)\}_4$ .

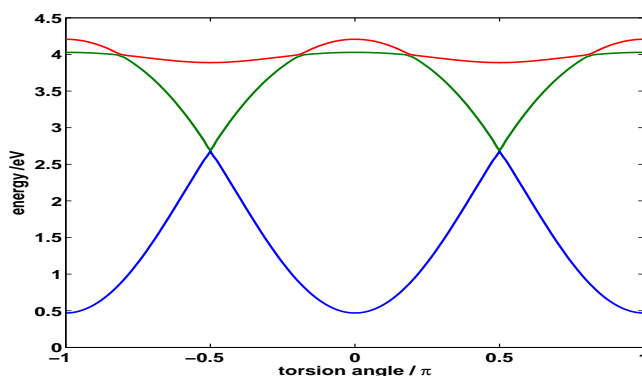


Figure 4.5.: Cut through the PESs with symmetry-adapted coordinates  $\{r \approx 1.0 \text{ \AA}, \phi\}$ , for the ground state energy  $V_0$  (blue line), first excited state  $V_1$  (green line) and the second excited state  $V_2$  (red line)

The adiabatic PES at  $r \approx 1.2 \text{ \AA}$  shows avoided crossing not only for  $V_0$  and  $V_1$  but also for  $V_1$  and  $V_2$ , see Fig. 4.6. These point to neighbouring sets of symmetry adapted  $CI_g^{0,1}$ ,  $g=1,2$  similar to those which have been discovered and confirmed in Fig. 4.4 and Fig. 4.5. Apparently, the locations of the neighbouring  $CI_g^{0,1}$  are at the same torsional angles  $\phi = \pi/2$  and  $-\pi/2$ , whereas pairs of corresponding torsional angles for  $CI_g^{1,2}$  have moved to, and merged at  $\phi = 0, \pm\pi$ .

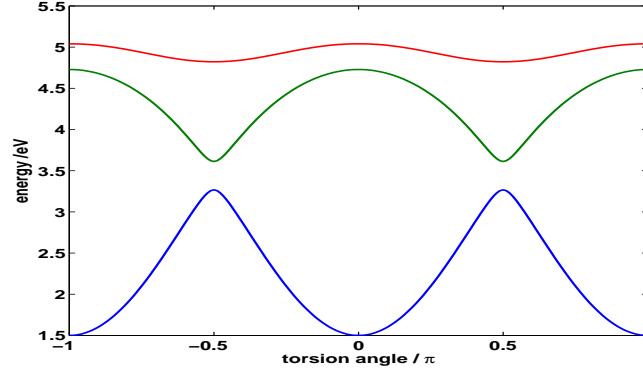


Figure 4.6.: Cut through the PESs with symmetry-adapted coordinates  $\{r \approx 1.2 \text{ \AA}, \phi\}$ , for the ground state energy  $V_0$  (blue line), first excited state  $V_1$  (green line) and the second excited state  $V_2$  (red line)

## 4.5. Symmetry of the NACTs

This section will include a general theorems leading to the assignment of the *IREPs* of the NACTs. The symmetry-adapted nuclear coordinates  $\vec{s} = \{s_k\}$  are used to define the NACTs of the (real-valued) electronic wavefunction  $\psi_{\text{el}}^i(\vec{s}_e, \vec{s})$

$$\tau_k^{i,j}(\vec{s}) = \langle \psi_{\text{el}}^i(\vec{s}) | \frac{\partial}{\partial s_k} \psi_{\text{el}}^j(\vec{s}) \rangle = \int d\vec{s}_e \psi_i(\vec{s}_e, \vec{s}) \frac{\partial}{\partial s_k} \psi_{\text{el}}^j(\vec{s}_e, \vec{s}) = -\tau_k^{j,i}(\vec{s}), \quad (4.9)$$

with  $0 \leq i < j \leq j_{\text{max}}$  and  $\tau^{i,j(1)} = \tau^{i,j}$  where superscript (1) is dropped for simplicity.

At the configurations  $\vec{s} = [\vec{s}^{i,i+1}]_g$  where the  $CI^{i,i+1}([\vec{s}^{i,i+1}]_g)$  are located, the NACTs have poles [3]. The  $\tau_k^{i,j}(\vec{s})$  may be considered as components  $k=1,2,\dots,n$  of the vectorial NACTs,  $\tau^{i,j}(\vec{s})$  for the  $n$ -dimensional model. For reference, we note that in principle, the IREPs of the NACTs (Eq.(4.9)) are given by

$$\begin{aligned} \Gamma(\tau_k^{i,j}) &= \Gamma \left( \psi_{\text{el}}^i(\vec{s}_e, \vec{s}) \frac{\partial}{\partial s_k} \psi_{\text{el}}^j(\vec{s}_e, \vec{s}) \right) \\ &= \Gamma \left( \psi_{\text{el}}^i(\vec{s}_e, \vec{s}) \right) \times \Gamma \left( \frac{\partial}{\partial s_k} \right) \times \Gamma \left( \psi_{\text{el}}^j(\vec{s}_e, \vec{s}) \right) \\ &= \Gamma \left( \tau_k^{j,i} \right), \end{aligned} \quad (4.10)$$

with  $0 \leq i < j \leq j_{max}$ .

The notation  $\Gamma$  in Eq.(4.10) is used for various properties, such as NACTs, the wavefunctions ( $\psi_{el}^j$ ), the derivatives  $\partial/\partial s_k$ , and also for IREPs of other properties such as the product of NACTs and CIs. The third equation in (4.10) follows from the antisymmetry relation (4.9), i.e. it suffices to determine the IREPs of the  $\tau_k^{i,j}$  for  $i < j$ . The task of determining the IREPs of the NACTs would thus be finished if the IREPs of the wavefunction  $\psi_{el}^j$  were known for the given MS group. Since it is difficult, if not even impossible, to provide this information by means of quantum chemistry, an alternative approach to the  $\Gamma(\tau_k^{i,j})$  must be developed. Our starting point comes from relation (4.5) which implies that the wave functions have identical absolute values at symmetry-related nuclear coordinates. As a consequence, the NACTs, Eq.(4.9), also have identical absolute values at symmetry-related coordinates: i.e.

$$|\tau_k^{i,j}([\vec{s}]_1)| = |\tau_k^{i,j}([\vec{s}]_2)| = \dots = |\tau_k^{i,j}([\vec{s}]_G)| \quad (4.11)$$

for  $0 \leq i < j \leq j_{max}$ .

Determination of the IREPs of the  $\tau_k^{i,j}(\vec{s})$  will also provide their relative signs at the symmetry-related nuclear coordinates, Eq.(4.1). Accordingly, for the model system C<sub>5</sub>H<sub>4</sub>NH, the investigation of the molecular symmetry properties should be applied for the radial and torsional NACTs  $\tau_r^{0,1}$ ,  $\tau_r^{0,2}$ ,  $\tau_r^{1,2}$ , and  $\tau_\phi^{0,1}$ ,  $\tau_\phi^{0,2}$ ,  $\tau_\phi^{1,2}$ . The properties of the complementary NACTs  $\tau_r^{1,0}$  ... etc. follow from the anti-symmetry relation, Eq.(4.9). It will also be useful to determine the IREPs with respect to the alternative derivatives  $\partial/\partial x$  and  $\partial/\partial y$ , see Eq.(4.6). Relation (4.11) is specified as

$$|\tau_k^{i,j}(\{r, \phi\})| = |\tau_k^{i,j}(\{r, -\pi + \phi\})| = |\tau_k^{i,j}(\{r, -\phi\})| = |\tau_k^{i,j}(\{r, \pi - \phi\})| \quad (4.12)$$

for  $i, j = 0, 1$  or  $0, 2$  or  $1, 2$  and  $\{\vec{s}_k\} = \{r, \phi\}$  or  $\{x, y\}$ , together with the anti-symmetry relation (4.9).

Next, we will derive two symmetry theorems which relate the IREPs of different NACTs to each other:

- 1- **The first theorem:** Consider two NACTs  $\tau_k^{i,j}$  and  $\tau_l^{i,j}$  for same electronic state  $i, j$  but different derivatives with respect to the two symmetry-adapted coordinates  $s_k$  and  $s_l$ . Then the relation represented in Eq.(4.10) implies that



$$\begin{aligned}\Gamma(\tau_k^{i,j}) \times \Gamma\left(\frac{\partial}{\partial s_l}\right) &= \Gamma(\psi_{\text{el}}^i(\vec{s}_e, \vec{s})) \times \Gamma\left(\frac{\partial}{\partial s_k}\right) \times \Gamma(\psi_{\text{el}}^j(\vec{s}_e, \vec{s})) \times \Gamma\left(\frac{\partial}{\partial s_l}\right) \\ &= \Gamma(\tau_l^{i,j}) \times \Gamma\left(\frac{\partial}{\partial s_k}\right)\end{aligned}\quad (4.13)$$

or

$$\Gamma(\tau_k^{i,j}) = \Gamma\left(\frac{\partial}{\partial s_k}\right) \times \Gamma\left(\frac{\partial}{\partial s_l}\right) \times \Gamma(\tau_l^{i,j}).\quad (4.14)$$

Theorem (4.14) implies that one can assign the IREPs of all the NACT from the IREPs of a single NACTs, for the same electronic state  $i$  and  $j$ .

The symmetry group  $C_{2v}(M)$  for the model system  $C_5H_4NH$  allows to set up four possible combinations of IREPs of the NACTs with respect to the derivatives of the coordinates  $r$ ,  $\phi$ ,  $x$  and  $y$ , see Table 3.3. For example, if  $\Gamma(\tau_r^{i,j}) = A_1$ , then the theorem (4.14) implies that  $\Gamma(\tau_\phi^{i,j}) = A_2$ ,  $\Gamma(\tau_x^{i,j}) = B_2$  and  $\Gamma(\tau_y^{i,j}) = B_1$ . Note, however, that the theorem (4.14) does not suffice per se to decide which of the four possible combinations apply to a given set of electronic states  $i$  and  $j$ .

- 2- **The second theorem** relates the IREPs of NACTs for the derivatives with respect to the same symmetry-adapted coordinate  $\partial/\partial s_k$ , but for different electronic states to each other. For this purpose, consider a loop-type sequence of  $N_{loop}$  molecule states with the same spin multiplicity, see Fig. 4.7.



Figure 4.7.: Model system with  $N_{loop}$  electronic state  $S_a, S_b, S_c, \dots, S_y, S_z=S_a$

The loop consists of  $N_{loop}$  singlet states  $S_a, S_b, S_c, \dots, S_y, S_z = S_a$  and it starts and ends with the same state  $S_a$ , i.e.  $S_z = S_a$ . The corresponding NACTs are

$$\tau_k^{a,b}, \tau_k^{b,c}, \tau_k^{c,d}, \dots, \tau_k^{y,z=a} = \tau_k^{y,a}\quad (4.15)$$

and their product is given by

$$\tilde{\tau}_k^{a,b,c,\dots,y,z=a} = \tau_k^{ab} \tau_k^{bc} \dots \tau_k^{yz=a}. \quad (4.16)$$

Theorem (4.10) implies that the IREPs of  $\tilde{\tau}_k^{a,b,c,\dots,y,z=a}$  can be determined from the product of the IREPs of the underlying electronic wavefunctions  $\psi_{\text{el}}^i(\vec{s}_e, \vec{s})$  and  $\psi_{\text{el}}^j(\vec{s}_e, \vec{s})$  as well as the derivatives of the symmetry-adapted coordinates  $\partial/\partial s_k$ . For one dimensional IREPs, Eq. (4.10) yields

$$\begin{aligned} \Gamma(\tilde{\tau}_k^{a,b,c,\dots,y,z=a}) &= \Gamma[\psi_{\text{el}}^a(\vec{s}_e, \vec{s})]^2 \times \Gamma[\psi_{\text{el}}^b(\vec{s}_e, \vec{s})]^2 \times \\ &\quad \dots \times \Gamma[\psi_{\text{el}}^y(\vec{s}_e, \vec{s})]^2 \times \Gamma\left(\frac{\partial}{\partial s_k}\right)^{N_{\text{loop}}} \\ &= \begin{cases} \Gamma\left(\frac{\partial}{\partial s_k}\right) & \text{if } N_{\text{loop}} \text{ is odd} \\ A_1 & \text{if } N_{\text{loop}} \text{ is even} \end{cases} \end{aligned} \quad (4.17)$$

Theorem (4.17) imposes a condition on the IREPs of the NACTs  $\tau_k^{i,j}$  which contribute to the loop (4.16). Analogous conditions can be derived for similar loops for NACTs  $\tau_k^{a,b} \tau_l^{b,c}$  ...etc. with respect to different symmetry adapted coordinates  $s_k, s_l$  ... etc. But these do not provide any additional information because they can be re-expressed in terms of theorems (4.14) and (4.17).

Implying theorem (4.17) on the model system (C<sub>5</sub>H<sub>4</sub>NH), with considering the lowest three molecular states  $S_0, S_1, S_2$ , i.e.  $N_{\text{loop}} = 3$ , the corresponding NACTs are  $\tau^{0,1}, \tau^{1,2}$  and  $\tau^{0,2}$  thus Eq.(4.16) implies

$$\tilde{\tau}_k^{0,1,2,0} = \tau_k^{0,1} \tau_k^{1,2} \tau_k^{2,0}. \quad (4.18)$$

Considering the symmetry-related coordinates  $\vec{s} = \{r, \phi\}$ , then theorem (4.17) yields the relation of IREPs of the NACTs to their derivatives, with respect to the  $\partial/\partial\phi$  derivatives

$$\Gamma(\tilde{\tau}_\phi^{0,1,2,0}) = \Gamma(\tau_\phi^{0,1}) \times \Gamma(\tau_\phi^{1,2}) \times \Gamma(\tau_\phi^{2,0}) = \Gamma\left(\frac{\partial}{\partial\phi}\right) = A_2. \quad (4.19)$$

Likewise, theorem (4.17) can be applied for the NACTs with respect to the second derivative  $\partial/\partial r$

$$\Gamma(\tilde{\tau}_r^{0,1,2,0}) = \Gamma(\tau_r^{0,1}) \times \Gamma(\tau_r^{1,2}) \times \Gamma(\tau_r^{2,0}) = \Gamma\left(\frac{\partial}{\partial r}\right) = A_1. \quad (4.20)$$

The relations (4.19) and (4.20) for the NACTs with respect to the derivatives  $\partial/\partial\phi$  and  $\partial/\partial r$ , imply symmetry constraints on their IREPs. For example, if the IREPs  $\Gamma(\tau_\phi^{0,1})$  and  $\Gamma(\tau_\phi^{0,2})$  of the two NACTs  $\tau_\phi^{0,1}$  and  $\tau_\phi^{0,2}$  are known with respect to  $\partial/\partial\phi$ , then the IREP of the third one, i.e.  $\Gamma(\tau_\phi^{1,2})$ , will follow automatically from relation (4.19). Consider the case where  $\Gamma(\tau_\phi^{0,1}) = \Gamma(\tau_\phi^{0,2}) = B_1$ : applying relation (4.19) yields

$$\begin{aligned}\Gamma(\tau_\phi^{0,1}) \times \Gamma(\tau_\phi^{1,2}) \times \Gamma(\tau_\phi^{0,2}) &= \Gamma\left(\frac{\partial}{\partial\phi}\right) = A_2 \\ B_1 \times B_1 \times \Gamma(\tau_\phi^{1,2}) &= \Gamma\left(\frac{\partial}{\partial\phi}\right) = A_2 \\ \Gamma(\tau_\phi^{1,2}) &= A_2\end{aligned}$$

Theorem (4.17) establish useful relation between NACTs of the loop of the electronic states. On the other hand, it does not suffice per se to determine the IREPs of all the NACTs, additional steps are necessary, see next. In any case, the two theorems (4.14) and (4.17) are applicable without calculating the electronic wavefunctions or the NACTs explicitly.

In general, theorems (4.14) and (4.17) allows to determine

- 1- the relation between different patterns of signs of the NACTs.
- 2- the corresponding different symmetric nodes for the  $\tau_k^{i,j}(\vec{s})$ , depending on the IREPs of the different derivatives  $\partial/\partial s_k$ .

According to the above two relations one can apply the symmetry operator  $\hat{P}_g$  in order to generate the sign of the  $\tau_k^{i,j}(\{\{s_k\}\}_h)$  at all the symmetry-related locations  $\{\{s_k\}\}_h$ . If the IREP of  $\tau_k^{i,j}(\vec{s})$  is  $\Gamma(\tau_k^{i,j}(\vec{s})) = \Gamma_g$ , and the value of  $\tau_k^{i,j}(\vec{s})$  at a reference location  $\vec{s} = \{\{s_k\}\}_1$  has been determined to be  $\tau_k^{i,j}(\{\{s_k\}\}_1)$ , then the absolute values of the  $\tau_k^{i,j}(\{\{s_k\}\}_h)$  at all symmetry-related coordinates generated by applying the symmetry projection operator  $\hat{P}^{\Gamma_g}$  are identical, see Eq.(4.11), while their patterns of the relative signs may differ depending on the characters  $\chi_{g,h}$  which are involved in the  $\hat{P}_g$ , see Eq.(4.2). Whenever the signs of  $\tau_k^{i,j}(\{\{s_k\}\}_f)$  and  $\tau_k^{i,j}(\{\{s_k\}\}_h)$  are different, there must be a node of  $\tau_k^{i,j}(\vec{s})$  located half-way between  $\{\{s_k\}\}_f$  and  $\{\{s_k\}\}_h$ , i.e.

$$\tau_k^{i,j}(\vec{s}_{fh}) = 0 \quad \text{at} \quad \vec{s}_{fh} = \frac{1}{2} (\{\{s_k\}\}_f + \{\{s_k\}\}_h) \quad (4.21)$$

if

$$\tau_k^{i,j}(\{\{s_k\}\}_f) = -\tau_k^{i,j}(\{\{s_k\}\}_h)$$

for the given IREP,  $\Gamma(\tau_k^{i,j}(\vec{s})) = \Gamma_g$ . The theorem (4.14) implies that the IREPs of  $\tau_k^{i,j}(\vec{s})$  and  $\tau_l^{i,j}(\vec{s})$  differ if  $\Gamma(\partial/\partial s_k) \neq \Gamma(\partial/\partial s_l)$ . By analogy of the derivation of Eq.(4.21), the patterns of the relative signs of the NACTs  $\tau_k^{i,j}(\{\{s_k\}\}_g)$  and  $\tau_l^{i,j}(\{\{s_k\}\}_g)$  at symmetry-related coordinates  $\{\{s_k\}\}_g$ , as well as the corresponding nodes (4.21) should also differ, according to their IREPs.

Applying the above theorem to the model system C<sub>5</sub>H<sub>4</sub>NH will provide lists of schemes of the different patterns of signs of the NACTs, as well as the different nodes, depending on their IREPs. Table 3.3a shows all four possibilities which are in accordance with theorems (4.14) and (4.17). For example, consider the third possibility when  $\Gamma(\tau_x^{i,j}) = A_1$ . The corresponding sign pattern implies that the  $\tau_x^{i,j}(\hat{S}_g[\{r, \phi\}])$  at all symmetry-related values of coordinates  $\hat{S}_g[\{r, \phi\}]$ , Eq.(4.8), have the same sign. This implies that  $\tau_x^{i,j}(\vec{s})$  does not possess any nodes imposed by symmetry, see Fig. 4.8. From  $\Gamma(\tau_x^{i,j}) = A_1$ , it follows that  $\Gamma(\tau_y^{i,j}) = A_2$ . Here, the values  $\tau_y^{i,j}(\hat{S}_g[\{r, \phi\}])$  have a pattern of alternating signs at the symmetry-related locations  $\hat{S}_g[\{r, \phi\}]$ , where both the  $x$ - and  $y$ -axes are nodal lines, see Fig. 4.8. Likewise,  $\tau_\phi^{i,j}$  and  $\tau_r^{i,j}$  have the IREPs B<sub>1</sub> and B<sub>2</sub>, with corresponding different patterns of the relative signs.

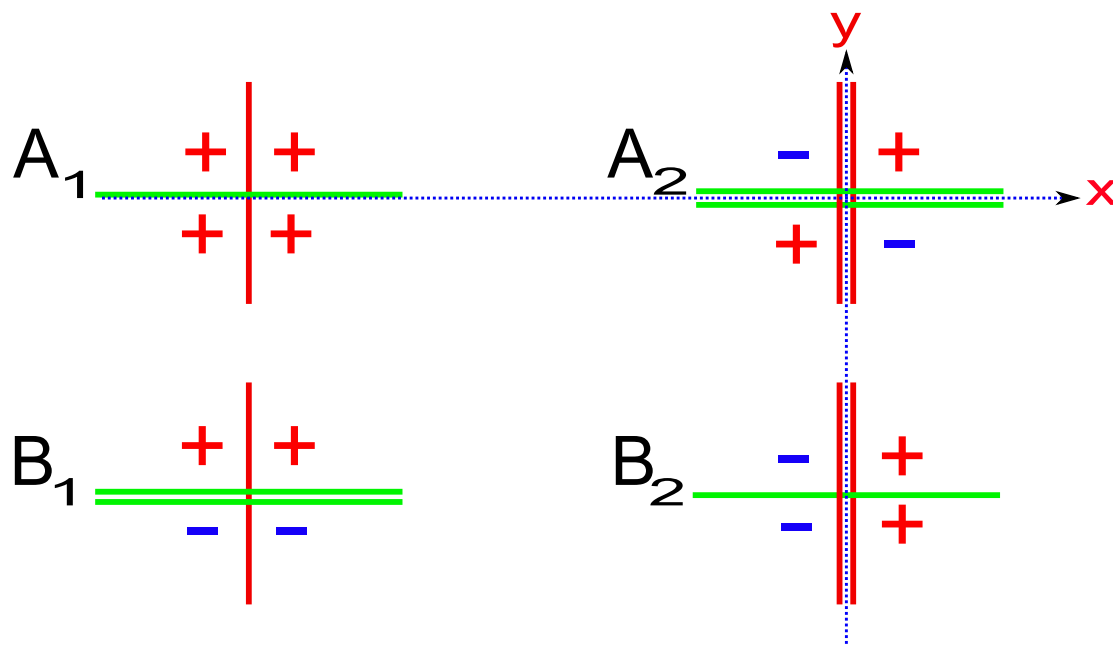


Figure 4.8.: The relative signs and nodes for the wavefunctions, NACTs or CIs at  $\hat{S}_g[\{x, y\}]$ . The + and - signs denote same and opposite relative signs, respectively; horizontal and vertical double lines indicate nodes at the x and y axis, respectively.





$C_{2v}(M)$ $\hat{S}_g$	E $\hat{S}_1$	$(12)$ $\hat{S}_2$	$E^*$ $\hat{S}_3$	$(12)^*$ $\hat{S}_4$	coord. (rotation)	deriv.	1st	(a) 2nd	3rd	4th
$A_1$	1	1	1	1	$r$	$\partial/\partial r$	$\tau_\phi$	$\tau_r$	$\tau_x$	$\tau_y$
$A_2$	1	1	-1	-1	$\phi (\hat{R}_\phi)$	$\partial/\partial \phi$	$\tau_r$	$\tau_\phi$	$\tau_y$	$\tau_x$
$B_1$	1	-1	-1	1	$y$	$\partial/\partial y$	$\tau_x$	$\tau_y$	$\tau_\phi$	$\tau_r$
$B_2$	1	-1	1	-1	$x$	$\partial/\partial x$	$\tau_y$	$\tau_x$	$\tau_r$	$\tau_\phi$
application to $C_5H_4NH$							-	$\tau_k^{12}$	$\tau_k^{01}$	-
$(r, \phi) \rightarrow \hat{S}_g(r, \phi)$ $(x, y) \rightarrow \hat{S}_g(x, y)$	$(r, \phi)$ $(x, y)$	$(r, -\pi + \phi)$ $(-x, -y)$	$(r, -\phi)$ $(x, -y)$	$(r, \pi - \phi)$ $(-x, y)$	(b) (c)					
sym.-related locations $\hat{S}_g(x, y)$					(d)					

Table 4.3.: Character table of the molecular symmetry group  $C_{2v}(M)$  of  $C_5H_4NH$ , with extensions, see Fig. 4.1. (a) Four possible combinations of IREPs of the NACTs. Short-hand notation  $\tau_k$  denotes the NACT  $\tau_k^{ij}$  for unspecified electronic states  $i$  and  $j$ , with respect to the derivative for the nuclear coordinates  $s_k = r, \phi, x$  or  $y$ . Applications of the 2nd and 3rd possible combinations for the NACTs of  $C_5H_4NH$  are specified below. (b) Effects of the symmetry operations  $\hat{S}_g$  yielding symmetry-related molecular structures with same radius  $r$  and but different torsional angles, cf. Fig. 4.1(b) (c) Effects of the symmetry operations  $\hat{S}_g$  yielding symmetry-related molecular structures with different Cartesian coordinates. (d) Symmetry-related top right, bottom left, bottom right, top left locations correspond to  $\hat{S}_g(x, y)$  with  $g=1,2,3,4$ , respectively.

### 4.5.1. Assigning the IREPs of NACTs

To assign the IREPs of the NACTs one needs additional information about the NACTs. The previous information and results, in particular the two general theorems (4.14) and (4.17) together with the consequences for the patterns of the relative signs and nodes of the NACTs, are quite useful. On the other hand, they do not always provide enough information to assign the IREPs of the NACTs. In general, the amount of information that is required in order to specify the IREP depends on the size  $G$  of the molecular symmetry group. All groups which are isomorphic to molecular point groups, can be constructed by means of a maximum of three symmetry operations  $\hat{S}_h$  which serve as generators. Accordingly, it suffices to specify no more than three (non-trivial, i.e. beyond  $\chi_{g,E} = 1$  for the identity  $E$ ) characters  $\chi_{g,h}$ , in order to deduce the corresponding IREP  $\Gamma_g$  [43].

As a consequence, three items (or even less) of information depending on the size of the MS group, should be sufficient to assign the IREPs of the NACTs (The two theorems (4.14) and (4.17) are also applicable). The following items specify three additional properties of the NACTs between two successive isolated state  $(\psi_{\text{el}}^i, \psi_{\text{el}}^{i+1})$  related to the CIs [3, 10]. These and another property which involves a third electronic state will provide complementary information needed to assign the IREPs of the NACTs:

- 1- If a single point  $CI_g^{i,i+1}$  is enclosed by a contour, then the contour integrals over the  $\tau_k^{i,i+1}(\vec{s}|L_g)$  calculated along a closed loop must satisfy a quantization rule [3]. This implies that the contour integrals are equal to  $+\pi$  or  $-\pi$ , which depends on the IREP-adapted signs of the  $\tau^{i,i+1}$  close to  $\vec{s}^{i,i+1}$ . If the loop  $L_g$  encloses one single  $CI_g^{i,i+1}$ , then

$$\oint ds \cdot \tau^{i,i+1}(\vec{s}|L_g) = \pm\pi = e_g^{i,i+1}\pi \quad (4.22)$$

where  $e_g^{i,i+1} = \pm 1$  denotes the sign of the  $CI_g^{i,i+1}$ . Else, if the loop does not enclose any  $CI_g^{i,j}$

$$\oint ds \cdot \tau^{i,i+1}(\vec{s}|L_g) = 0. \quad (4.23)$$

Here, the dot represents a scalar product of the vectorial NACTs  $\tau^{i,i+1}(\vec{s}|L_g)$ , which have components  $\tau_k^{i,i+1}(\vec{s}|L_g)$ , and  $d\vec{s}$  with respect to the symmetry adapted coordinates  $\vec{s} = \{s_k\}$ , respectively. The integrations (4.22) and (4.23) are over the tangential components of  $\tau^{i,i+1}$ . For convenience, the loops  $L_g$  of the contour integrals is constructed as a closed sequence of lines along individual symmetry-adapted coordinates.

**Remark:** The quantization rule (4.22) holds if and only if the loop is sufficiently close to the  $CI_g^{i,i+1}(\vec{s}^{i,i+1})$  such that the NACTs due other states  $j \neq i, i+1$  do not

interfere significantly; this corresponds to the two-state model [3]. Else, interfering give rise to more general quantization rule [3, 111]. The quantization rule for the NACTs has been exploited previously [34] in order to reveal a conical intersection in a given region of configuration space [3].

- 2- The second additional information is the pole property. The  $\tau_k^{i,i+1}(\vec{s})$  have poles and their values diverge to  $\pm\infty$  as the coordinates  $\vec{s}$  approach the  $CI^{i,i+1}(\vec{s}^{i,i+1})$  [3],

$$\tau_k^{i,i+1}(\vec{s}) \rightarrow \pm\infty \quad \text{for} \quad \vec{s} \rightarrow (\vec{s}^{i,i+1}) \quad (4.24)$$

It depends on the signs imposed by their IREPs, if the values diverge to  $+\infty$  or  $-\infty$ .

- 3- The third information is related to the character of the wave function. The wave function  $\psi_{\text{el}}^j(\vec{s}_e, \vec{s})$  and  $\psi_{\text{el}}^{j+1}(\vec{s}_e, \vec{s})$  may change characters as the nuclear coordinates  $\vec{s}$  pass from one side, say the "left,  $\vec{s}_l$ " hand side across the seam of  $CI^{j,j+1}(\vec{s}^{j,j+1})$  to opposite side, say the "right,  $\vec{s}_r$ " hand side, see Fig. 4.9. For example, if  $\psi_{\text{el}}^j(\vec{s}_e, \vec{s}_l)$  and  $\psi_{\text{el}}^{j+1}(\vec{s}_e, \vec{s}_r)$  represent essentially covalent or biradical types of bonding, then these characters may switch to  $\psi_{\text{el}}^{j+1}(\vec{s}_e, \vec{s}_r)$  and  $\psi_{\text{el}}^j(\vec{s}_e, \vec{s}_l)$ , respectively. The molecular symmetry implies that if the two wavefunctions change their characters near to the specific configuration of the seam  $[\vec{s}^{j,j+1}]_1$ , then equivalent switches occur at all other symmetry-adapted coordinates  $[\vec{s}^{j,j+1}]_g$  close to the CIs. As a consequences, the two wave functions  $\psi_{\text{el}}^j$  and  $\psi_{\text{el}}^{j+1}$  have the same IREPs. Then the NACTs  $\tau_k^{i,j}(\vec{s})$  and  $\tau_k^{i,j+1}(\vec{s})$  between two different states  $i < j, j+1$  should also interchange according to the definition (4.21). Also, the relation (4.10) yields the same IREPs for the NACTs  $\tau_k^{i,j}(\vec{s})$  and  $\tau_k^{i,j+1}$ , (see Table 3.3)

$$\Gamma(\tau_k^{i,j}) = \Gamma(\tau_k^{i,j+1}) \quad (4.25)$$

in case of a switch close to  $CI^{j,j+1}(\vec{s}^{j,j+1})$

$$\tau_k^{i,j}(\vec{s}_l) \rightarrow \tau_k^{i,j+1}(\vec{s}_r) \quad (4.26)$$

$$\tau_k^{i,j+1}(\vec{s}_l) \rightarrow \tau_k^{i,j}(\vec{s}_r) \quad (4.27)$$



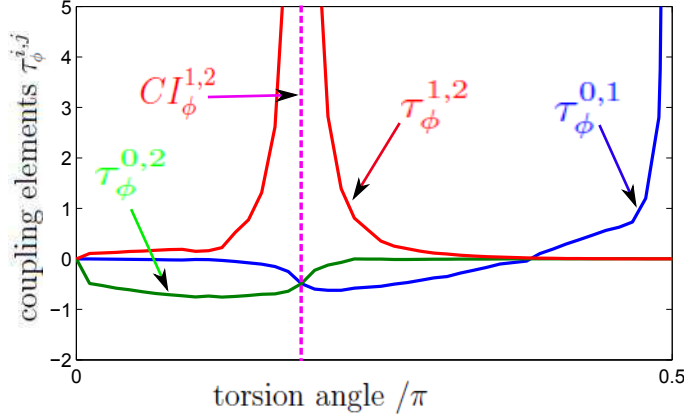


Figure 4.9.: The non-adiabatic coupling terms (NACTs) of  $C_5H_4NH$  with  $r \approx 1.00 \text{ \AA}$ ,  $\tau_{\phi}^{0,1}$  (blue lines),  $\tau_{\phi}^{0,2}$  (green lines) and  $\tau_{\phi}^{1,2}$  (red lines) (For calculation of NACTs see Section 4.5.2).

In the following, we apply these three additional pieces of information to identify the IREPs of the NACTs. The determination of the IREPs of the associated  $\tau_k^{i,i+1}(\phi, r)$  is reduced to the determination of the appropriate combination of IREPs of the NACTs. This reduction is a consequence of theorem (4.17). Table 3.3 shows four possibility combination of the IREPs of the NACTs for model system  $C_5H_4NH$ . In order to find the appropriate combination of IREPs of the NACTs  $\tau_k^{i,i+1}(\phi, r)$ , two cases of  $CI^{i,i+1}(\vec{s}^{i,i+1})$  located at different symmetry-adapted coordinates are considered. The first case has  $CI^{i,i+1}(\vec{s}^{i,i+1})$  located at specific values of the symmetry-related coordinates  $[\vec{s}^{i,i+1}]_1 = [\{r^{i,i+1}, \phi^{i,i+1} = \pi/2\}]_1$ , while the second case has the  $CI^{i,i+1}(\vec{s}^{i,i+1})$  located at  $[\vec{s}^{i,i+1}]_1 = [\{r^{i,i+1}, \phi^{i,i+1} = 0\}]_1$ . The two properties (4.22) and (4.24) of the CIs will be applied for these two cases as follows:

- 1- **The first case:** The CI is located at the symmetry-related coordinates  $[\vec{s}^{i,i+1}]_1 = [\{r^{i,i+1}, \phi^{i,i+1} = \pi/2\}]_1$ , see Fig. 4.10. For this purpose, the quantization rule (4.22) for  $CI^{i,i+1}(\{r^{i,i+1}, \phi^{i,i+1} = \pi/2\})$ , as specified in Eq.(4.28), is applied in order to eliminate two of four possible combinations of IREPs of the NACTs, see Table 3.3. Figure 4.10 schematically illustrates the conical intersection  $CI_1^{i,i+1}([\vec{s}^{i,i+1}]_1)$  located at coordinates  $[\vec{s}^{i,i+1}]_1 = [\{r^{i,i+1}, \phi^{i,i+1} = \pi/2\}]_1$ . In order to apply the quantization rule (4.22), the loop  $L_1$  is constructed around  $CI_1^{i,i+1}([\vec{s}^{i,i+1}]_1)$ , as shown in Fig. 4.10(a). The contour integral Eq.(4.28) consists of three contributions,  $I_{tor}$

along torsional angle  $\phi$ , from  $\phi = \phi_2$  to  $\pi - \phi_2$  and two radial lines with opposite directions along the radial coordinates  $r$ , from 0 to  $r_1$  and from  $r_1$  to 0, respectively.

$$\oint d\vec{s} \cdot \tau^{i,i+1}(\vec{s}|L_1) = I_{tor} + I_{rad,1} + I_{rad,2} = e_1^{i,i+1}\pi, \quad (4.28)$$

where

$$I_{tor} = \int_{\phi_2}^{\pi-\phi_2} d\phi \tau_{\phi}^{i,i+1}(r_1, \phi|L_1), \quad (4.29)$$

$$I_{rad,1} = \int_0^{r_1} dr \tau_r^{i,i+1}(r, \phi_2|L_1), \quad (4.30)$$

$$I_{rad,2} = \int_{r_1}^0 dr \tau_r^{i,i+1}(r, \pi - \phi_2|L_1). \quad (4.31)$$

Since loop  $L_1$  encloses one CI, the absolute value of the contour integral Eq.(4.28) should be equal to  $\pi$  [3]. The sign or "charge"  $e_1^{i,i+1}$  is arbitrary because the signs of the underlying wavefunctions  $\psi_{el}^i$  and  $\psi_{el}^{i+1}$  are arbitrary, see Eq.(4.9). The choice  $e_1^{i,i+1} = +1$  in Eq.(4.28) is made ad hoc, for convenience of the subsequent illustrations, which implies corresponding consistent sets of relative (same or opposite) signs or charges of all the NACTs and CIs, but it will not affect any of the subsequent conclusions. Accordingly, we assign the charge  $e_1^{i,i+1} = 1$  to the  $CI^{i,i+1}(\{r^{i,i+1}, \phi^{i,i+1} = \pi/2\}_1)$ , as shown in Fig. 4.10. The symmetry properties of the NACTs are derived from their values at symmetry-related locations on the loop, which are indicated by stars \* on the torsional line and by cross + on the radial lines.

The specification (4.28) of the quantization rule (4.22) will now allow us to eliminate the 2nd and 4th combinations of the IREPs of the NACTs which have been specified in Table 3.3. The two combination have alternating relative signs of the  $\tau_{\phi}^{i,i+1}(r_1, \phi)$  at the symmetry-related coordinates, e.g. see the stars on the loop  $L_1$  in Fig. 4.10(a). As a consequence, these alternating sign of the  $\tau_{\phi}^{i,i+1}(r_1, \phi)$  have a compensating effect on the torsional integral (4.29), hence  $I_{tor} = 0$ . Moreover, the NACTs  $\tau_r^{i,i+1}(r, \phi_2|L_1)$  and  $\tau_r^{i,i+1}(r, \pi - \phi_2|L_1)$  which contribute to the radial integrals (4.30) and (4.31), respectively, are identical (e.g. see the crosses + on the loop  $L_1$  in Fig. 4.10(a)). This implies that  $I_{rad,1} = -I_{rad,2}$ . As a consequence, the 2nd and 4th combinations of IREPs would yield  $I_{tor} + I_{rad,1} + I_{rad,2} = 0$ , which is incompatible with the quantization rule (4.28) for the NACTs.

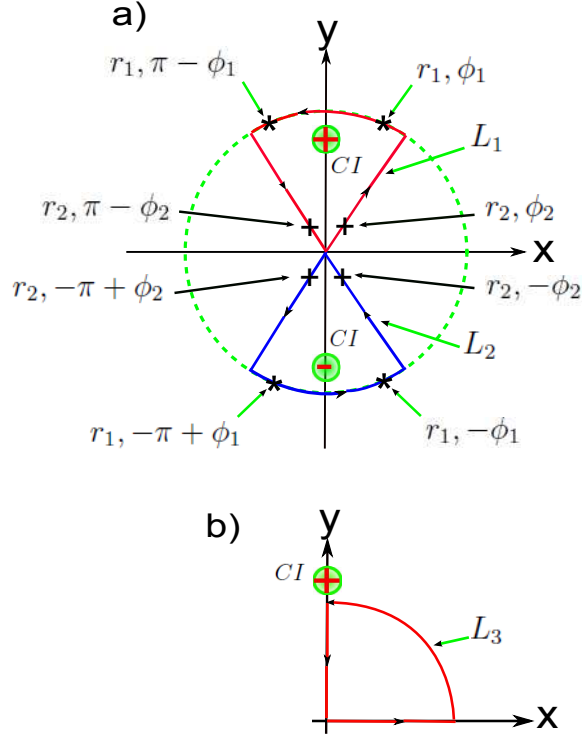


Figure 4.10.: Assigning the IREPs of the NACTs  $\tau_k^{i,i+1}(\vec{s})$  and the corresponding IREPs of the seams of the CIs. In this case the  $CI_1^{i,i+1}$  has been discovered at the symmetry-adapted coordinates  $[\vec{s}^{i,i+1}]_1 = [\{r^{i,i+1}, \phi^{i,i+1} = \pi/2\}]$ . The CI is surrounded by loop  $L_1$  which is drawn in red lines (panel a). It consists of three parts, as indicated by small arrows: a "torsional" line along the torsional angle  $\phi$ , from  $\phi = \phi_2$  to  $\pi - \phi_2$  (panel a) and two "radial" lines with opposite directions along the radial coordinate  $r$ , from 0 to  $r_1$  and from  $r_1$  to 0, respectively. The values of the contour integral (4.28) for this loop is assumed to be  $\pi$ ; the + sign is used as "charge"  $e_1^{i,i+1} = 1$  for this CI. The symmetry properties of the NACTs are derived from their values at symmetry-related locations on the loop, which are indicated by asterisks (\*) on the torsional line and by plus (+) on radial lines. Bold arrows point to these symbols \* and +, indicating their symmetry-related values of the coordinates. The IREPs of the NACTs and CIs imply the existence of the additional symmetry-related  $CI_2^{i,i+1}$  which has opposite charge,  $e_2^{i,i+1}$ . This is surrounded by equivalent loop  $L_2$  (blue lines) with additional symmetry-related positions which are labeled again by symbols \* and +, respectively. The NACTs at these locations \* and + on blue lines  $L_2$  have the same absolute values as for the red line loop  $L_1$  but opposite sign. Panel b shows loop  $L_3$  which does not encircle the CI; It consists of three parts, i.e. a quarter circle along the torsional angle  $\phi$  which approaches the CI, plus two lines along  $x$  and  $y$  axes. The contour integrals (4.32) for these loop  $L_3$  are zero.

The only possible combinations of IREPs of the NACTs left are the first or the third one, see Table 3.3. Subsequently, the pole property (4.24) is applied in order to eliminate one of the two remaining possibilities, thus determining the one and only one combination of the IREPs of the NACTs which is left after elimination of the other choices. In order to exploit the pole property (4.24) close to  $CI^{i,i+1}$ , loop  $L_3$  is constructed, see Fig. 4.10(b).

The loop  $L_3$  consists of a quarter circle (quc) and two lines along the y and x axes. The radius  $r'$  of the quarter circle is chosen such that the loop does not encircle the CI, but it approaches the CI for  $\phi \rightarrow \pi/2$ , implying ever increasing absolute values of the  $\tau_\phi^{i,i+1}(r', \phi)$ , see rule (4.24). According to Eq.(4.23), the contour integral of the loop  $L_3$  should be equal to zero. To investigate this criteria, the contour integral is separated into three line integrals, specifically for the quarter circle (quc) plus the contributions on the y and x axes,

$$\oint d\vec{s} \cdot \tau^{i,i+1}(\vec{s}|L_3) = I_{quc} + I_y + I_x = 0, \quad (4.32)$$

where

$$I_{quc} = \int_0^{\pi/2} d\phi \tau_\phi^{i,i+1}(r', \phi|L_3), \quad (4.33)$$

$$I_y = \int_{r'}^0 dy \tau_y^{i,i+1}(x=0, y|L_3), \quad (4.34)$$

$$I_x = \int_0^{r'} dx \tau_x^{i,i+1}(x, y=0|L_3). \quad (4.35)$$

Now, for the first possible combination of IREPs of the NACTs, on one hand,  $\tau_x$  and  $\tau_y$  have nodes along the x and y axes, respectively, hence  $I_x = I_y = 0$ , see Table 3.3. On the other hand, the rule (4.24) implies that  $I_{quc} \neq 0$  because it is dominated by the large contributions of  $\tau_\phi^{i,i+1}(r', \phi|L_3)$  close to  $\phi = \pi/2$ . The net results is thus  $I_{quc} + I_x + I_y \neq 0$ , which is incompatible with Eq.(4.32).

In conclusion, for the case where the conical intersection  $CI_1^{i,i+1}$  is discovered at  $\phi^{i,i+1} = \pi/2$ , one can apply the quantization rule of the NACTs, Eq. (4.22), together with the pole property of the NACTs close to the CI, Eq.(4.24). This will eliminate all possible combination of the IREPs of the NACTs, except the third one. The third one shows that  $\Gamma(\tau_x^{i,i+1}(\vec{s})) = A_1$ ,  $\Gamma(\tau_y^{i,i+1}(\vec{s})) = A_2$ ,  $\Gamma(\tau_\phi^{i,i+1}(\vec{s})) = B_1$ , and  $\Gamma(\tau_r^{i,i+1}(\vec{s})) = B_2$ , see Table 3.3. It is equivalent to say that the two properties (4.22) and (4.24) of  $CI_1^{i,i+1}$ , together with the theorem (4.10), determine the IREPs  $\Gamma(\tau_k^{i,i+1}(\vec{s}))$  of all the NACTs, and this is equivalent to determining two non-trivial

characters  $\chi_{g,h}$  for each of them.

- 2- **The second case:** The conical intersection  $CI_1^{i,i+1}$  is located at the symmetry-adapted coordinate  $\phi^{i,i+1}=0$ , see Fig. 4.11(a). Arguments which are entirely analogous to those which have just been applied to  $CI^{i,i+1}(\{r^{i,i+1}, \phi^{i,i+1} = \pi/2\}_1)$  will be used to find the possible combination of the IREPs of the NACTs. The loop  $L'_1$  encloses one conical intersection, this implies that the contour integral is equal to  $e_1^{i,i+1}\pi$ . Like for first case, choosing positive sign, i.e.  $e_1^{i,i+1} = 1$ , implies that the contour integral is equal to  $\pi$ . The contour integral of loop  $L'_1$  is separated into three parts, i.e.

$$\oint d\vec{s} \cdot \tau^{i,i+1}(\vec{s}|L'_1) = I_{tor} + I_{rad,1} + I_{rad,2} = e_1^{i,i+1}\pi, \quad (4.36)$$

where

$$I_{tor} = \int_{-\phi_2}^{+\phi_2} d\phi \tau_{\phi}^{i,i+1}(r_1, \phi|L'_1), \quad (4.37)$$

$$I_{rad,1} = \int_0^{r_1} dr \tau_r^{i,i+1}(r, -\phi_2|L'_1), \quad (4.38)$$

$$I_{rad,2} = \int_{r_1}^0 dr \tau_r^{i,i+1}(r, \phi_2|L'_1). \quad (4.39)$$

The 2nd and 3rd combination show that the  $\tau_{\phi}^{i,i+1}(r_1, \phi)$  has alternative sign at the positions marked by \* in  $L'_1$ . This implies that  $I_{tor} = 0$ , see Table 3.3. Also the NACTs  $\tau_r^{i,i+1}(r_2, \phi_2 | L'_1)$  and  $\tau_r^{i,i+1}(r_2, \pi - \phi_2 | L'_1)$  which contribute to the radial integrals (4.38) and (4.39), respectively, are identical, hence  $I_{rad,1} + I_{rad,1} = 0$ . As consequence, the 2nd and 3rd combinations of IREPs would yield  $I_{rad,1} + I_{rad,1} + I_{tor} = 0$ . But this is in contradiction with the quantization rule.

Moreover, applying the pole property (4.24) of the NACTs close to  $CI_1^{i,i+1}$  applied to the contour integral for the loop  $L'_3$  shown in Fig. 4.11(b) eliminates the first combination, as follows. Since the loop  $L'_3$  consists of three segments: the quarter circle along the torsional angle  $\phi$  which approaches the CIs located at  $\phi^{i,i+1}=0$ , plus two lines along the  $x$  and  $y$  axes, the quantization rule (4.22) require that the contour integral should obey

$$\oint d\vec{s} \cdot \tau^{i,i+1}(\vec{s}|L'_3) = I_{quc} + I_x + I_y = 0, \quad (4.40)$$

where

$$I_{quc} = \int_{-\frac{\pi}{2}}^0 d\phi \tau_{\phi}^{i,i+1}(r', \phi | L'_3), \quad (4.41)$$

$$I_y = \int_0^{r'} dy \tau_y^{i,i+1}(x=0, y | L'_3), \quad (4.42)$$

$$I_x = \int_{r'}^0 dx \tau_x^{i,i+1}(x, y=0 | L'_3). \quad (4.43)$$

Table 3.3 shows that for the first possible combination of the IREPs, the NACTs  $\tau_x$  and  $\tau_y$  have nodes along x and y axes, respectively, this implies that  $I_x = I_y = 0$ , while, rule (4.24) implies that  $I_{quc} \neq 0$  since its dominated by the large contribution of  $\tau_{\phi}^{i,i+1}(r', \phi | L'_3)$  close to  $\phi = 0$ . As a consequence, Eq.(4.40) does not equal zero, contradiction to the rule (4.24).

In conclusion, if the conical intersection  $CI_1^{i,i+1}$  is discovered at  $\phi^{i,i+1} = 0$ , then the quantization rule will eliminate the second and third combination of the IREPs of the NACTs, whereas the rule (4.24) for the pole property of the NACTs close to  $CI_1^{i,i+1}$  eliminates the first combination. The only possible combination is the fourth one, thus,  $\Gamma(\tau_x^{i,i+1}(\vec{s})) = A_2$ ,  $\Gamma(\tau_y^{i,i+1}(\vec{s})) = A_1$ ,  $\Gamma(\tau_{\phi}^{i,i+1}(\vec{s})) = B_2$ , and  $\Gamma(\tau_r^{i,i+1}(\vec{s})) = B_1$ , see Table 3.3.

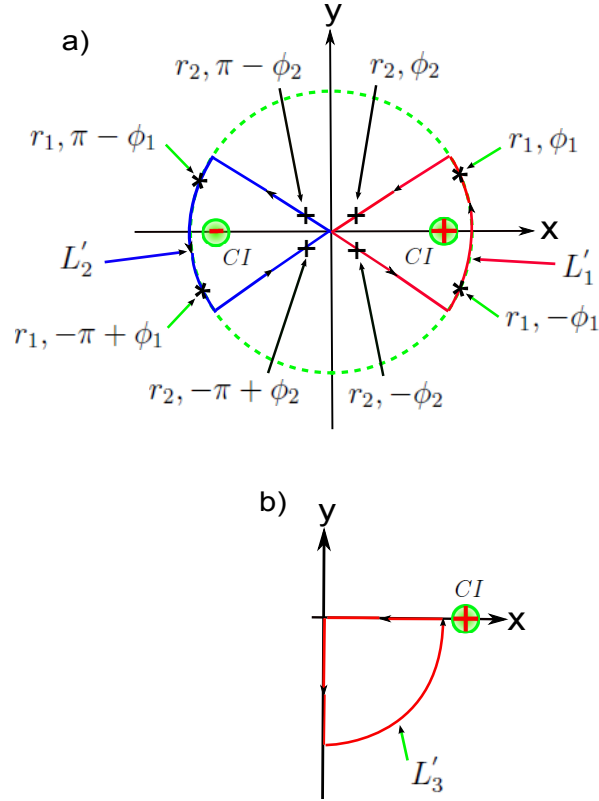


Figure 4.11.: Assigning the IREPs of the NACTs  $\tau_k^{i,i+1}(\vec{s})$  and the corresponding IREPs of the seams of the CIs. In this case the  $CI_1^{i,i+1}$  has been discovered at the symmetry-adapted coordinates  $[\vec{s}^{i,i+1}]_1 = [\{r^{i,i+1}, \phi^{i,i+1} = 0\}]$ . The CI is surrounded by loop  $L'_1$  which is drawn in red lines (panel a). It consists of three parts, as indicated by small arrows: a "torsional" line along the torsional angle  $\phi$ , from  $\phi = \phi_2$  to  $-\phi_2$  (panel a) and two "radial" lines with opposite directions along the radial coordinate  $r$ , from 0 to  $r_1$  and from  $r_1$  to 0, respectively. The values of the contour integral (4.28) for this loop is assumed to be  $\pi$ ; the + sign is used as "charge"  $e_1^{i,i+1} = 1$  for this CI. The symmetry properties of the NACTs are derived from their values at symmetry-related locations on the loop, which are indicated by asterisks (\*) on the torsional line and by plus (+) on radial lines. Bold arrows point to these symbols \* and +, indicating their symmetry-related values of the coordinates. The IREPs of the NACTs and CIs imply the existence of the additional symmetry-related  $CI_2^{i,i+1}$  which has opposite charge,  $e_2^{i,i+1}$ . The  $CI_2^{i,i+1}$  is surrounded by equivalent loop  $L'_2$  (blue lines) with additional symmetry-related positions which are labeled again by symbols \* and +, respectively. The NACTs at these locations \* and + on blue lines  $L'_2$  have the same absolute values as for the red line loop  $L'_1$  but opposite sign. Panel b shows loop  $L'_3$  which does not encircle the CI; It consists of three parts, i.e. a quarter circle along the torsional angle  $\phi$  which approaches the CI, plus two lines along  $x$  and  $y$  axes.

### 4.5.2. Calculating the NACTs of C<sub>5</sub>H<sub>4</sub>NH

The two symmetry-adapted coordinates  $(r, \phi)$  used to generate the PESs of C<sub>5</sub>H<sub>4</sub>NH are also used to calculate the related non-adiabatic coupling terms. The NACTs corresponding to these two coordinates are

$$\tau_{\phi}^{i,j}(r, \phi) = \langle \psi_{\text{el}}^i(r, \phi) | \frac{\partial}{\partial \phi} \psi_{\text{el}}^j(r, \phi) \rangle \quad (4.44)$$

and

$$\tau_r^{i,j}(r, \phi) = \langle \psi_{\text{el}}^i(r, \phi) | \frac{\partial}{\partial r} \psi_{\text{el}}^j(r, \phi) \rangle \quad (4.45)$$

In practice, NACTs are calculated by means of finite differences with help of the quantum chemistry MOLPRO program [32]; specifically we employ the approximations

$$\tau_{\phi}^{i,j}(r, \phi) \approx \frac{1}{2\Delta\phi} \left[ \langle \psi_{\text{el}}^i(r, \phi) | \psi_{\text{el}}^j(r, \phi + \Delta\phi) \rangle - \langle \psi_{\text{el}}^i(r, \phi) | \psi_{\text{el}}^j(r, \phi - \Delta\phi) \rangle \right] \quad (4.46)$$

and

$$\tau_r^{i,j}(r, \phi) \approx \frac{1}{2\Delta r} \left[ \langle \psi_{\text{el}}^i(r, \phi) | \psi_{\text{el}}^j(r + \Delta r, \phi) \rangle - \langle \psi_{\text{el}}^i(r, \phi) | \psi_{\text{el}}^j(r - \Delta r, \phi) \rangle \right]. \quad (4.47)$$

These approximations are valid to third orders of the parameters  $\Delta r$  and  $\Delta\phi$  for the finite differences. The choice of the parameters is made by considering two opposite requirements:

- 1- According to the numerical convergence request, the values of  $\Delta r$  and  $\Delta\phi$  must be very small and must be smaller than the width of any sharp peak which appear in the NACTs, specially, near the degeneracy points (CIs).
- 2- The chosen parameters should not be smaller than the limits which are imposed by the sensitivity of the quantum chemistry calculation of the electronic wavefunction with respect to very small shifts of the nuclear position.

According to these opposite requirements, the values of the parameters employed in our calculation are  $\Delta r = 0.0189 \text{ \AA}$  and  $\Delta\phi = 1.74 \times 10^{-4}$  radians ( $= 0.01^\circ$ ).

The quantum chemistry results for the torsional NACTs  $\tau_{\phi}^{i,j}(r, \phi)$  for  $r \approx 1.0 \text{ \AA}$  in the domain  $0 \leq \phi \leq \pi/2$  are shown in Fig. 4.12(b,e), see also Fig. 4.9. The results show large peaks of  $\tau_{\phi}^{i,j}$  near the degeneracy points. The quantum chemistry result of the corresponding PESs at  $r \approx 1.0 \text{ \AA}$  shows two degenerate points,  $CI_1^{0,1}$  at  $\phi = \pi/2$  and



$CI_1^{1,2}$  at  $\phi = 36^\circ$ , respectively, see Fig. 4.5. Figure 4.12(e) shows corresponding large peaks of the NACTs  $\tau_\phi^{0,1}$  and  $\tau_\phi^{1,2}$  close to the  $CI_1^{0,1}$  and  $CI_1^{1,2}$ , respectively, with rapid decay as one moves away from the CIs. This is due to the poles of the NACTs at the degeneracy points (CIs), see Section 4.5.1.

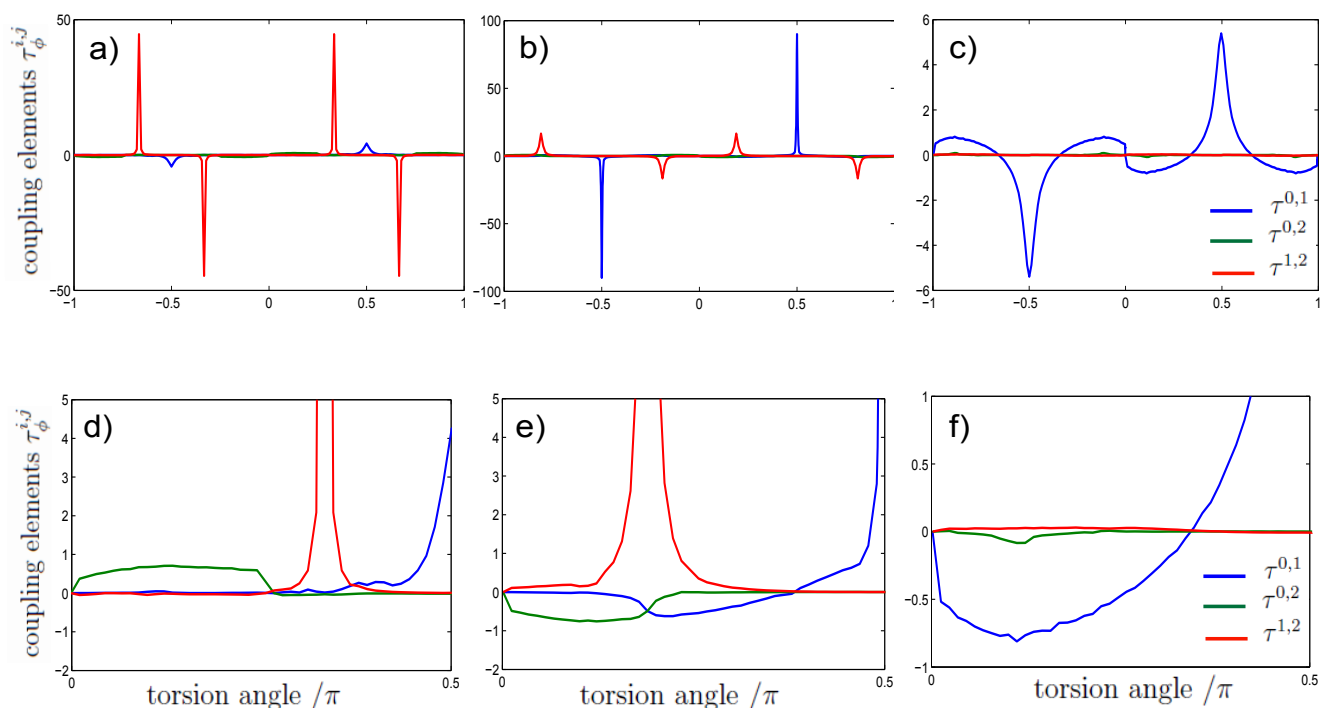


Figure 4.12.: The quantum chemistry calculated torsional non-adiabatic terms (NACTs)  $\tau_\phi^{0,1}$  ( blue lines),  $\tau_\phi^{0,2}$  ( green lines) and  $\tau_\phi^{1,2}$  ( red lines) in domain  $-\pi \leq \phi \leq +\pi$  (panels a-c) and  $0 \leq \phi \leq \pi/2$  (panels d-e) for  $r \approx 0.8 \text{ \AA}$  (panels a,d),  $r \approx 1.00 \text{ \AA}$  (panels b,e) and  $r \approx 1.2 \text{ \AA}$  (panels c,f), in unit of 1/radians. Note the different scale i.e. on one hand, the "blow up" panels d-f discover details such as the crossing of  $\tau_\phi^{0,1}$  and  $\tau_\phi^{0,2}$  which cannot be resolved in panels a-c. On the other hand, the "global" panels a-c demonstrate the patterns of the sign of the peaks of the NACTs, in accord with their irreducible representation in the frame of the "global" molecular symmetry group  $C_{2v}(M)$

Figure 4.12(a,d) shows the quantum chemistry results for the torsional NACTs  $\tau_\phi^{i,j}(r, \phi)$

for  $r \approx 0.8 \text{ \AA}$  in the domain  $0 \leq \phi \leq \pi/2$ . The results shows large peaks of NACTs  $\tau_\phi^{i,j}$  near the degeneracy points. The quantum chemistry result of the PESs for  $r \approx 0.8 \text{ \AA}$  shows two degenerate points  $CI_1^{0,1}$  and  $CI_1^{1,2}$  at  $\phi = \pi/2$  and  $\phi = 60^\circ$ , respectively, see Fig. 4.4. Fig. 4.12(a) shows corresponding large peaks of the NACTs  $\tau_\phi^{0,1}$  and  $\tau_\phi^{1,2}$  close to the  $CI_1^{0,1}$  and  $CI_1^{1,2}$ , respectively. For  $r \approx 1.2 \text{ \AA}$  the PES (Fig. 4.6) show avoided crossing. As a consequence, the values of the NACTs in Fig. 4.12(f) are much smaller than for the previous cases.

The challenge now is to define the sign of the peaks of the NACTs which appear in Fig. 4.12. The overall sign of these peaks close to the CIs ( $CI_1^{0,1}$  and  $CI_1^{1,2}$ ) are arbitrary, because the signs of the underlying electronic wave functions  $\psi_{el}^j(\vec{s}_e, \{r, \phi\})$ ,  $j = 0, 1, 2$  are arbitrary. As a convention, it is assumed that the NACTs close to the "first" CIs - that means for the first peak with  $\phi > 0$  - have positive signs, Fig. 4.12(d,e,f). In contrast, there is no near degeneracy between  $V_0$  and  $V_2$  in the restricted domain  $\{r \approx 1.0 \text{ \AA}, 0 \leq \phi \leq \pi/2\}$  - the maximum absolute value of the corresponding  $\tau_\phi^{0,2}$  is, therefore, much smaller than the peak values of  $\tau_\phi^{0,1}$  or  $\tau_\phi^{1,2}$ . Thus the signs of the  $\tau_\phi^{0,2}$  are no longer arbitrary, they depend on the given assignments for  $\tau_\phi^{0,1}$  and  $\tau_\phi^{1,2}$  because all the torsional  $\tau_\phi^{i,j}$  involve the same electronic wavefunctions labelled  $i = 0, 1$  and  $j = 1, 2$  ( $i < j$ ). As a consequence,  $\tau_\phi^{0,2}$  is negative in the domain close to  $CI_1^{1,2}$  such that the values of  $\tau_\phi^{0,2}$  and  $\tau_\phi^{0,1}$  interchange close to  $CI_1^{1,2}$ , see Fig. 4.12(e). This points to a switch of the characters of the electronic wavefunctions  $\psi_{el}^1(\vec{s}_e, \{r \approx 1.0 \text{ \AA}, \phi\})$  and  $\psi_{el}^2(\vec{s}_e, \{r \approx 1.0 \text{ \AA}, \phi\})$  close to  $CI_1^{1,2}$ .

For the other rings  $r \approx 0.8$  and  $1.2 \text{ \AA}$ , the signs of the "first" peaks of the NACTs  $\tau_\phi^{0,1}$  and  $\tau_\phi^{1,2}$  are also set to be positive, as for  $r \approx 1.0 \text{ \AA}$ , compare Fig. 4.12(d) and Fig. 4.12(f) with Fig. 4.12(e), respectively. The consistency of this assignment will be discussed in Section 4.5.3. Thus for  $r \approx 0.8 \text{ \AA}$ , Fig. 4.12(d) shows a large positive peak of  $\tau_\phi^{1,2}$  close to the  $CI_1^{1,2}$  which has been deduced from the near degeneracy of  $V_1$  and  $V_2$  close to  $\phi = 1.047$  radian ( $60^\circ$ ), see Fig. 4.4. In contrast, the increase of the energy gap between  $V_1$  and  $V_0$  causes strong decreases of the corresponding peak value of  $\tau_\phi^{0,1}$ , compare Fig. 4.12(d) with Fig. 4.12(e). This extrapolates a general trend from near degeneracies to avoided crossings with increasing energy gaps between 1d cuts of the PESs. These signatures of the CIs are located at increasing distances from the corresponding CIs, causing systematic decreases of the peak values of the corresponding NACTs, in accord with the pole property Eq. (4.24). This conjecture is confirmed by the results shown in Fig. 4.6 and Fig. 4.12(c) for  $r \approx 1.2 \text{ \AA}$ . The previous near degeneracies (Fig. 4.5 for  $r \approx 1.0 \text{ \AA}$ ) are transformed into avoided crossings, not only for  $V_0$  and  $V_1$  but even more drastically for  $V_1$  and  $V_2$ . Figure 4.12(f) shows that, indeed, the peak value of  $\tau_\phi^{0,1}$  at  $\{r \approx 1.2 \text{ \AA}, \phi = \pi/2\}$  is much smaller than at  $\{r \approx 1.0 \text{ \AA}, \phi = \pi/2\}$  which is shown in Fig. 4.12(e). Moreover, the peak for  $\tau_\phi^{1,2}$

which is so obvious in Fig. 4.12(d) and (e) has decayed to a marginal maximum value which is hardly noticeable in Fig. 4.12(f).

In the region close to the boundaries  $\phi = 0$  and  $\pi/2$ , see Fig. 4.12(d-f), some of the  $\tau_\phi^{i,j}$  have decayed to very small values, below the accuracy of the quantum chemistry based method for calculating the NACTs. In these cases, quantum chemistry *per se* is not sufficient to determine the signs of the NACTs in these neighbourhoods and, therefore, also not in other connected domains. The solution of this apparent quantum chemistry ambiguity will be presented in the next section.

### 4.5.3. Assignment of the IREPs of NACTs of $C_5H_4NH$

It is now straightforward to solve the combined task of the assignment of the IREPs of the NACTs of  $C_5H_4NH$  together with their nodal patterns. This will be done based on the general theorems and properties which have been derived and summarized in previous sections, in the frame of the molecular symmetry group  $C_{2v}(M)$ . Recall the quantization rule (4.22) and the pole property Eq. (4.24), applied for the model of two-state systems [3]. The exclusive peaks of the NACTs  $\tau_\phi^{0,1}(\{r \approx 1.0 \text{ \AA}, \phi\})$  and  $\tau_\phi^{1,2}(\{r \approx 1.0 \text{ \AA}, \phi\})$  in narrow domains close to the  $CI_1^{0,1}$  and  $CI_1^{1,2}$  demonstrate the approximate validity of the two-state scenario. This implies that there are apparently no other CIs which interfere with  $CI_1^{0,1}$  or  $CI_1^{1,2}$  close to  $\{\{r^{0,1}, \phi^{0,1}\}\}_1$  and  $\{\{r^{1,2}, \phi^{1,2}\}\}_1$ , respectively, see Fig. 4.12(b). The example for  $r \approx 1.0 \text{ \AA}$  is sufficient for the derivation of the IREPs of the NACTs, because these are global properties of the MS group  $C_{2v}(M)$  of  $C_5H_4NH$ . Once they are determined for the special case  $r \approx 1.0 \text{ \AA}$ , they apply automatically also to other values the MS adapted coordinates.

Let us start from the discovery of the  $CI_1^{0,1}$  based on the LH theorem ( $= S_0/S_1$  CI ( $1A'/1A''$ )) at  $\phi^{0,1} = \pi/2$ . This location implies immediately that  $\Gamma(\tau_\phi^{0,1}) = B_1$ . Recall that the derivation of this result exploits the quantization rule (4.22) and the pole property (4.24), in the frame of the two-state model which is approximately valid as discussed above. Moreover, the general theorem (4.14) immediately relates the IREP  $B_1$  of  $\tau_\phi^{0,1}$  to the IREPs of all the other NACTs  $\tau_k^{0,1}$ , for the same states  $i, i+1 = 0, 1$ . Specifically, the radial NACT has  $\Gamma(\tau_r^{0,1}) = B_2$ , whereas the Cartesian ones Eq.(4.6) have  $\Gamma(\tau_x^{0,1}) = A_1$  and  $\Gamma(\tau_y^{0,1}) = A_2$ . Symmetry Table 3.3 also lists the corresponding sign patterns for the peaks of the NACTs, as well as their nodal patterns. As an example,  $\tau_\phi^{0,1}(\{r, \phi\})$  should have opposite signs of the peaks for  $\phi = \pi/2$  and  $-\pi/2$ , and corresponding nodes at  $\phi = 0$  and  $\pm\pi$ .

Next recall that the NACTs  $\tau_\phi^{0,1}(r \approx 1.0 \text{ \AA}, \phi)$  and  $\tau_\phi^{0,2}(r \approx 1.0 \text{ \AA}, \phi)$  interchange close to the  $CI_1^{1,2}$  which is located at  $\{\{r \approx 1.0 \text{ \AA}, \phi \approx 0.628 (36^\circ)\}\}_1$ , see Fig. 4.12(e). The

general properties of the NACTs then imply that the IREPs of  $\tau_\phi^{0,1}$  and  $\tau_\phi^{0,2}$  are the same, as shown in Eq.(4.26) and (4.27), i.e.  $\Gamma(\tau_\phi^{0,2}) = \Gamma(\tau_\phi^{0,1}) = B_1$ . Likewise, for each pair of the NACTs  $\tau_k^{0,2}$  and  $\tau_k^{0,1}$  with respect to the other MS-adapted coordinates  $s_k = r, \phi$  or  $x, y$ , the IREPs are also the same, see theorem (4.14). As a consequence, the pairs of NACTs  $\tau_k^{0,2}$  and  $\tau_k^{0,1}$  have the same nodal patterns - for example,  $\tau_\phi^{0,2}$  should have nodes at  $\phi = 0$  and at  $\phi = \pm\pi$ , same as for  $\tau_\phi^{0,1}$ , *vide infra*.

Finally, the general theorem (4.17) which includes the special case (4.19) is used to determine the IREP of the NACT which is still "missing",  $\tau_\phi^{1,2}$ . Theorem (4.19) implies that  $\Gamma(\tau_\phi^{1,2}) = A_2$ . Using this as a reference, the IREPs of the  $\tau_k^{1,2}$  for the other MS-adapted coordinates  $s_k$  are determined, again using theorem (4.14). The results for the IREPs, the sign patterns of the peaks, and the nodal patterns for all the NACTs  $\tau_k^{i,j}$ , with respect to all coordinates  $k = r, \phi, x$  and  $y$  and for the three lowest electronic singlet states  $i=0,1,2$  are listed in Table 3.3. For example,  $\tau_\phi^{1,2}$  should have nodes not only at  $\phi = 0$  and  $\phi = \pm\pi$ , but also at  $\phi = \pm\pi/2$ . It is impossible to deduce all these nodal patterns, which are a property of the molecular symmetry of C<sub>5</sub>H<sub>4</sub>NH, from the quantum chemistry results shown in Fig. 4.12(d-f). For example, the values of NACTs  $\tau_\phi^{0,1}(\{r \approx 1.0 \text{ \AA}, \phi\})$  close to  $\phi = \pi/2$ , far away from  $CI_1^{1,2}$ , are compatible with a node or with no node at  $\pi/2$ , since they are below the accuracy of the method for calculating the NACTs.

## 4.6. Adiabatic-to-diabatic Transformation (ADT)

The kinetic couplings, i.e. the NACTs, between separated adiabatic electronic states can be neglected while the energy gap between the electronic state is large. In contrast, near the degeneracy points (CIs) this energy gap become very small and the NACTs have poles, i.e. they approach infinity. The NACTs also have an important role for the photo-induced dynamics since they determine the efficiency of the ultrafast radiationless decay between different electronic states. The singularity of the NACTs at the CIs makes the simulation of nuclear dynamics on coupled electronic states very difficult in the adiabatic representation. In order to remove these singularities an adiabatic-to-diabatic transformation (ADT) is applied, as described in Section 2.5. The transformation matrix  $\mathbf{A}$  is given by Eq. (2.63). In the our model system, we consider just three states  $S_0$ ,  $S_1$  and  $S_2$ , the starting point is  $\phi_0 = -\pi$ , and the  $\mathbf{A}$ -matrix at  $\phi_0 = -\pi$  is defined as the unity matrix

$$\mathbf{A}(r, \phi_0) = \begin{pmatrix} 1 & 0 & 0 \\ 0 & 1 & 0 \\ 0 & 0 & 1 \end{pmatrix} \quad (4.48)$$

The integration along the loop  $L(r)$  with radius  $r$  from  $\phi_0$  to  $\phi_0 + 2\pi$ , yields the topological matrix  $\mathbf{D}(\mathbf{r})$  [3].

$$\mathbf{D}(r) = \mathbf{A}(r, 2\pi) = \wp \exp \left[ - \int_{\phi_0}^{\phi_0+2\pi} d\phi' \boldsymbol{\tau}_{\phi'}(r, \phi') \right] \mathbf{A}(r, \phi_0). \quad (4.49)$$

The numerical evaluation of Eq.(4.49) is described in Section 2.5.

The topology matrix  $\mathbf{D}(\mathbf{r})$  is diagonal if the three states form a quasi-Hilbert subspace in the region surrounded by  $L(r)$ . The  $\mathbf{D}(\mathbf{r})$  matrix is also orthogonal, hence the diagonal elements are equal to +1 or -1. Figure 4.13 shows the elements of the A-matrix of  $\text{C}_5\text{H}_4\text{NH}$  as a function of  $\phi$  for three different values of  $r$ , i.e.  $r \approx 0.8, 1.0$  and  $1.2 \text{ \AA}$ , based on the NACTs  $\tau_{\phi}^{i,j}$  shown in Fig. 4.12 in the domain  $-\pi \leq \phi \leq +\pi$ . In the limit  $\phi \rightarrow \pi$ , the ADT matrix approaches the topological matrix  $\mathbf{D}(\mathbf{r})$ . It is gratifying that the numerical values of  $\mathbf{D}(\mathbf{r})$  satisfy the quantization rule perfectly, i.e. it is a self-consistency test for the NACTs and their IREPs.

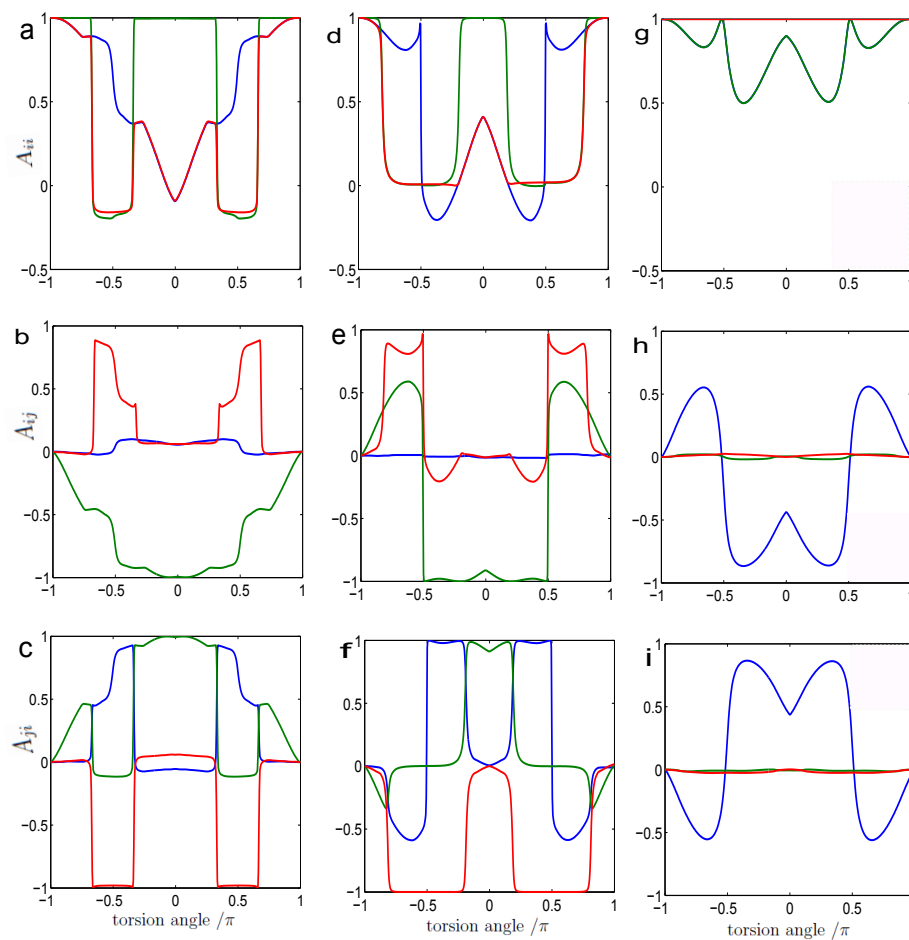


Figure 4.13.: Elements of the  $\mathbf{A}(r, \phi)$ -matrix as a function of  $\phi$  for  $r \approx 0.8 \text{ \AA}$  (panels a-c),  $r \approx 1.0 \text{ \AA}$  (panels d-f) and for  $r \approx 1.2 \text{ \AA}$  (panels g-i). Panels a, d and g show the diagonal elements  $A_{ii}$ , where  $A_{11}$  presented in blue lines, green lines show  $A_{22}$  and red lines for  $A_{33}$ . Panels b, e, h and c, f, i show the off-diagonal elements  $A_{ij}$  and  $A_{ji}$ , respectively. The values of  $A_{12}$  and  $A_{21}$  are indicated by blue lines,  $A_{13}$  and  $A_{31}$  in green lines, finally,  $A_{23}$  and  $A_{32}$  are shown in red lines.

Applying the transformation matrix  $\mathbf{A}$  to the diagonal matrix  $\mathbf{V}(r, \phi)$  for the adiabatic PESs yields the diabatic potential matrix  $\mathbf{W}$

$$\mathbf{A} \begin{pmatrix} V_2 & 0 & 0 \\ 0 & V_1 & 0 \\ 0 & 0 & V_0 \end{pmatrix} \mathbf{A}^\dagger = \begin{pmatrix} W_{22} & W_{21} & W_{20} \\ W_{12} & W_{11} & W_{10} \\ W_{02} & W_{01} & W_{00} \end{pmatrix} = \mathbf{W} \quad (4.50)$$

Here  $W_{01} = W_{10}$ ,  $W_{20} = W_{02}$  and  $W_{21} = W_{12}$ . The coupling elements between the states will appear in the form of potential coupling terms  $W_{01}$ ,  $W_{02}$  and  $W_{12}$ . The diabatic matrix elements are single-valued, i.e.  $\mathbf{W}(r, \phi) = \mathbf{W}(r, \phi + 2\pi)$ , which is the result of the quantization rule for the topological matrix. Figure 4.14, shows the three diabatic potentials  $W_{00}$ ,  $W_{11}$  and  $W_{22}$  for different values of  $r$ . Figure 4.14(a) shows the diabatic potentials for  $r \approx 0.8 \text{ \AA}$ , while the diabatic potentials for  $r \approx 1.0$  and  $1.2 \text{ \AA}$  are shown in Fig. 4.14(b) and (c), respectively. Note that the diabatic potentials do not transform according to IREPs of  $C_{2v}(M)$ , e.g.

$$|W_{ii}(r, \phi = 0)| \neq |W_{ii}(r, \phi = \pm\pi)|. \quad (4.51)$$

As it will be shown in next chapter, diabatic quantum dynamics simulation on those diabatic potentials lead nevertheless to consistent description of the adiabatic nuclear dynamics of the system.

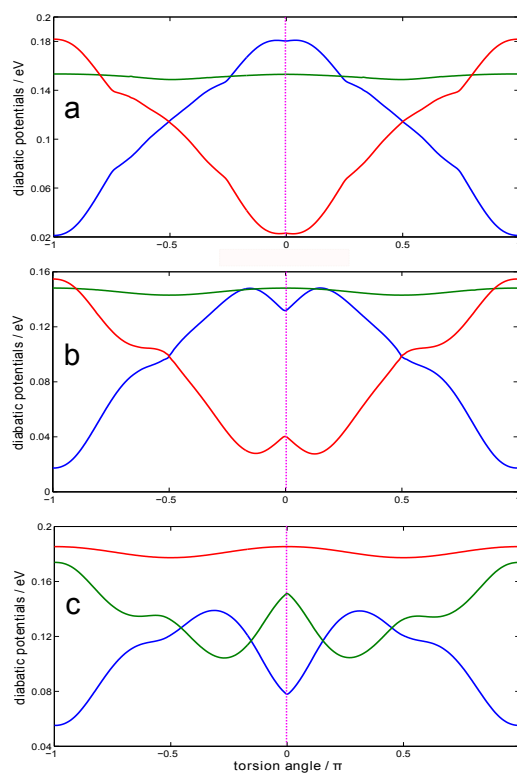


Figure 4.14.: The diatomic potential energy surfaces for three values of  $r$  - Panel a at symmetry adapted coordinates  $s = \{r \approx 0.8 \text{ \AA}, -\pi \leq \phi \leq +\pi\}$ , Panel b for  $s = \{r \approx 1.0 \text{ \AA}, -\pi \leq \phi \leq +\pi\}$ , Panel c for  $s = \{r \approx 1.2 \text{ \AA}, -\pi \leq \phi \leq +\pi\}$ , where blue lines indicates  $W_{11}$ , green lines  $W_{22}$  and blue lines  $W_{33}$ .



## 4.7. Conclusion

In this chapter we discover several properties related to the CIs and the related NACTs with respect to symmetry-adapted coordinates. One of these discoveries is to generate a complete set of conical intersections from the first localized  $CI_1^{i,i+1}$  between the PES at symmetry-adapted coordinates  $\vec{s} = \vec{s}_1^{i,i+1}$  by applying the symmetry operations  $\hat{S}_g$ ,  $g=1,2,\dots,G$  of the MS. This will yield a complete set of conical intersection  $CI_g^{i,i+1}$  at different symmetry-adapted location  $\vec{s}_g^{i,i+1} = \hat{S}_g \vec{s}_1^{i,i+1}$ .

The main investigation of this chapter is the determination the IREPs of the CIs and related NACTs. In order to do that, we derived the general theorems (4.14) and (4.17), together with known properties of the NACTs related to the CIs [3], in particular the quantization rule (4.22), pole properties (4.24) and switching property (4.26). These theorems allow to assign the IREPs of the NACTs and CIs, in the frame of the MS group. The discovering of IREPs provide several "global" properties, such as:

- 1- The pattern of the sign of the peaks value of the NACTs close to the set of MS-adapted CIs.
- 2- The nodal pattern of the NACTs

These properties cannot always be provided by means of quantum chemistry calculations, they are a result of combination between quantum chemistry and global MS group. For example, applying quantum chemistry will provide the same absolute values of the NACTs close to several symmetry-adapted potential minima. Applying MS group will provide the sign of the related NACTs.

These general theories and the resulting NACTs and CIs with the proper IREPs global domain have been demonstrated in detail for model system  $C_5H_4NH$  which has  $C_{2v}(M)$  molecular symmetry. This step-by-step approach could serve as an example for extended applications. The results are summarized in Table 3.3 as well as in several Figures. Some of the underlying tools which have been developed or integrated in the individual steps appear to be quite powerful. For example, the localization of the first  $CI_1^{0,1}$  at the perpendicular geometry ( $\phi^{0,1} = \pi/2$ ) has been achieved by means of the method based on the Longuet-Higgins theorem [17]. This requires nothing but quantum chemistry calculations of four anchors ( the potential minima and two transition states) of  $C_5H_4NH$  in the electronic ground state  $S_0$ . Nevertheless, this rather restricted input from quantum chemistry, combined with the general results for the MS group, suffices in order to determine the global IREPs of all the NACTs  $\tau_k^{0,1}$  for the couplings of the PES of the electronic ground state  $V_0$  and the excited state  $V_1$ , including all the MS properties such as the nodal patterns and the signs of the NACTs or the opposite charges of the MS-adapted set of the two  $CI_1^{0,1}$  and  $CI_2^{0,1}$ .

These and other, rather rich results for all the NACTs and the CIs of the three lowest electronic singlet states  $S_1, S_1$  and  $S_2$  of C<sub>5</sub>H<sub>4</sub>NH have been confirmed by various tests for self-consistency. In particular, we have calculated the A-matrices for adiabatic-to-diabatic transformation, based on the MS-adapted NACTs, along different paths for molecular torsion. In the limit of torsion by  $2\pi$  ( $360^\circ$ ), the A-matrices approach the so-called topological matrices D which have to satisfy simple but mandatory quantization rules, i.e. they must be diagonal, with diagonal elements equal to 1 or -1 where the number of -1's must be even [3]. We consider the successful computational tests of this demanding rule as rewarding. Turning the table, the self-consistency tests could also be employed as alternative criteria for the determination of the IREPs.

**5. Molecular Symmetry Effects and  
Non-adiabatic Nuclear Dynamics:  
Simulation of Photo-Induced Torsion  
of C<sub>5</sub>H<sub>4</sub>NH**

## 5.1. Introduction

In this chapter, we investigate the photo-induced cis-trans isomerization around the CN-bond in C<sub>5</sub>H<sub>4</sub>NH, i.e. the rotation of the H-atom around the CN-bond. The main goal of this chapter is to investigate the effects of the molecular symmetry of the CIs and the corresponding NACTs on the nuclear dynamics and to demonstrate the importance of the molecular symmetry of the NACTs in quantum dynamical simulations. To achieve this aim, the following steps are presented:

- Presentation of two cases with identical potentials and absolute values of the NACTs, but with different irreducible representation.
- Determination of the symmetry of the transition dipole moments.
- Simulation of the radiation-less decay after  $\delta$ -pulse excitation and discussion of symmetry effects.
- Simulation of photo-excitation with laser pulse of finite duration and dipole functions depending on the torsion angle, discussion of symmetry effect and comparison between dynamics in adiabatic and diabatic representation.

## 5.2. PES and the Related Non-adiabatic Coupling Terms of C<sub>5</sub>H<sub>4</sub>NH: Comparison between two cases

In order to investigate the symmetry effects on the nuclear dynamics, two cuts of the PESs are considered with the symmetry-adapted coordinates  $\vec{s} = \{r \approx 0.8 \text{ \AA}, \phi\}$  and  $\vec{s} = \{r \approx 1.0 \text{ \AA}, \phi\}$  as shown in Figs. 5.1 and 5.2. In Section 4.4, the IREPs of the corresponding NACTs have been determined. Here, for each cut of PES, a second case with same absolute values of the NACTs but with different IREPs is proposed. These examples with different IREPs of the NACTs will provide insight in the effect of MS on the quantum dynamics.

The PESs and the related NACTs for C<sub>5</sub>H<sub>4</sub>NH at symmetry-adapted coordinates  $r \approx 0.8 \text{ \AA}$  are presented in Section 4.4. The one-dimensional cut through the PESs belonging to three lowest electronic state  $S_0$  (blue line),  $S_1$  (green line) and  $S_2$  (red line) is shown again in Fig. 5.1(a) (thin lines) together with the related NACTs (broad lines). It is shown in Section 4.5 that the NACTs must fulfil certain rules which are related to the transformation of the Hamiltonian to the diabatic basis by the unitary matrix  $\mathbf{A}$ . Figure 5.1(b) shows that the diagonal elements of  $\mathbf{A}$ -matrix, i.e. the elements  $A_{ii}$ , fulfil the quantization condition of NACTs, i.e.  $\mathbf{A}(\phi = 0) = \mathbf{A}(\phi = 2\pi)$ . The corresponding diabatic potential  $W_{ii}$  are

shown again in Fig.5.1(c).

Moreover, it has been shown in Section 4.6 that the NACTs have to fulfil certain symmetry rules. In particular, the following equation for the irreducible representation  $\Gamma$  of the NACTs must hold (see Eq. (4.19))

$$\Gamma(\tau_\phi^{0,1}) \times \Gamma(\tau_\phi^{0,2}) \times \Gamma(\tau_\phi^{1,2}) = \Gamma\left(\frac{\partial}{\partial\phi}\right) = A_2 \quad (5.1)$$

As it can be seen in Fig.5.1(a),  $\Gamma(\tau_\phi^{0,1}) = B_1$  (broad blue line),  $\Gamma(\tau_\phi^{0,2}) = B_1$  (broad green line) and  $\Gamma(\tau_\phi^{1,2}) = A_2$  (broad red line) fulfil Eq. (5.1) with

$$B_1 \times B_1 \times A_2 = A_2 \quad (5.2)$$

In the following, the NACTs with this symmetry are referred to as "case I".

In order to investigate the effect of the symmetry of the NACTs on the radiation-less decay, another case with different symmetry of the NACTs is considered. Figure 5.1(a') shows again the terms  $\tau_\phi^{0,1}$  (broad blue line),  $\tau_\phi^{0,2}$  (broad green line) and  $\tau_\phi^{1,2}$  (broad red line). Here, the NACTs have the same absolute values but different relative sign, i.e. different IREPs compared to Fig.5.1(a). In this case (case II), the irreducible representation  $\Gamma$  of the NACTs also fulfill Eq.(5.1) with

$$\Gamma(\tau_\phi^{0,1}) \times \Gamma(\tau_\phi^{0,2}) \times \Gamma(\tau_\phi^{1,2}) = B_1 \times A_2 \times B_1 = A_2 \quad (5.3)$$

The corresponding diagonal elements of the  $\mathbf{A}$ -matrix, depicted in Fig.5.1(b'), show that the quantization rule  $\mathbf{A}(\phi = 0) = \mathbf{A}(\phi = 2\pi)$  is also fulfilled for case II. The diabatic potentials for case II are shown in Fig.5.1(c') where the elements  $W_{00}$ ,  $W_{11}$  and  $W_{22}$  presented in blue, green and red lines, respectively. The two diabatic potentials for case I and II are slightly different. The two cases I and II are the only possible combination of IREPs of the NACTs which fulfil the symmetry rules Eq.(4.14) and Eq.(4.17) and the quantization rule for the  $\mathbf{A}$ -matrix.

Note that case II does not fulfill condition (4.26) and has therefore been excluded in Section 4.5. Figure 5.2 shows again the PES, NACTs and  $\mathbf{A}$ -matrix for  $\vec{s} = \{r \approx 1.0 \text{ \AA}, \phi\}$ , which have been presented in Section (4.4). The IREPs of the NACTs, as in Fig.5.1(a), fulfil the symmetry rules Eq.(5.2).

The NACTs for this case (case I) are shown in Fig.5.2(a), where  $\tau_\phi^{0,1}$  is depicted as broad blue line,  $\tau_\phi^{0,2}$  as broad green line and  $\tau_\phi^{1,2}$  as broad red line. Again, we consider a second case with the following IREPs  $\Gamma(\tau_\phi^{0,1}) = B_1$ ,  $\Gamma(\tau_\phi^{0,2}) = A_2$  and  $\Gamma(\tau_\phi^{1,2}) = B_1$ , as it can be

seen in Fig.5.2(a'). Fig.5.2 panels (b) and (b') show diagonal term of the A-matrix, with the elements  $A_{00}$  (blue lines),  $A_{11}$  (green lines) and  $A_{22}$  (red lines). For both cases the quantization is fulfilled for  $i=0,1$  and  $2$  with  $A_{ii}(2\pi) = +1$ . The corresponding diabatic potentials  $W_{ii}$  for case I and II are shown in Fig.5.2(c) and (c'), respectively.

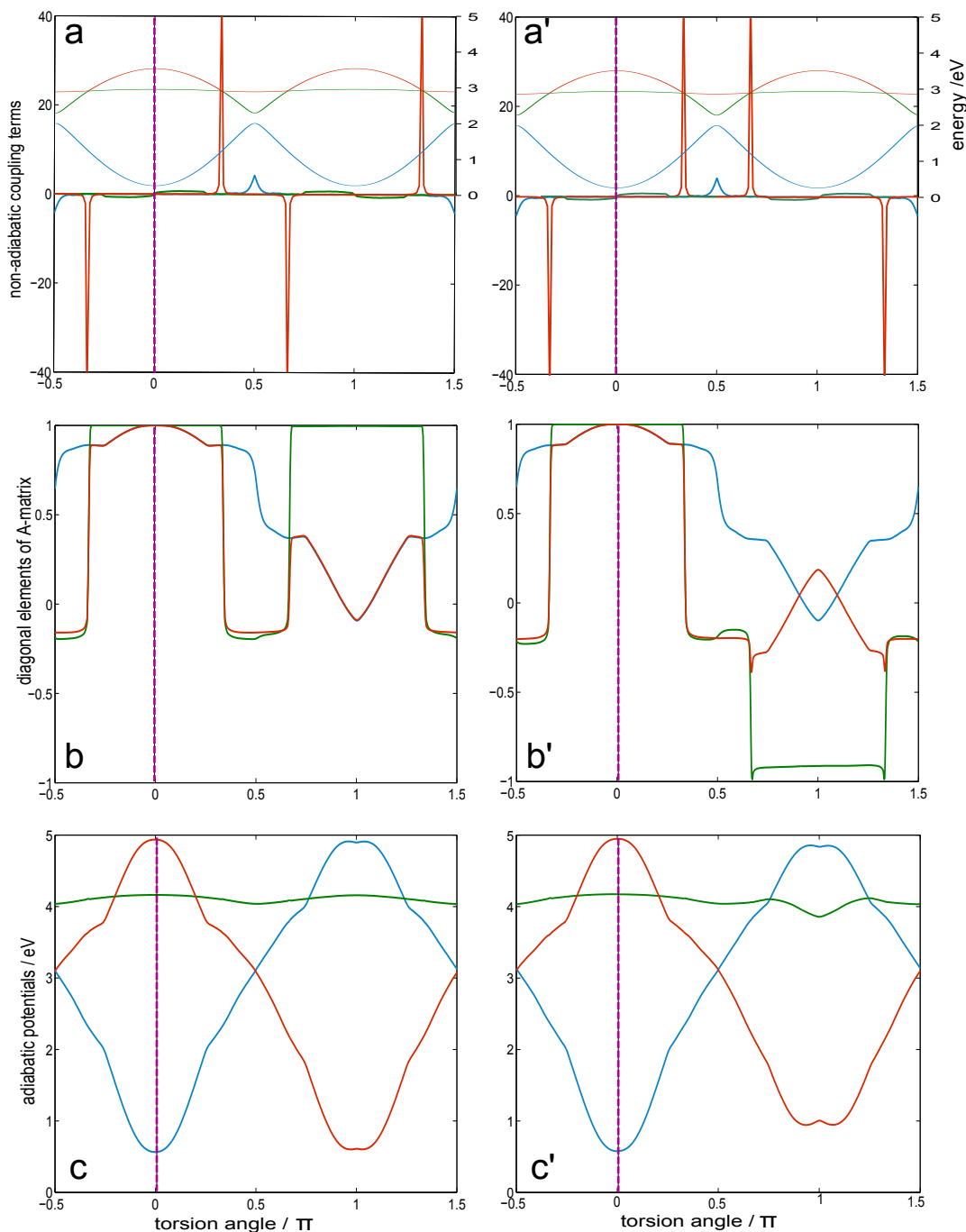


Figure 5.1.: The non-adiabatic coupling elements for the symmetry-adapted coordinates  $\vec{s} = \{r \approx 0.8 \text{ \AA}, \phi\}$  for case I (a) and case II (a'). The terms  $\tau_\phi^{0,1}$ ,  $\tau_\phi^{0,2}$  and  $\tau_\phi^{1,2}$  are depicted in blue, green and red broad lines, respectively. For comparison the adiabatic potentials are shown in thin lines. The diagonal elements of the A-matrix can be seen in panels (b) and (b') for case I and II, respectively. Here, the blue, green and red lines refer to  $A_{00}$ ,  $A_{11}$  and  $A_{22}$ . Finally, the panels (c) and (c') show the diabatic potentials  $W_{00}$  (blue lines),  $W_{11}$  (green lines) and  $W_{22}$  (red lines).

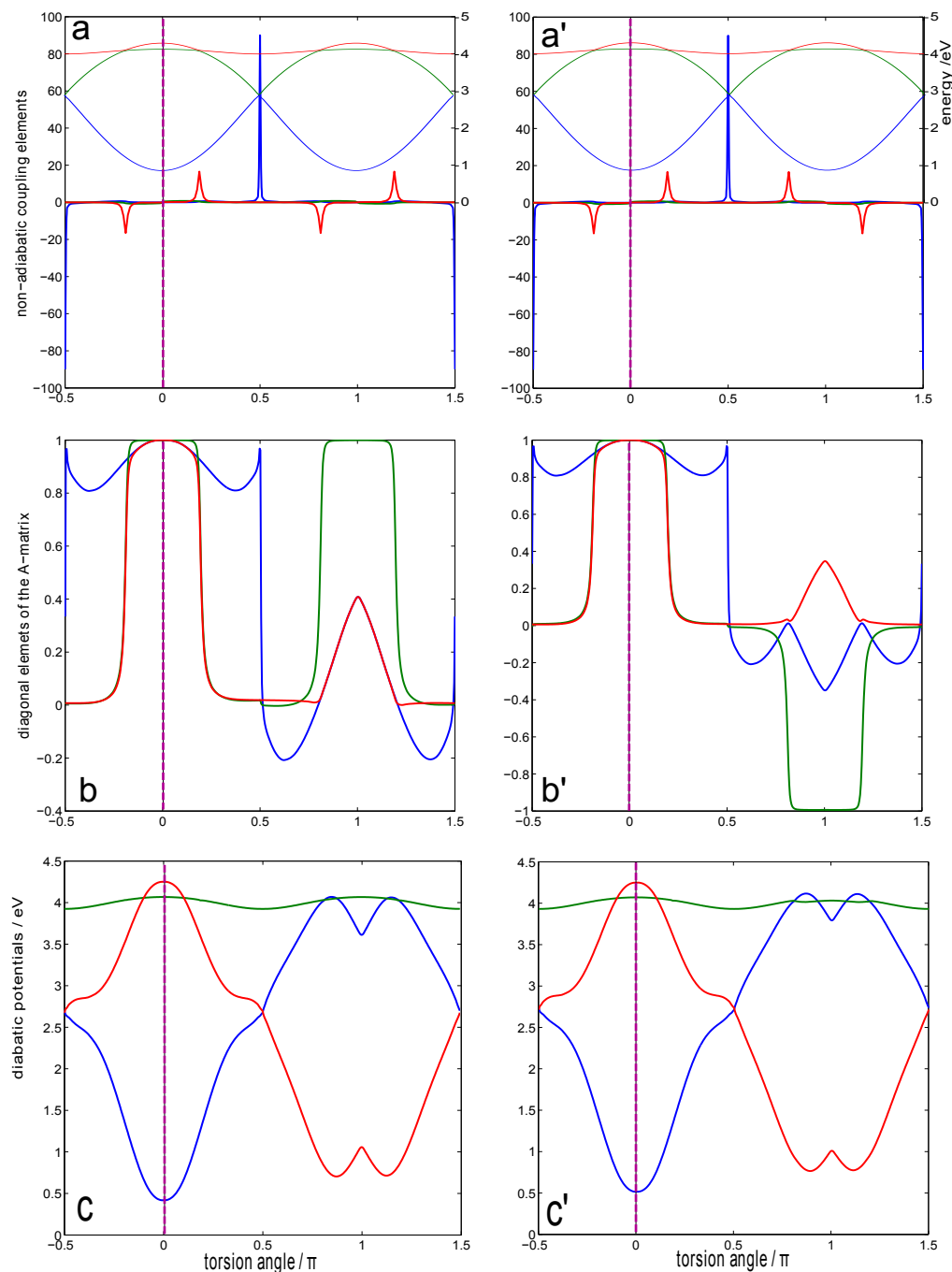


Figure 5.2.: The NACTs for the symmetry-adapted coordinates  $\vec{s} = \{r \approx 1.0 \text{ \AA}, \phi\}$  for case I (a) and case II (a'). The terms  $\tau_{\phi}^{0,1}$ ,  $\tau_{\phi}^{0,2}$  and  $\tau_{\phi}^{1,2}$  are depicted in blue, green and red broad lines, respectively. For comparison the adiabatic potentials are shown in thin lines. The diagonal elements of the A-matrix can be seen in panels (b) and (b') for case I and II, respectively. Here, the blue, green and red lines refer to  $A_{00}$ ,  $A_{11}$  and  $A_{22}$ , respectively. Finally, the panels (c) and (c') show the diabatic potentials  $W_{00}$  (blue lines),  $W_{11}$  (green lines) and  $W_{22}$  (red lines).



### 5.3. Assigning the IREPs of the Transition Dipole Moments

The transition dipole moments  $\mu_z^{i,j}$  also transform according to the irreducible representation of  $C_{2v}(\text{M})$ . In this section, we show how the IREPs of the NACTs determine the IREPs of the transition dipole moments. Since the transition dipole moments

$$\mu_z^{i,j} = \langle \psi_{\text{el}}^i(\phi) | \mu_z | \psi_{\text{el}}^j(\phi) \rangle \quad (5.4)$$

contains the electronic dipole operator, we first determine the transformation of the x, y and z components of the electronic coordinates in  $C_{2v}(\text{M})$

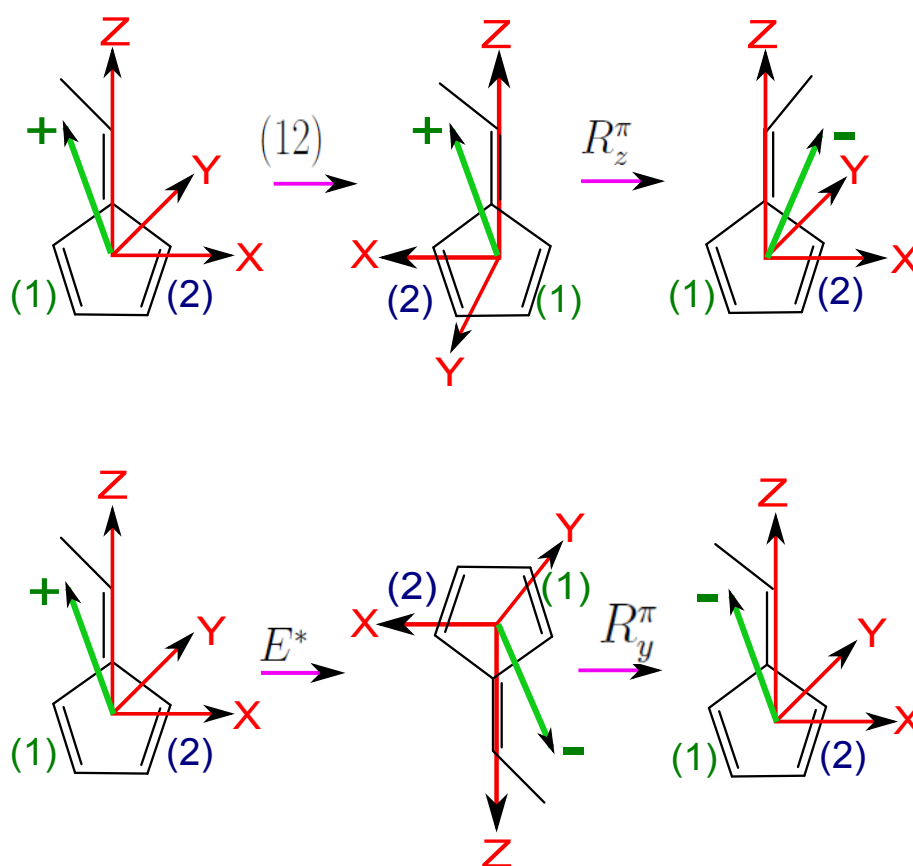


Figure 5.3.: The transformation of the electronic coordinates (depicted by the green arrow, where the + and - sign indicates the position of the arrow with respect to the XZ-plane) upon applying the symmetry operations of the group  $C_{2v}(\text{M})$ . Here,  $R_z^\pi$  and  $R_y^\pi$  denote the equivalent rotations [43], and X, Y and Z describe the molecular fixed coordinates system.

Figure 5.3 shows the effect of the symmetry operations (12) and  $E^*$ , on the electronic coordinates, depicted by the green arrow. Together with  $(12)^*=(12)E^*$ , these operations determine the IREPs for the electronic coordinates as follows (see character Table 4.3):

- 1- The x-components of the electronic coordinates transform as  $B_2$ , as a result of

$$\left. \begin{array}{l} Ex = +x \\ (12)x = -x \\ E^*x = +x \\ (12)^*x = -x \end{array} \right\} \implies x \sim B_2 \quad (5.5)$$

- 2- The y components transforms as  $B_1$ ,

$$\left. \begin{array}{l} Ey = +y \\ (12)y = -y \\ E^*y = -y \\ (12)^*y = +y \end{array} \right\} \implies y \sim B_1 \quad (5.6)$$

- 3- The z components transform as  $A_1$ , since

$$\left. \begin{array}{l} Ez = +z \\ (12)z = +z \\ E^*z = +z \\ (12)^*z = +z \end{array} \right\} \implies z \sim A_1 \quad (5.7)$$

Figure 5.3 and Eq.(5.7) imply that z-component of the dipole operator transforms as  $A_1$ , i.e.

$$\Gamma(\mu_z) = \Gamma(z) = A_1 \quad (5.8)$$

As a consequence the IREPs of the transition dipole moments can be determined from the symmetry of the NACTs as follows

$$\Gamma(\tau_\phi^{i,j}) \times \Gamma(\mu_z^{i,j}) = \Gamma\left(\frac{\partial}{\partial \phi}\right) \times \Gamma(z) = A_2 \quad (5.9)$$

or

$$\Gamma(\mu_z^{i,j}) = \Gamma(\tau_\phi^{i,j}) \times A_2 \quad (5.10)$$

for  $i \neq j$ .

Relations (5.10) is used to determine all components of the transition dipole moments for

case I as follows:

$$\begin{aligned}
 \Gamma(\mu_z^{0,1}) &= \Gamma(\tau_\phi^{0,1}) \times A_2 = B_1 \times A_2 = B_2 \\
 \Gamma(\mu_z^{0,2}) &= \Gamma(\tau_\phi^{0,2}) \times A_2 = B_1 \times A_2 = B_2 \\
 \Gamma(\mu_z^{1,2}) &= \Gamma(\tau_\phi^{1,2}) \times A_2 = A_2 \times A_2 = A_1
 \end{aligned}
 \tag{5.11}$$

Table 5.1 summarize the symmetry of the NACTs and transition dipole moments (case I). As explained in Section 5.2, we also consider a second case where the NACTs transform according to different IREP, which are also summarized in Table 5.1 (case II). As a consequence, also the transition dipole moments have different IREPs. According to Eq. (5.10),  $\mu_\phi^{0,1}$ ,  $\mu_\phi^{0,2}$  and  $\mu_\phi^{1,2}$  transform as  $B_2$ ,  $A_1$  and  $B_2$ , respectively (see Table 5.1). All dipole moments  $\mu_z^{i,i}$  transform as  $A_1$ .

	CASE I	CASE II
$\tau_\phi^{0,1}$	$B_1$	$B_1$
$\tau_\phi^{0,2}$	$B_1$	$A_2$
$\tau_\phi^{1,2}$	$A_2$	$B_1$
$\mu_\phi^{0,1}$	$B_2$	$B_2$
$\mu_\phi^{0,2}$	$B_2$	$A_1$
$\mu_\phi^{1,2}$	$A_1$	$B_2$

Table 5.1.: The IREPs of the NACTs and of the transition dipole moments  $\mu_z^{i,j}$  for cases I and II.

## 5.4. Photo-Excitation and Molecular Symmetry of the Initial Wavepacket

In order to investigate the movement of the H-atom, i.e. the torsion around CN axis after excitation with an ultra-short laser pulse, the time-dependent Schrödinger equation

$$i\hbar \frac{\partial}{\partial t} \vec{\psi}_{\text{nuc}}(\phi, t) = [\mathbf{H} + \mathbf{H}_{\text{int}}(t)] \vec{\psi}_{\text{nuc}}(\phi, t) \quad (5.12)$$

has to be solved, where

$$\vec{\psi}_{\text{nuc}}(\phi, t) = \begin{pmatrix} \psi_{\text{nuc}}^2(\phi, t) \\ \psi_{\text{nuc}}^1(\phi, t) \\ \psi_{\text{nuc}}^0(\phi, t) \end{pmatrix} \quad (5.13)$$

is the nuclear wavefunction in the adiabatic basis which depends on the torsion angle  $\phi$ . The molecular Hamiltonian  $\mathbf{H}$  is given by

$$\mathbf{H} = -\frac{\hbar^2}{2I_{\text{red}}} \left( \frac{\partial}{\partial \phi} + \boldsymbol{\tau}_{\phi} \right)^2 + \mathbf{V} \quad (5.14)$$

where  $I_{\text{red}}$  is the reduced moment of inertia,  $\mathbf{V}$  is the adiabatic potential matrix and the  $\boldsymbol{\tau}_{\phi}$  matrix contains the NACTs. Note that  $\boldsymbol{\tau}_{\phi} = \boldsymbol{\tau}_{\phi}^{(1)}$  where (1) is dropped for simplicity. Here, real electronic wavefunctions are considered, so the diagonal elements  $\tau_{\phi}^{i,i}$  are zero and the  $\boldsymbol{\tau}_{\phi}$ -matrix is anti-symmetric, i.e.

$$\boldsymbol{\tau}_{\phi} = \begin{pmatrix} 0 & \tau_{\phi}^{1,2} & \tau_{\phi}^{0,2} \\ -\tau_{\phi}^{1,2} & 0 & \tau_{\phi}^{0,1} \\ -\tau_{\phi}^{0,2} & -\tau_{\phi}^{0,1} & 0 \end{pmatrix} \quad (5.15)$$

The interaction of the molecule with a  $z$ -polarized laser pulse (see Fig.5.4) is described by

$$H_{\text{int}}(t) = -E(t)\boldsymbol{\mu}_z. \quad (5.16)$$

Here, we assume that the molecules are oriented along the space fixed  $z$ -axis [137].

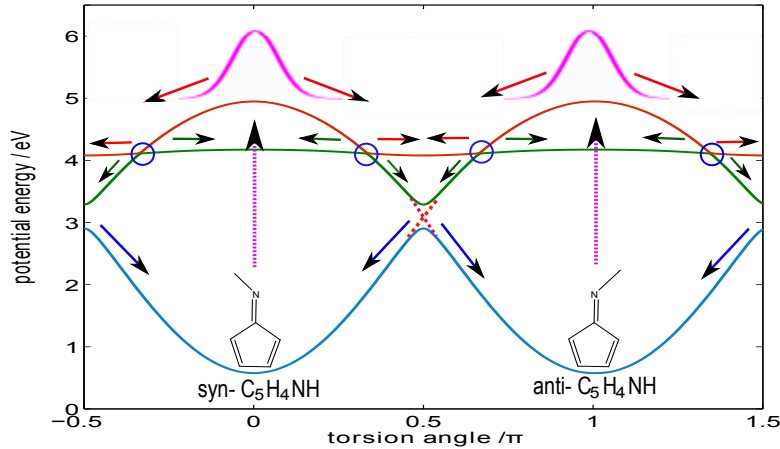


Figure 5.4.: Adiabatic potential energy curves for  $C_5H_4NH$ , with syn- and anti-form localized in the left and right well of the potential, respectively. The arrows describe the motion of H-atom after excitation and the decay through the conical intersections (blue circles) and avoided crossing (red dashed lines).

The initial wavefunction  $\psi_{\text{nuc}}^0(\phi, 0)$  is assumed to be the ground torsional state in  $V_0$ . Figures 5.5(a) and (b) show the lowest symmetric (light green line in (a)) and anti-symmetric (orange line in (b)) eigenfunctions of the potential  $V_0$ , with symmetry  $A_1$  and  $B_2$ , respectively. The anti-symmetry principle states that it depends on the nuclear spin of the molecule whether the torsional ground states has  $A_1$  or  $B_2$  symmetry [50, 136]. If the laser pulse is short enough to induce a vertical transition to the excited state  $S_2$ , the wave function immediately after the interaction can be written as

$$\vec{\psi}_{\text{nuc}}(\phi, 0) = \begin{pmatrix} \psi_{\text{nuc}}^2(\phi, 0) \\ 0 \\ 0 \end{pmatrix} \quad (5.17)$$

with

$$\psi_{\text{nuc}}^2(\phi, 0) = C\mu_z^{0,2}\psi_{\text{nuc}}^0(\phi, 0) \quad (5.18)$$

where  $C$  is constant. In this part of the investigation, the transition dipole moment in the Frank-Condon region, i.e. at  $\phi \approx 0$  and  $\phi \approx \pi$ , is assumed to be constant. However, the symmetry of  $\mu_z^{0,2}$  is taken in account, see Table 5.1.

In the following, the photo-excitation for case I and II (Table 5.1) is compared. In case I,  $\mu_z^{0,2}$  transforms as  $B_2$ . As a consequence, if  $\psi_{\text{nuc}}^0(\phi, 0)$  is anti-symmetric, i.e. transforms as  $B_2$ , then  $\psi_{\text{nuc}}^2(\phi, 0)$  is symmetric, i.e. transforms as  $A_1$ , and vice versa, as it can be seen in

Fig.5.5 (a) and (b). In case II, the transition dipole moment  $\mu_z^{0,2}$  transforms as  $A_1$ . This implies that the wavefunction after excitation  $\psi_{\text{nuc}}^2(\phi, 0)$  is symmetric, i.e. transforms as  $A_1$ , if the initial wavefunction  $\psi_{\text{nuc}}^0(\phi, 0)$  is symmetric, see Fig.5.5(c).

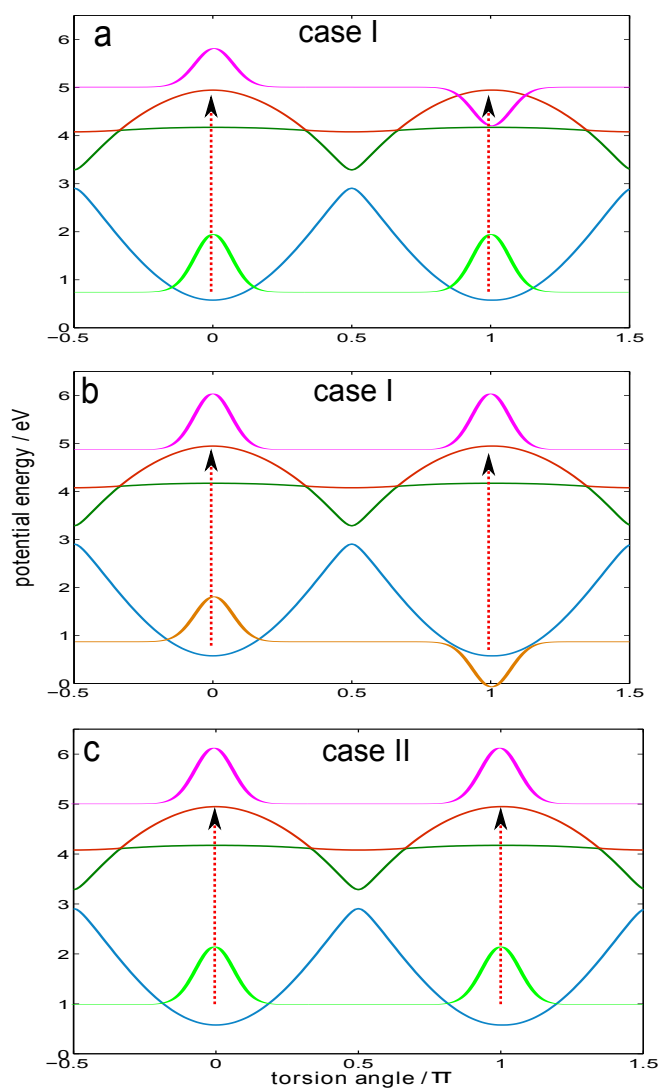


Figure 5.5.: Symmetric (a) and anti-symmetric (b) initial wavefunction  $\psi_{\text{nuc}}^0(\phi, 0)$  and wavefunction  $\psi_{\text{nuc}}^2(\phi, 0)$  after excitation with short laser pulse (indicated by dashed arrow) for case I. (c) symmetric initial wavefunction  $\psi_{\text{nuc}}^0(\phi, 0)$  and symmetric wavefunction  $\psi_{\text{nuc}}^2(\phi, 0)$  after excitation for case II.

## 5.5. Effect of the IREPs of the NACTs and Transition Dipoles on the Radiation-less Decay

In this section, the photo-induced movement of the H-atom and resulting radiation less decay is investigated. The process is sketched in Fig.5.4. The result of the effect of the IREPs of the NACTs, transition dipole moments and wavefunctions on the radiation-less decay will be presented for different examples. The first and second example are torsional potentials of  $C_5H_4NH$  with different radii, i.e. two values of  $r$  ( $\approx 0.8$  and  $\approx 1.0$  Å). The PESs and NACTs of the two examples are presented in Section 5.2. In third example  $C_5H_4ND$  is considered instead of  $C_5H_4NH$ .

The simulation of the time-evolution is done using the split operator method implemented in the program package Wavepacket [134]. For the simulation, the Hamiltonian is transformed to the diabatic representation, i.e.

$$\mathbf{H}^d = \mathbf{A}^\dagger \mathbf{H} \mathbf{A} = -\frac{\hbar^2}{2I_{red}} \frac{\partial^2}{\partial \phi^2} + \mathbf{W} \quad (5.19)$$

where  $\mathbf{W}$  the diabatic potential matrix,  $\mathbf{A}$  is the transformation matrix give in Eq.(2.63) and  $I_{red}$  is the reduced moment of inertia ( $I_{red} = 4898.36u \text{ \AA}^2$  for  $r \approx 0.8 \text{ \AA}$ ,  $6015.65u \text{ \AA}^2$  for  $r \approx 1.0 \text{ \AA}$ , and  $9743.86u \text{ \AA}^2$  for  $C_5H_4ND$  with  $r \approx 1.0 \text{ \AA}$ ). The spatial grid used in the simulation is  $\Delta\phi = 0.0123$  radians which correspond to 1024 grid points in the domain  $-\pi/2 \leq \phi \leq 3\pi/2$ . The time steps for the split operator are  $\Delta t = 0.024$  fs. The subsequent results are presented in adiabatic representation. After excitation with laser pulse, the wave packet start moving on the three coupled potentials and the populations of the three electronic states are calculated using the following formula

$$P^i(t) = \int_{-\pi/2}^{3\pi/2} |\psi_{nuc}^i(\phi, t)|^2 d\phi \quad (5.20)$$

with  $i=0$  for  $S_0$ ,  $i=1$  for  $S_1$  and  $i=2$  for  $S_2$ .

### 5.5.1. Isotope Effect on Radiation-less Decay

After excitation with laser pulse, the wavepacket starts moving on three coupled potentials. Figure 5.6 (a) shows the adiabatic population of the electronic state  $S_2$  (red line),  $S_1$  (green line) and  $S_0$  (blue line) as a function of time for the cut of the PES with  $r \approx 1.0$  Å using a initially symmetric wavefunction. During the first 5 fs the wavepacket is localized on the  $S_2$ -state, then the wavepacket starts to decay to the electronic state  $S_1$

through the  $S_2/S_1$  conical intersections, see Fig. 5.4. After 20 fs approximately 50% of the wavepacket has decayed into the first excited state while  $S_0$  is almost empty. At  $t \approx 18$  fs the wavepacket starts populating in the ground states and within time the population increases up to 30% at  $t \approx 27$  fs. As the time increases the population alternates between the highest electronic states and  $S_1$  and  $S_0$ . At  $t \approx 70$  fs, 85% of the wavepacket is again in the second electronic state  $S_2$ . After a while, the wavepacket decays again to the first electronic state  $S_1$ , then to  $S_0$ .

Figure 5.6 (b) shows the adiabatic population of three electronic states  $S_2$  (red line),  $S_1$  (green line) and  $S_0$  (blue line) for C<sub>5</sub>H<sub>4</sub>ND with  $r \approx 10$  Å. This case is shown in order to compare the movement of light H-atom with the movement of the heavier D-atom on the three electronic states. Here, the reduced moment of inertia is  $I_{red} = 9743.86 \text{u} \text{Å}^2$ . The adiabatic population shows that the wavepacket start to decay from the electronic state  $S_2$  into  $S_1$  after approximately 18 fs, while in H-atom movement case, the decay already starts after 10 fs. This is due to the slower movement of the heavier atom. Moreover, only 35% of the wavepacket decayed into the  $S_1$  at  $t \approx 22$  fs which is less than for the H-atom case. At  $t \approx 22$  fs the wavepacket starts to decay into the ground state. Approximately 20% of the wavepacket is transferred into the ground state at  $t \approx 38$  fs, which is also less than in the H-atom case. The C<sub>5</sub>H<sub>4</sub>NH case is chosen to serve as model for subsequent investigation since, it is show large radiation-less decay for higher excited state to the ground more than for C<sub>5</sub>H<sub>4</sub>ND case.

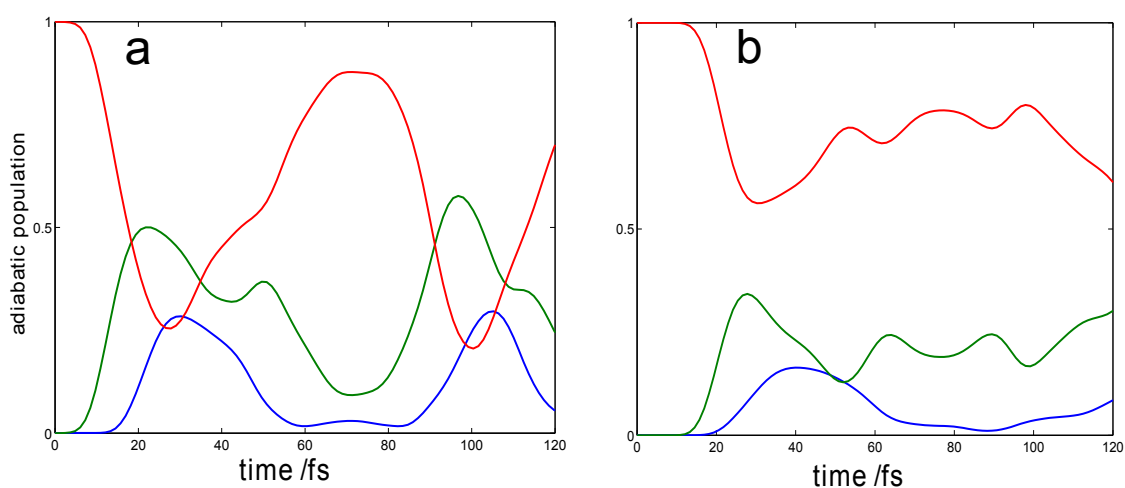


Figure 5.6.: Adiabatic population in  $S_2$  (red lines),  $S_1$  (green lines) and  $S_0$  (blue lines) after excitation for (a) C<sub>5</sub>H<sub>4</sub>NH with  $r \approx 1.0$  Å and (b) C<sub>5</sub>H<sub>4</sub>ND with  $r \approx 1.0$  Å using initially symmetric wavefunctions.



### 5.5.2. Effects of the Symmetry of the Initial Wavefunctions

As sketched in Fig.5.5 (a) and (b), the torsional ground state of  $V_0$  can be either symmetric ( $A_1$  in  $C_{2v}(M)$ ) or anti-symmetric ( $B_2$  in  $C_{2v}(M)$ ). Due to the high torsional barrier in  $V_0$ , the two states are almost degenerate. In the following, we investigate how the symmetry of the initial wavefunction affects the radiation-less decay.

The wavefunction symmetry effect on the radiation-less decay is investigated for  $C_5H_4NH$  with  $r \approx 1.0$  Å. Figure 5.7(a) shows the adiabatic population of three electronic states,  $S_0$  (blue lines),  $S_1$  (green lines) and  $S_2$  (red lines) using symmetric (dashed lines) and anti-symmetric (continuous lines) initial wavefunctions corresponding to case I, see Section 5.5.2. The Figure shows that after excitation with a  $\delta$ -pulse, the wavepacket starts moving on the three coupled potentials as described in the previous section. The adiabatic population during the first 20 fs shows no difference between symmetric and anti-symmetric initial wavefunction.

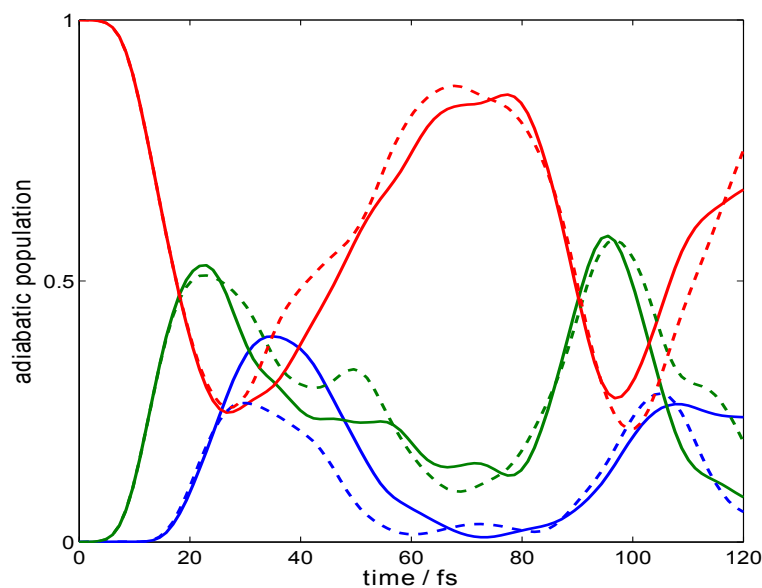


Figure 5.7.: Comparison of the adiabatic populations for an initially anti-symmetric wavefunction (solid lines) and for a symmetric wavefunction (dashed lines) for case I for the cut of the PES with  $r \approx 1.0$  Å. The population of state  $S_2$  is shown in red color, of  $S_1$  in green and of  $S_0$  in blue lines.

The difference between initially symmetric and anti-symmetric wavefunctions at  $t \approx 35$  fs can be seen in particular in the ground electronic state with population of 28% for the initially symmetric wavefunction and 43% for the initially anti-symmetric wavefunction. This effect can be seen more pronounced for the second cut with  $r \approx 0.8$  Å.

Figure 5.8(a) and (b) show the adiabatic population of the electronic states  $S_2$  (red lines),  $S_1$  (green lines) and  $S_0$  (blue lines) as a function of time for the cut of the PES with  $r \approx 0.8$  Å. Panel (a) corresponds to a initially symmetric wavefunction and panel (b) correspond to a initially anti-symmetric wavefunction.

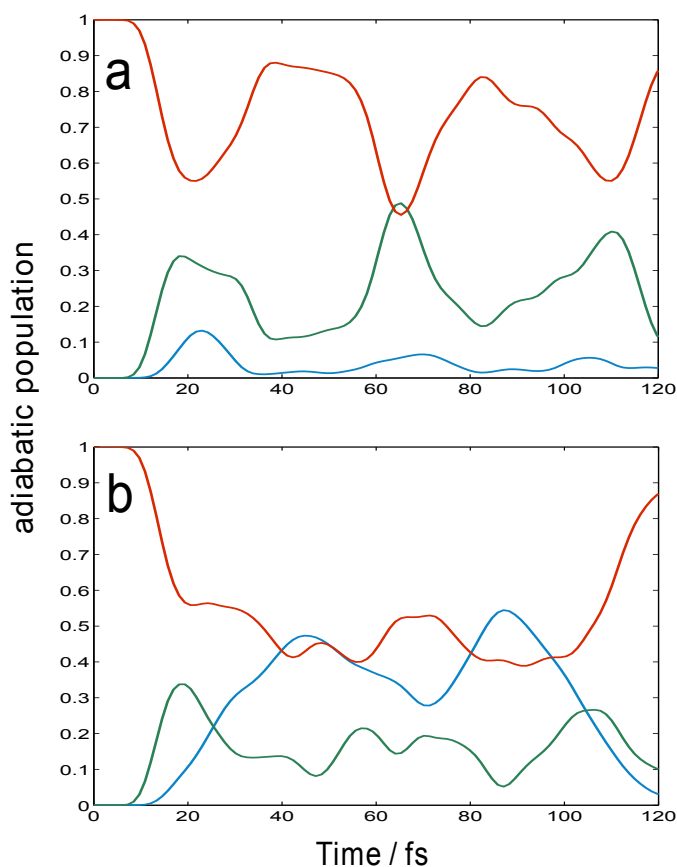


Figure 5.8.: Adiabatic population in  $S_2$  (red lines),  $S_1$  (green lines) and  $S_0$  (blue lines) after excitation for (a) initially symmetric wavefunction and (b) anti-symmetric wavefunction for case I for the cut of the PES with  $r \approx 0.8$  Å.

In both situations, the wavepacket starts to decay from  $S_2$  to  $S_1$  after 10 fs. Another 5 fs

later part of the population is transferred to the ground state  $S_0$ . Again, during the first 20 fs, the time-evolution of the symmetric and anti-symmetric wavefunction is the same.

Afterwards, interference between the left and right part of the wavefunctions lead to rather different behaviours, as shown in Figs.5.8(a) and (b). In Fig.5.8(a), the electronic ground state is almost empty and the population oscillates between the first and second excited states via the  $S_1/S_2$  conical intersections at  $\phi = \pm 0.33\pi$  and  $\phi = \pi \pm 0.33\pi$ . The symmetry of the wavefunction prevents its decay to the ground state: As it can be seen in Fig.5.1(a), the coupling between  $S_1$  and  $S_0$  is strongest at  $\phi = \pi/2$  and  $\phi = 3\pi/2$ . The probability density  $|\psi_{\text{nuc}}^1(\phi, t)|^2$ , shown in Fig.5.9(a) and (a') in blue lines for  $t = 22$  fs has a node at  $\phi = \pi/2$  and  $\phi = 3\pi/2$  which prevents effective radiation-less decay to the ground state.

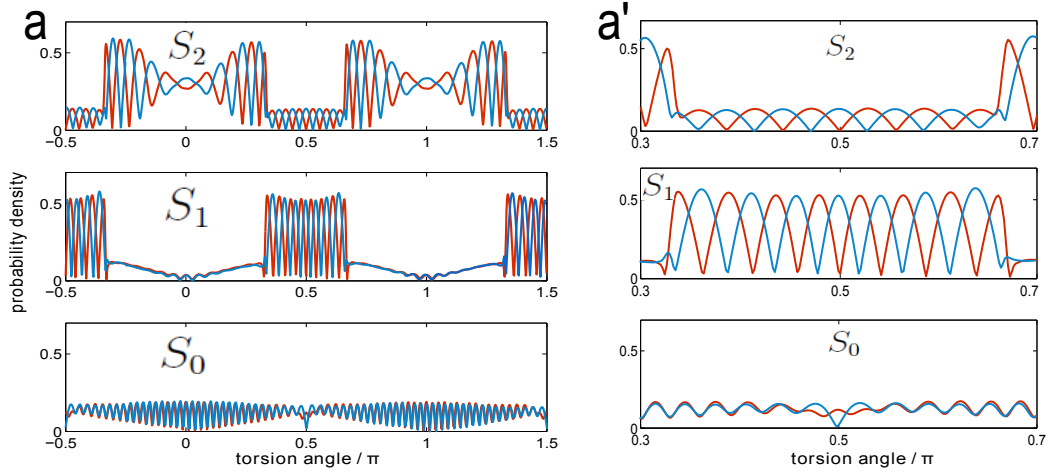


Figure 5.9.: Probability densities in the electronic states  $S_2$ ,  $S_1$  and  $S_0$  at  $t = 22$  fs after excitation. Panel (a) shows  $|\psi_{\text{nuc}}^i(\phi, t = 22 \text{ fs})|^2$  for  $i = 0, 1, 2$  for symmetric (red lines) and anti-symmetric (blue lines) initial wavefunctions for case I. Panel (a') shows a magnification of  $|\psi_{\text{nuc}}^i(\phi, t = 22 \text{ fs})|^2$  close to  $\phi = \pi/2$ .

In Fig. 5.8(b), we find a different behaviour. After  $t \approx 50$  fs, approximately 50% of the population has decayed to the ground state. The probability density  $|\psi_{\text{nuc}}^1(\phi, t)|^2$  has local maxima at  $\phi = \pi/2$  and  $\phi = 3\pi/2$ , see Fig.5.9(a) and (a')(red lines). These maxima promote the population transfer to the ground state.

In conclusion, the difference in the dynamics of symmetric and anti-symmetric initial wavefunction is an interesting subject. Since the symmetry of the torsional wave function

is determined by the nuclear spin of the molecule [50, 136], differences in the photo-induced torsional dynamics and radiation less decay open possibilities for the separation of the nuclear spin isomers.

### 5.5.3. Effects of the IREPs of the NACTs and Transition Dipole Moments

In Section 5.2, we presented two cases in which the NACTs and, as a consequence, the transition dipole moments have different IREPs. Here, we show by comparison of the two cases how the IREPs of the NACTs affect the torsional dynamics and the radiation-less decay. In order to achieve this goal, we consider the cut with  $r \approx 0.8 \text{ \AA}$  which has large coupling elements between  $S_1$  and  $S_2$ . Since the sign pattern of these coupling elements differs between case I and case II, the influence of the symmetry is expected to be particularly pronounced for this example. Moreover, the symmetric wavefunction is used as initial wave function in both cases. The photo-excitation for the two cases are depicted in Fig.5.5 (a) and (c). Figure 5.10 shows the comparison of the adiabatic populations in three electronic states for case I (solid lines) and case II (dashed lines). The populations in both cases are the same during the first 20 fs after excitation, while after  $t = 20$  fs they start to deviate.

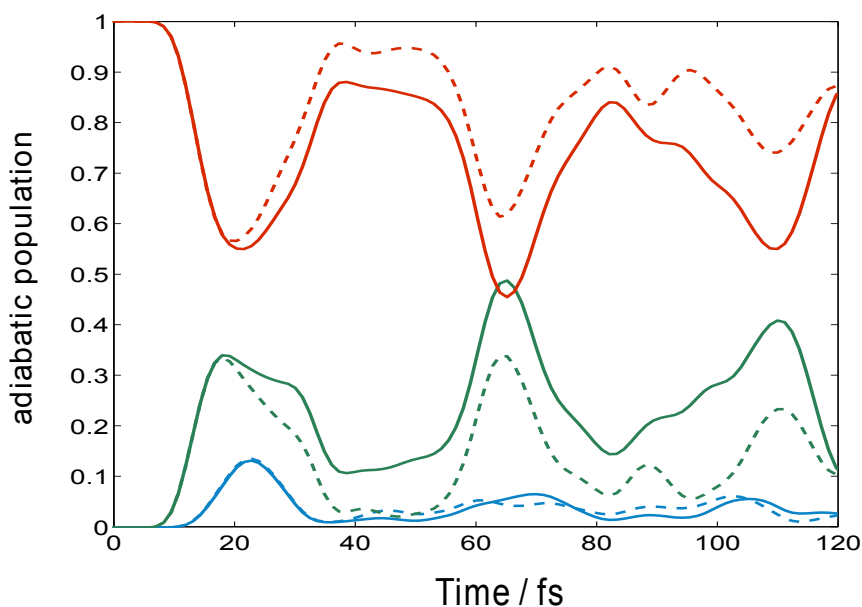


Figure 5.10.: Comparison of the adiabatic populations for case I (solid lines) and case II (dashed lines) for an initially symmetric wavefunction.

One can notice two important points here: First, the wave function  $\psi_{\text{nuc}}^2(\phi, 0)$  in case I is anti-symmetric, while for case II it is symmetric, see Fig.5.5. Figure 5.11(a) shows that at  $t=22$  fs the probability density function  $|\psi_{\text{nuc}}^2(\phi, t)|^2$  in case I (red lines) has a node (minimum) at  $\phi = \pi/2$  while in case II (blue lines) it has a maximum. Nevertheless, in both cases the population in the three electronic states is similar. In particular, the decay to the ground state is prevented also in case II, where  $\psi_{\text{nuc}}^2(\phi, 0)$  is symmetric. Due to the NACTs  $\tau_{\phi}^{1,2}(\phi)$  between the electronic states  $S_2$  and  $S_1$ , the nuclear wavefunction for case II requires an additional phase, different from case I, since the IREPs of  $\tau_{\phi}^{1,2}(\phi)$  are different. As a consequence, the probability density  $|\psi_{\text{nuc}}^1(\phi, t = 22 \text{ fs})|^2$  has nodes at  $\phi = \pi/2$  and  $\phi = 3\pi/2$ , see Fig.5.11 panels (a) and (a'), as in case I, and therefore the decay to ground state  $S_0$  is hindered.

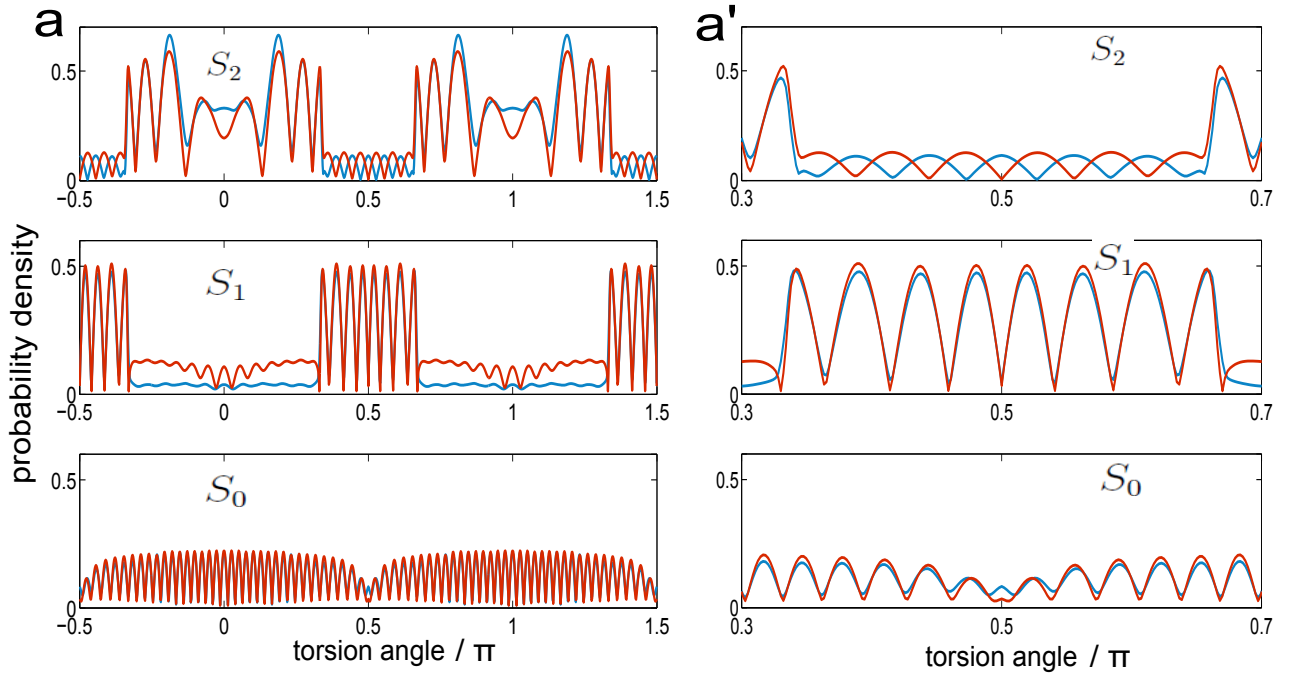


Figure 5.11.: Probability densities in the electronic states  $S_2$ ,  $S_1$  and  $S_0$  at  $t=22$  fs after excitation. Panel (a) shows  $|\psi_{\text{nuc}}^i(\phi, t = 22 \text{ fs})|^2$  for  $i=0,1,2$  for symmetric initial wavefunction for case I (red lines) and case II (blue lines). Panel (a') shows a magnification of  $|\psi_{\text{nuc}}^i(\phi, t = 22 \text{ fs})|^2$  close to  $\phi = \pi/2$ .

The second important issue is that after approximately  $t \approx 22$  fs, a difference in the radiation-less decay for cases I and II, is observed. In both cases the initial wavefunction, adiabatic potential, absolute values of the NACTs and the transition dipole are identical. The only difference between case I and case II is the molecular symmetry of the initial excited states, electronic states, due to the different IREPs of the NACTs and the transition dipole moments. These differences leads to different adiabatic population between two cases. In particular, the wavefunction transfer to the intermediate state  $S_1$  in case I is larger than in case II, see Fig.5.10.

After  $t \approx 65$  fs, 49% of the population populated is in state  $S_1$  in case I, while in case II only 35 % is present in state  $S_1$ . In order to further analyze this difference in the wavepacket evolution, it is useful to calculate the angular expectation values. The angular expectation values  $\langle \cos(2\phi) \rangle$  are given by

$$\langle \cos(2\phi) \rangle_i = \frac{\langle \psi_{\text{nuc}}^i | \cos(2\phi) | \psi_{\text{nuc}}^i \rangle}{\langle \psi_{\text{nuc}}^i | \psi_{\text{nuc}}^i \rangle} \quad (5.21)$$

The angular expectation values for state  $S_2$ , i.e.  $i=2$ , and for  $S_1$ , i.e.  $i=1$  are shown in Fig.5.12 panels (a) and (b), respectively. The angular expectation value for case I represented in red lines, while the blue lines correspond to case II.

The angular expectation value is approximately one ( $\langle \cos(2\phi) \rangle \approx 1$ ), if the wavepacket is localized at  $\phi \approx 0$  or  $\phi \approx \pi$ , while  $\langle \cos(2\phi) \rangle \approx -1$  for a wavepacket localized at  $\phi = \pi/2$  and  $\phi = 3\pi/2$ , and a uniform distribution in the interval  $-\pi/2 \leq \phi \leq 3\pi/2$  corresponds to  $\langle \cos(2\phi) \rangle \approx 0$ .

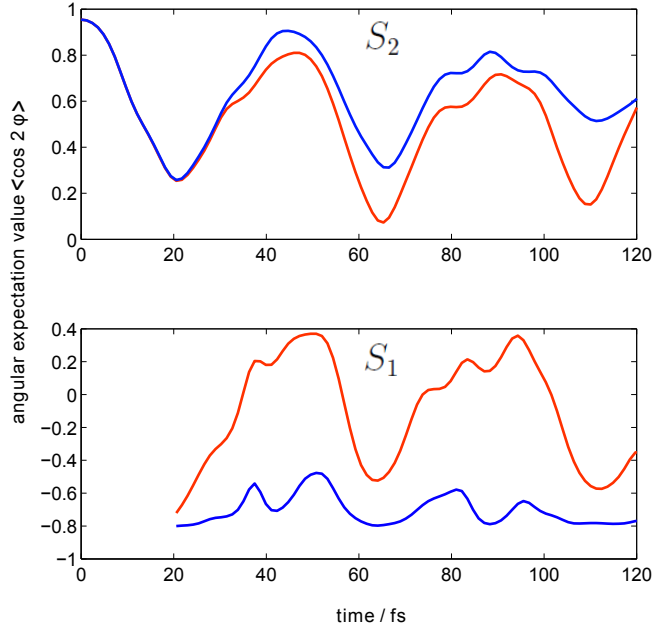


Figure 5.12.: Expectation values  $\langle \cos(2\phi) \rangle_i$  for  $i=2$  (a) and  $i=1$  (b) as a function of time. The red and blue curves correspond to cases I and II, respectively.

The expectation values show that in both cases at  $t=0$  fs, the wavefunction  $\psi_{\text{nuc}}^2(\phi, t=0)$  is localized at the torsion angle  $\phi = 0$  and  $\phi = \pi$  so that  $\langle \cos(2\phi) \rangle_2 \approx 1$ , see Fig.5.12(a). As the wavepackets disperse and become localized again with time  $\langle \cos(2\phi) \rangle_2$  decreases and increases again. With time, the differences between case I and case II becomes larger. In case II, the wavefunction tends to be more localized at  $\phi = 0$  and  $\phi = \pi$ . The difference in  $\langle \cos(2\phi) \rangle$  between the two cases is more pronounced in electronic state  $S_1$  (Note that in Fig.5.12(b) the expectation value  $\langle \cos(2\phi) \rangle_1$  is not plotted for  $t \leq 20$  fs since numerical meaningful expectation values can be calculated only if there is enough population in the electronic state to evaluate the corresponding integrals). At  $t = 20$  fs the expectation values for both cases are similar with  $\langle \cos(2\phi) \rangle_1 \approx -0.7$  to  $-0.8$ . Since the coupling between the electronic state  $S_1$  and  $S_2$  is most effective at the torsion angle  $\phi \approx \pm 0.33\pi$  and  $\phi \approx \pi \pm 0.33\pi$ , the wavefunction in state  $S_1$  is initially localized between  $\phi = \pm 0.33\pi$  and  $\phi = \pi \pm 0.33\pi$ , which is close to  $\phi = \pi/2$  and  $\phi = 3\pi/2$ . Thus,  $\langle \cos(2\phi) \rangle_1$  is close to  $-1$ . In case I (red line), the  $\langle \cos(2\phi) \rangle_1$  value increases to approximately  $0.37$ , while in case II (blue line), it oscillates between  $-0.7$  to  $-0.8$ , as shown in Fig.5.12 (b).

Figure 5.13 panels (a) and (b) show the probability densities of  $|\psi_{\text{nuc}}^2(\phi, t = 44 \text{ fs})|^2$  and  $|\psi_{\text{nuc}}^1(\phi, t = 44 \text{ fs})|^2$  for both cases. The probability density  $|\psi_{\text{nuc}}^2(\phi, t = 44 \text{ fs})|^2$

for both cases it is similar, in accord with the similar results of  $\langle \cos(2\phi) \rangle_2$  for cases I and II, cf. Fig.5.13(a). Fig.5.13(b) shows that in case II the wavefunction is trapped in the potential minima of  $V_1$  at  $\phi = \pi/2$  and  $\phi = 3\pi/2$  while it is spread over the whole range of torsion angle in case I.

In conclusion, the IREPs of the NACTs and the transition dipole moments effect significantly the radiation-less decay and dispersion of the torsional wavepackets in the excited electronic states.

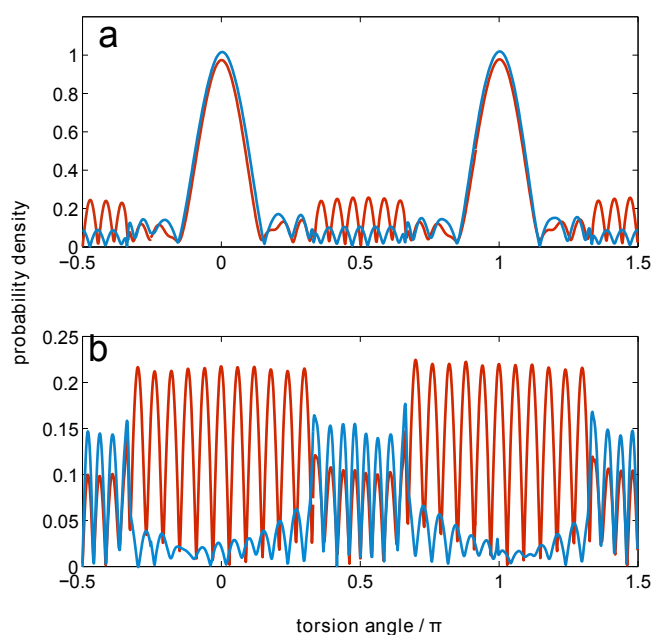


Figure 5.13.: The probability densities  $|\psi_{\text{nuc}}^2(\phi, t)|^2$  (a) and  $|\psi_{\text{nuc}}^1(\phi, t)|^2$  (b) at  $t = 44$  fs. The red and blue curves correspond to case I and II, respectively.

To fortify this statement, the nuclear dynamics is simulated for a situation where the two excited states are simultaneously populated due the interaction with short laser field. This scenario is possible due to the fact that in the Franck-Condon region ( $\phi \approx 0$  and  $\phi \approx \pi$ ) the energy difference between the electronic states  $S_1$  and  $S_2$  is  $\Delta E = 0.77\text{eV}$ . As a consequence, the bandwidth of a very short laser pulse with a pulse duration of few femtoseconds can exceed this energy gap. As a result, it is likely that a short laser pulse excites a wavepacket in both electronic states. Here, we choose again the symmetric torsional ground state as initial state for both cases, case I and case II. The wavepackets



after excitation are assumed to be

$$\vec{\psi}_{\text{nuc}}(\phi, 0) = \begin{pmatrix} \psi_{\text{nuc}}^2(\phi, 0) \\ \psi_{\text{nuc}}^1(\phi, 0) \\ 0 \end{pmatrix} \quad (5.22)$$

with

$$\psi_{\text{nuc}}^2(\phi, 0) = \frac{C}{\sqrt{2}} \mu_z^{0,2} \psi_{\text{nuc}}^0(\phi, 0). \quad (5.23)$$

$$\psi_{\text{nuc}}^1(\phi, 0) = \frac{C}{\sqrt{2}} \mu_z^{0,1} \psi_{\text{nuc}}^0(\phi, 0). \quad (5.24)$$

The symmetry of the excited wavefunction depends on the symmetry of the transition dipole moments  $\mu_z^{0,2}$  and  $\mu_z^{0,1}$ . Table 5.3 shows that  $\mu_z^{0,2}$  transforms according to  $B_2$  for case I and  $A_1$  for case II, while  $\mu_z^{0,1}$  is transformed according to  $B_2$  for both cases. The resulting wave functions  $\psi_{\text{nuc}}^2(\phi, 0)$  and  $\psi_{\text{nuc}}^1(\phi, 0)$  are shown in Fig.5.14(a) and (b) for cases I and II, respectively. It can be seen that for case I the wavefunction  $\psi_{\text{nuc}}^2(\phi, 0)$  and  $\psi_{\text{nuc}}^1(\phi, 0)$  have the same symmetry: they are both anti-symmetric. For case II, the wavefunction  $\psi_{\text{nuc}}^2(\phi, 0)$  is symmetric while  $\psi_{\text{nuc}}^1(\phi, 0)$  is anti-symmetric.

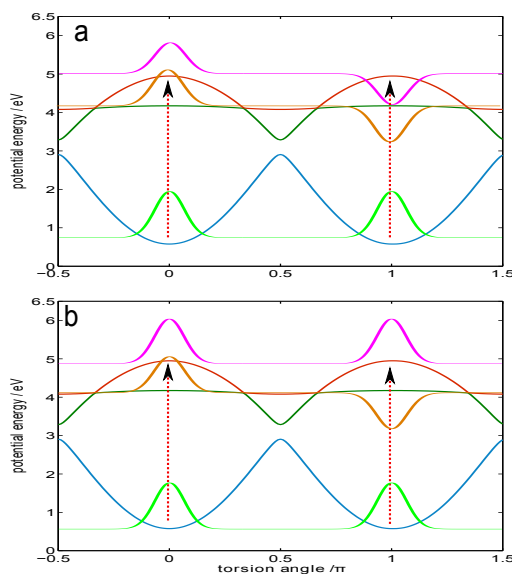


Figure 5.14.: The wavefunction after excitation with an ultra-short laser pulse for cases I (a) and II(b). The initial wavefunction  $\psi_{\text{nuc}}^0(\phi, 0)$  is the symmetric torsional ground state in both cases.

The populations of three electronic states after excitation are shown in Fig.5.15 for both cases. At the beginning, the time-evolution of the populations of both excited states are equal. Then, after  $t \approx 15$  fs the decay through the  $S_1/S_2$  conical intersection leads to increasing the  $S_1$  population (green lines) at the cost of the  $S_2$  population (red lines). As before, the population in the ground state  $S_0$  is almost zero, and the wavefunction oscillates between the excited states  $S_1$  and  $S_2$ . Moreover, differences in excited states populations between case I (solid lines) and case II (dashed lines) can be observed, and increasing with time as shown in Fig.5.16. If both excited states are initially populated (solid lines in Fig.5.16), the difference between case I and case II is even slightly enhanced for  $t \geq 100$  fs, compared to the case where only  $S_2$  is initially populated (dashed lines in Fig.5.16). In conclusion, the effect of the symmetry of the NACTs and transition dipole moments on the radiation-less decay are observed also if both excited electronic states are populated after photo-excitation.

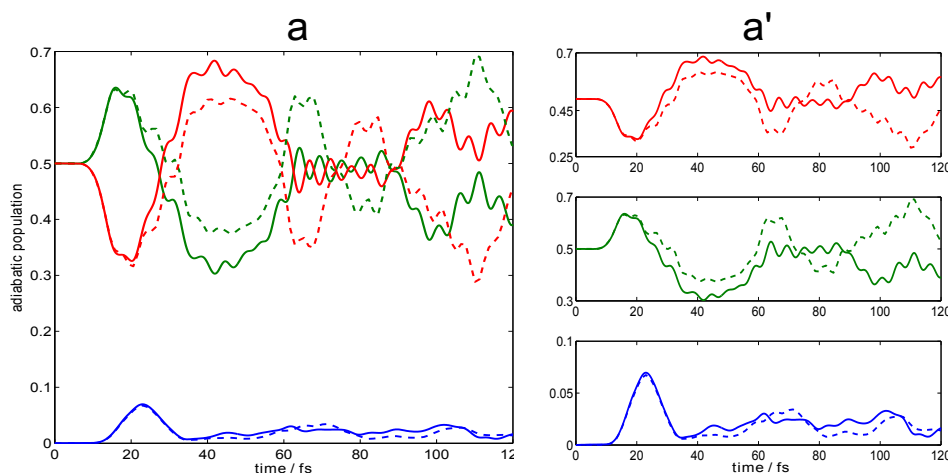


Figure 5.15.: (a) Populations of the electronic states  $S_2$  (red lines),  $S_1$  (green lines) and  $S_0$  (blue lines) for case I (solid lines) and for case II (dashed lines). Here,  $S_1$  and  $S_2$  are equally populated immediately after excitation. (a') is magnification.

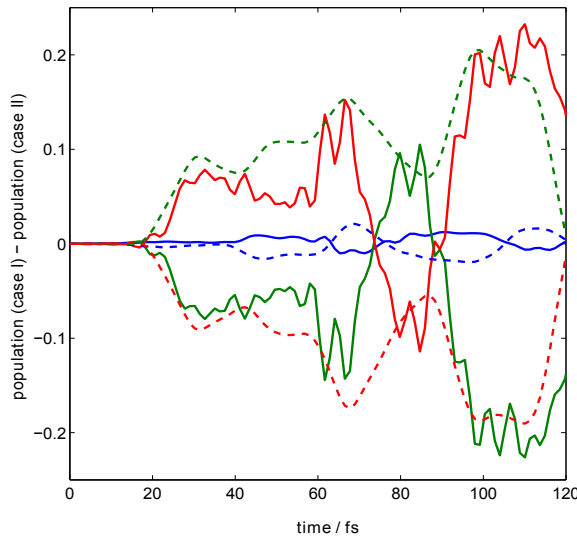


Figure 5.16.: Difference between case I and case II in the population of the electronic states  $S_2$  (red lines),  $S_1$  (green lines) and  $S_0$  (blue lines). The dashed lines correspond to the excitation of a initially symmetric wavefunction to state  $S_2$ . The solid lines correspond to simultaneous excitation of wavefunctions in  $S_1$  and  $S_2$ .

The effect of the molecular symmetry of the NACTs on the torsional dynamics is also investigated for the cut of the PES with  $r \approx 1.0 \text{ \AA}$ . The corresponding potentials and NACTs are shown in Fig.5.2(a) and (a'). The adiabatic population of the two cases presented in Section 5.2 with different IREPs of the NACTs and transition dipole moments are shown in Fig.5.17. The adiabatic population of three electronic states  $S_0$  (blue line),  $S_1$  (green line) and  $S_2$  (red line) are shown in continuous lines for case I and in dashed lines for case II. Here, we consider again initially symmetric wavefunction and assume that the wavefunction after excitation is

$$\vec{\psi}_{\text{nuc}}(\phi, 0) = \begin{pmatrix} \psi_{\text{nuc}}^2 \\ 0 \\ 0 \end{pmatrix} \quad (5.25)$$

As in all previous simulation, the adiabatic populations for case I and II are the same during the first  $\approx 20$  fs. After this, slight differences between case I and case II can be observed. For this cut of the PES, the differences between the two cases are much smaller than for the cut with  $r \approx 0.8 \text{ \AA}$ . For  $r \approx 1.0 \text{ \AA}$ , the large NACTs are those between  $S_0$

and  $S_1$ , i.e.  $\tau_\phi^{0,1}$ . Their symmetry ( $B_1$ ) is the same in case I and case II. The terms  $\tau_\phi^{1,2}$  have different symmetry ( $A_2$  in case I and  $B_1$  in case II). They are much smaller for the cut  $r \approx 1.0 \text{ \AA}$  than for the cut  $r \approx 0.8 \text{ \AA}$  (see Figs.5.1 and 5.2). Therefore, it is reasonable that the difference in the radiation-less decay between case I and case II are much smaller for the cut  $r \approx 1.0 \text{ \AA}$  than for  $r \approx 0.8 \text{ \AA}$ .

We have shown that the difference between case I and case II, i.e. the effect of molecular symmetry on the nuclear dynamics is always present, but more or less pronounced depending on the cut through the PES, which has been chosen for the simulations. An extension of this work to a more dimensional PES is demanding in order to demonstrate the total effect of molecular symmetry on radiation-less decay.

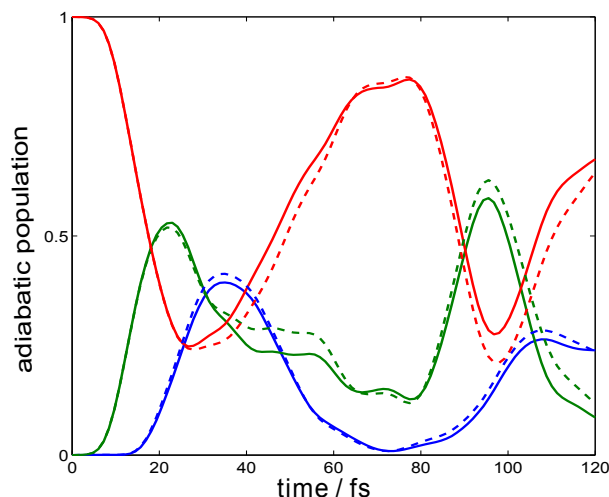


Figure 5.17.: The adiabatic populations for cases I (solid lines) and II (dashed lines) using the initially symmetric wavefunction. The populations of  $S_2$ ,  $S_1$  and  $S_0$  are shown in red, green and blue lines, respectively.

## 5.6. Interaction with a Laser Field

In the first part of this chapter the components of the transition dipole moments  $\mu_z^{i,j}$  are assumed to be constant in the Franck-Condon region i.e. at  $\phi \approx 0$  and  $\phi \approx \pi$ . As a consequence, the movement of the H-atom after excitation with the laser pulse has been simulated by neglecting the  $\phi$ -dependences of the dipole and transition dipole moments.

In this part of the study, the photo-induced dynamics of syn- and anti-C<sub>5</sub>H<sub>4</sub>NH, i.e. cis-trans isomerization about the C=N bond are investigated by taking into account that the  $\mu_z^{i,j}$  and  $\mu_z^{i,i}$  depend strongly on the torsion angle  $\phi$ . Moreover, the interaction with a laser pulse is taken into account explicitly. The torsion of the H-atom around the CN-axis is studied during and after excitation with a single laser pulse by numerically solving the TDSE, i.e. Eq. (5.12). In general, the interaction of the molecule with a z-polarized electric field in the adiabatic representation is given by Eq.(5.16) (see also Section 2.6). Here, the molecule is assumed to be oriented along the z-axis [137] and the laser field is z-polarized. For a three-state system,

$$H_{int} = -E(t) \begin{pmatrix} \mu_z^{2,2} & \mu_z^{2,1} & \mu_z^{2,0} \\ \mu_z^{1,2} & \mu_z^{1,1} & \mu_z^{1,0} \\ \mu_z^{0,2} & \mu_z^{0,1} & \mu_z^{0,0} \end{pmatrix} \quad (5.26)$$

where the laser pulse is given by

$$E(t) = E_0 \cos(\omega t) f(t) \quad (5.27)$$

with the amplitude  $E_0$ , the central frequency  $\omega$  and the envelope (shape function) given by

$$f(t) = \begin{cases} \sin^2\left(\frac{\pi t}{t_p}\right) & \text{for } 0 \leq t \leq t_p \\ 0 & \text{elsewhere.} \end{cases} \quad (5.28)$$

Here,  $t_p$  denotes the pulse duration.

As described in Section 5.5, the TDSE is solved in the diabatic representation, i.e.

$$i\hbar \frac{\partial}{\partial t} \vec{\psi}_{\text{nuc}}^d(\phi, t) = \left[ \mathbf{H}^d + \mathbf{H}_{int}^d(t) \right] \vec{\psi}_{\text{nuc}}^d(\phi, t) \quad (5.29)$$

where  $\mathbf{H}^d$  is given in Eq.(5.19).

The diabatic representation of the interaction Hamiltonian is

$$\mathbf{H}_{int}^d = -E(t) \begin{pmatrix} \mu_z^{2,2,d} & \mu_z^{2,1,d} & \mu_z^{2,0,d} \\ \mu_z^{1,2,d} & \mu_z^{1,1,d} & \mu_z^{1,0,d} \\ \mu_z^{0,2,d} & \mu_z^{0,1,d} & \mu_z^{0,0,d} \end{pmatrix} = -E(t) \boldsymbol{\mu}_z^d \quad (5.30)$$

with

$$\boldsymbol{\mu}_z^d = \mathbf{A}^\dagger \boldsymbol{\mu}_z \mathbf{A} \quad (5.31)$$

where  $\mathbf{A}$  is the transformation matrix defined in Eq.(4.49).

The wavepacket dynamics is simulated with the split operator method in the diabatic basis implemented in program package wavepacket [134]. The spatial grid used in the simulation is  $\Delta\phi = 0.0123$  radians which correspond to 2024 grid points in the domain  $-\pi/2 \leq \phi \leq 3\pi/2$ . The time steps for the split operator are  $\Delta t = 0.024$  fs. The results are then transformed back to the adiabatic picture.

## 5.7. Dipole Moments and Transition Dipole Moments

In Section 5.3 the symmetry of the transition dipole moments has been determined. The z-components of the dipole moments and transition dipole moments have been calculated by ab initio method using CAS(10,9)/cc-pVDZ level of theory, the CASSCF methodology implemented in the MOLPRO [32]. The dipole moments for the cuts with  $r \approx 1.0$  Å and  $r \approx 0.8$  Å are shown in Fig.5.18(a) and (b), respectively. All dipole and transition dipole moments presented in this chapter are calculated in the domain  $0 \leq \phi \leq 2\pi$ . As mentioned in Section 5.3, all dipole moments must have  $A_1$ -symmetry.

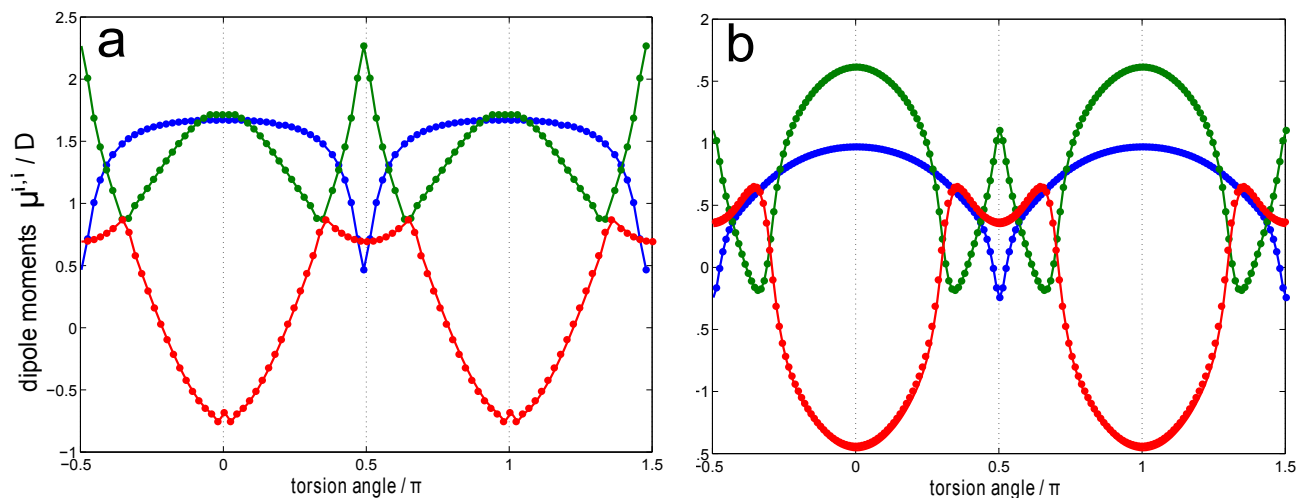


Figure 5.18.: The dipole moments  $\mu_z^{i,i}$  (a) for  $r \approx 0.8$  Å (b) for  $r \approx 1.0$  Å as a function of  $\phi$ . Here,  $\mu_z^{0,0}$  is shown in blue lines,  $\mu_z^{1,1}$  in green lines and  $\mu_z^{2,2}$  in red lines.

Figure 5.19(a) and (a') shows the transition dipole moments for the cut with  $r \approx 0.8$  Å. Note that the dots indicates the values that have been calculated quantum chemically. The

transition dipole moments components for case I transform as  $\Gamma(\mu_z^{0,1}) = B_2$ ,  $\Gamma(\mu_z^{0,2}) = B_2$  and  $\Gamma(\mu_z^{1,2}) = A_1$ , while in case II they transform as  $\Gamma(\mu_z^{0,1}) = B_2$ ,  $\Gamma(\mu_z^{0,2}) = A_1$  and  $\Gamma(\mu_z^{1,2}) = B_2$ . Figure 5.19 (a) and (a') show that for  $r \approx 0.8 \text{ \AA}$  the ab initio calculations of the transition dipole moments are compatible with case I as well as with case II. In case I, the sign pattern for  $\Gamma(\mu_z^{0,2})=B_2$  implies that  $\mu_z^{0,2}$  has a node at  $\phi = \pm\pi/2$ . For  $r \approx 0.8 \text{ \AA}$  this is in accordance with the data shown in Fig.5.19(a). However, for  $r \approx 1.0 \text{ \AA}$ ,  $|\mu_z^{0,2}(\phi = \pm\pi/2)| = 0.685$ , see Fig.5.19(b) and (b'). A node at  $\phi = \pm\pi/2$  is therefore in contradiction with the quantum chemistry results. Apparently, case I is ruled out - this is in contradiction to the results for the NACTs which support case I as shown in Section 5.3. In case II, however,  $\Gamma(\mu_z^{0,2})=A_1$  which does not require a node at  $\phi = \pm\pi/2$ , see Fig.5.19(b'). One should remember, however, that case II is not supported by the results for the NACTs, see Section 5.3. The other transition dipole moments are in accordance with both cases. We shall discuss this discrepancy in Appendix B.

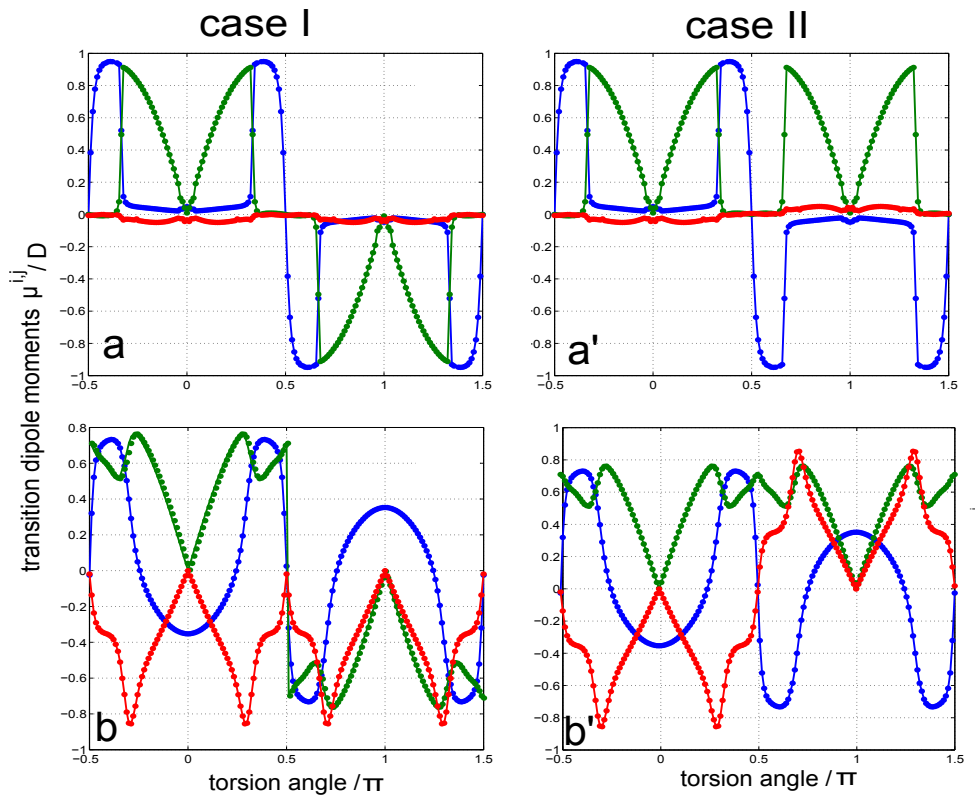


Figure 5.19.: The transition dipole moments  $\mu_z^{i,j}$ . Panels (a) and (a') show case I and case II for  $r \approx 0.8 \text{ \AA}$ . Panels (b) and (b') show case I and case II for  $r \approx 1.0 \text{ \AA}$ . Here,  $\mu_z^{0,1}$  is plotted in blue lines,  $\mu_z^{0,2}$  in green lines and  $\mu_z^{1,2}$  in red lines.

The transition dipole moments and dipole moments component must be transformed to the diabatic basis, i.e.  $\mu_z^d = \mathbf{A}\mu_z\mathbf{A}^\dagger$ . The diabatic transition dipole moments for  $r \approx 0.8$  Å for case I and case II are depicted in Fig.5.20 (a) and (a'). Panels (b) and (b') show the diabatic dipole moments for both cases for the same cut. The diabatic transition dipole moments for the cut with  $r \approx 1.0$  Å for case I and case II are depicted in Fig.5.21 (a) and (a'), respectively. Figure 5.21 (b) shows the dipole moments in diabatic basis for case I, while Panel (b') represent the diabatic dipole function for case II. In particular for the transition dipole moments, large differences between cases I and II can be noticed for both  $r \approx 0.8$  Å and  $r \approx 1.0$  Å.

Note also that the transformation to the diabatic representation does not preserve the IREPs of the adiabatic dipole and transition dipole functions. This effect of symmetry breaking already been observed for the diabatic potential matrix (see Section 5.2) and will be discussed in Section 5.10.

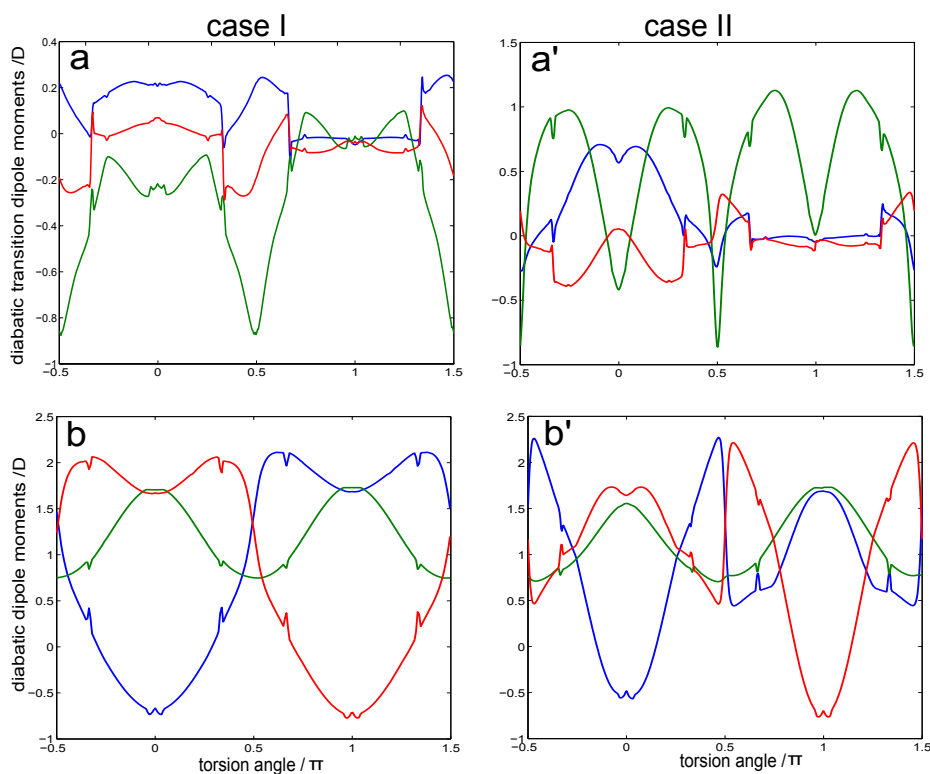


Figure 5.20.: Diabatic transition dipole moments  $\mu_z^{i,j,d}$  for the cut with  $r \approx 0.8$  Å. Panel (a) shows case I and (a') shows case II. The  $\mu_z^{0,1,d}$  is shown in blue lines,  $\mu_z^{0,2,d}$  in green lines and  $\mu_z^{1,2,d}$  in red lines. Panels (b) and (b') show the diabatic dipole moments  $\mu_z^{i,i,d}$  for cases I and II, respectively. Here  $\mu_z^{0,0,d}$  is depicted in blue lines,  $\mu_z^{1,1,d}$  in green lines and  $\mu_z^{2,2,d}$  in red lines.



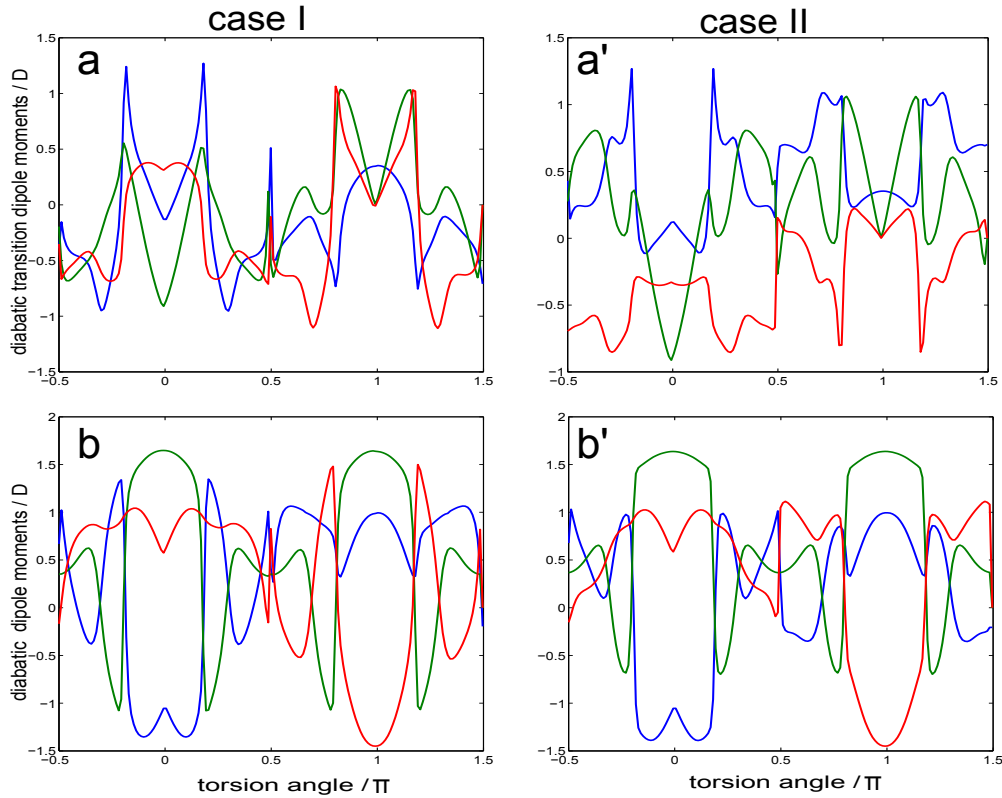


Figure 5.21.: Diabatic transition dipole moments  $\mu_z^{i,j,d}$  for the cut with  $r \approx 1.0$  Å. Panel (a) shows case I and (a') shows case II. The  $\mu_z^{0,1,d}$  is shown in blue lines,  $\mu_z^{0,2,d}$  in green lines and  $\mu_z^{1,2,d}$  in red lines. Panels (b) and (b') show the diabatic dipole moments  $\mu_z^{i,i,d}$  for case I and case II, respectively. Here  $\mu_z^{0,0,d}$  is depicted in blue lines,  $\mu_z^{1,1,d}$  in green lines and  $\mu_z^{2,2,d}$  in red lines.

## 5.8. Effect of Laser Pulse Parameters on Excitation

The torsion of the H-atom around the CN-bond is investigated after excitation with the short laser pulse which is defined in Eqs. (5.27) and (5.28). As a first step, the laser pulse parameters have to be chosen, such that a considerable amount of population is transferred to the excited electronics states after the end of the pulse. As a consequence, simulations with different laser pulse parameters are carried out. Here a wavefunction localized in the left potential well, i.e. a superposition of the symmetric and anti-symmetric eigenstates depicted in Fig.5.5 is used as initial wavefunction. Fig.5.22 shows the adiabatic population for the cut with  $\vec{s} = \{r \approx 1.0$  Å,  $\phi\}$  for case I using different pulse parameters. Figure 5.22 (a), (b) and (c) show the adiabatic population using pulses with large integrated intensity,

i.e. large  $E_0$  and long pulse duration. The results show strong oscillation in adiabatic population during the pulse and sudden change (exchange) of the population in  $S_1$  and  $S_2$ . By turning the frequency from  $\hbar\omega = 3.4989$  eV to  $\hbar\omega = 3.4274$  eV, the oscillation effect can be reduced but is still presents. A smooth transition of the population from ground state to the excited states can be obtained by using weaker and shorter pulse, as shown in Fig.5.22 (d), (e) and (f). Here, the smooth transfer from  $S_0$  to  $S_1$  during the pulse duration and the increases of the population in  $S_2$  due to the  $S_1/S_2$  CIs after the pulse can also be observed. The sudden change between the population in  $S_1$  and  $S_2$  during pulse can still be seen in panels (d) and (e). It disappears as the frequency decreases (panel f).

Therefore, the laser pulse parameters shown in Fig.5.22(f) are chosen for the simulations with  $r \approx 1.0$  Å: the frequency  $\hbar\omega = 3.4274$  eV, pulse duration  $t_p = 10$  fs and amplitude  $E_0 = 0.5144 \times 10^{10}$  V/m. The laser pulse amplitude is chosen such that the corresponding intensity  $I \approx 7 \times 10^{12} \frac{W}{cm^2}$  is less than Keldysh ionization limit, i.e.

$$I = \epsilon c E_0^2 \leq 10^{13} \frac{W}{cm^2} \quad (5.32)$$

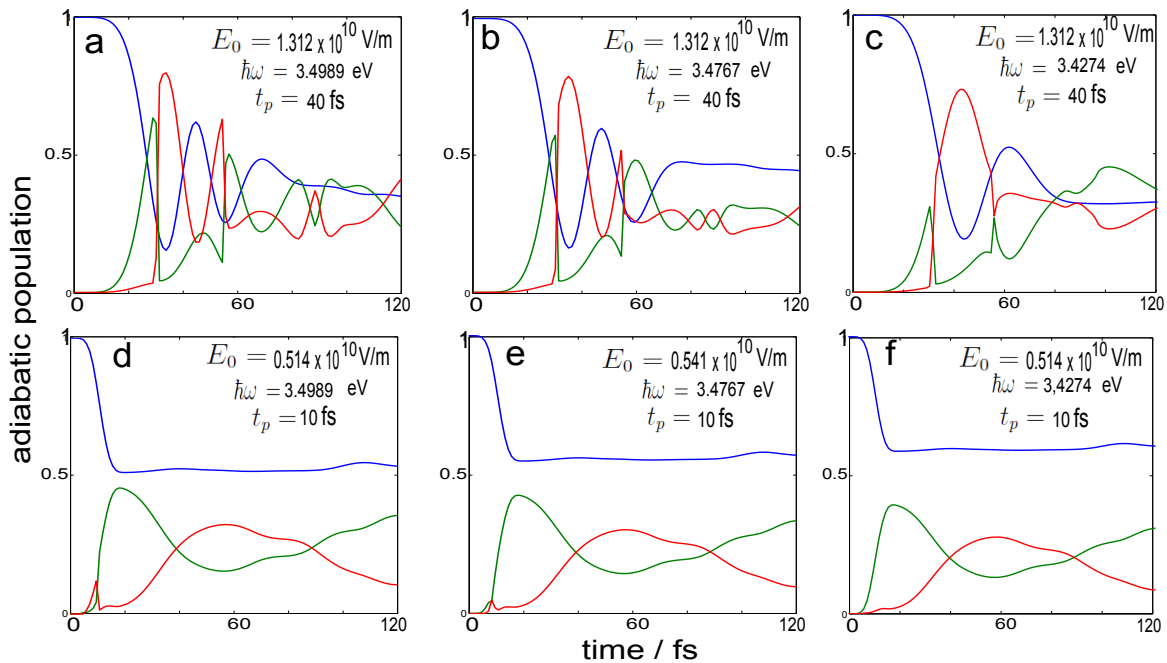


Figure 5.22.: Adiabatic population of  $S_0$  (blue lines),  $S_1$  (green lines) and  $S_2$  (red lines) for different laser pulse parameters for the cut with  $r \approx 1.0$  Å.

Also for the second example, i.e. for  $\vec{s} = \{r \approx 0.8 \text{ \AA}, \phi\}$ , simulations have been done for different laser pulse parameters in order to determine the useful laser parameters, the two examples are shown in Fig.5.23. We found that the laser pulse with frequency  $\hbar\omega = 4.159 \text{ eV}$ , pulse duration  $t_p = 10 \text{ fs}$  and amplitude  $E_0 = 0.643 \times 10^{10} \text{ V/m}$  which corresponds to  $I \approx 11 \times 10^{12} \frac{\text{W}}{\text{cm}^2}$  are suitable to reach at least 5-10% population in the two excited states. Here the frequency is chosen such that the population is excited basically only in  $S_2$  during the pulse. The state  $S_1$  become populated due to decay through the  $S_1/S_2$  CIs.

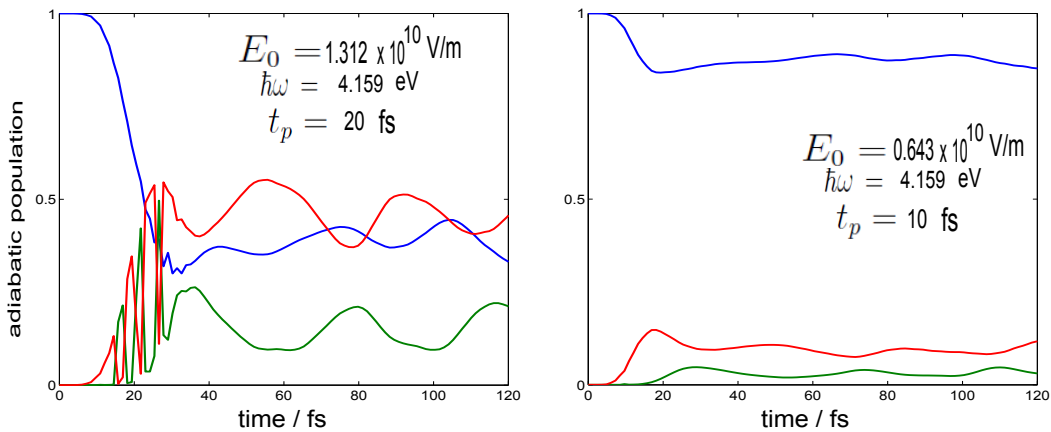


Figure 5.23.: Adiabatic population of  $S_0$  (blue lines),  $S_1$  (green lines) and  $S_2$  (red lines) for different laser pulse parameters for the cut with  $r \approx 0.8 \text{ \AA}$ .

## 5.9. Effects of the IREPs of the NACTs, Dipole and Transition Dipole Moments in Laser Pulse Induced Radiation-less Decay

Here, we investigate the effect of the IREPs of the NACTs, dipole and transition dipole moments and of the initial wavefunctions on the radiation-less decay after excitation with a laser pulse with parameters defined in Section 5.8. We first consider the cut with  $r \approx 0.8 \text{ \AA}$ . Again we compare case I and case II from Section 5.2 to observe the symmetry effects. Figure 5.24(a) shows the adiabatic population for both cases, case I depicted in solid lines and case II shown in dashed lines. The initial state is the symmetric torsional eigenstate of  $V_0$  (see Fig.5.4). The adiabatic population shows that the laser pulse excites

approximately 15% of the wavepacket to the second excited state. Then, after a while 5% of population decays from  $S_2$  to  $S_1$ . The differences between the two cases are small because the amount of population excited from the ground state  $S_0$  into the second excited states  $S_2$  is small, so the effect of the symmetry on the remaining population decay is small. It is seen mainly in the populations of the two excited states, amplified in Fig.5.24(a'). In Fig.5.24(b) the adiabatic populations of the two cases are shown for the initially anti-symmetric wavefunction. Here, the symmetry of the NACTs affects the radiation-less decay slightly stronger than for the initially symmetry wavefunction. In particular, at  $t \approx 60$  fs, the  $S_1$ -state is almost empty in case II (green dashed line in Fig.5.24(b) and (b')) while its population is approximately 3% populated in case I. At  $t \approx 105$  fs, the population in state  $S_1$  and  $S_2$  are approximately 5% and 12%, respectively for case I, while in case II approximately 0% populated in  $S_1$  and 16% populated in state  $S_2$ .

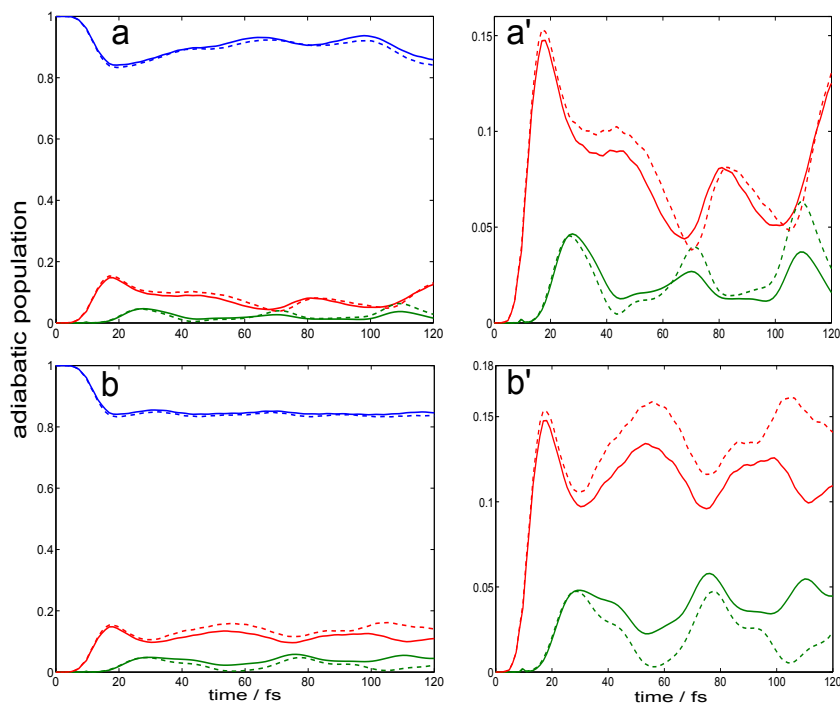


Figure 5.24.: Comparison of the adiabatic population for case I (solid lines) and case II (dashed lines) using (a) the initially symmetric wavefunction, and (b) the initially anti-symmetric wavefunction, (a') and (b') are magnifications. The population dynamics is induced by a laser pulse with intensity  $I \approx 11 \times 10^{12} \frac{W}{cm^2}$ , duration  $t_p = 10$  fs and frequency  $\hbar\omega = 4.159$  eV. Here, the population of  $S_0$  is shown in blue lines, of  $S_1$  in green lines and of  $S_2$  in red lines for the cut with  $r \approx 0.8$  Å.

Simulations for photo-excitation and subsequent radiation-less decay for the cut with  $r \approx 1.0 \text{ \AA}$  are shown in Fig.5.25. In panels (a) and (b) the adiabatic populations for the different states  $S_0$  (blue line),  $S_1$ (green lines)  $S_2$  (red lines) for case I (solid lines) and case II (dashed lines) are depicted for the initially symmetric and anti-symmetric wavefunctions, respectively. During the laser pulse interaction, nearly 30% of the adiabatic population is excited to the first excited state  $S_1$  in both cases. Moreover, approximately 2% is populated in the second electronic state  $S_2$ . At  $t \approx 40$  fs the two excited electronic states, i.e.  $S_1$  and  $S_2$ , are equally populated in both cases and the differences between the two cases are very small. The population of the ground state  $S_0$  is almost identical in both cases. The difference in the population of  $S_2$  increases with time up to  $\Delta P^2 \approx 6\%$  at  $t \approx 98$  fs, where  $\Delta P^2 = P^2(\text{caseI}) - P^2(\text{caseII})$  with  $P^2$  defined in Eq.(5.20).

In conclusion, differences in the radiation-less decay between the two cases with different symmetry can be observed also if the interaction with a laser pulse and the  $\phi$ -dependent of the transition dipole moments are taken into account explicitly. However, in particular for the cut with  $r \approx 0.8 \text{ \AA}$ , the effect is much smaller than in the simulations using the  $\delta$ -pulse excitation (see Section 5.5.3). The reason is that the laser pulse parameters used here lead only to small population transfer to the excited states. With laser pulses optimized for better population transfer to  $S_2$ , larger symmetry effects, compared to the ones observed in Section 5.5.3, are expected.

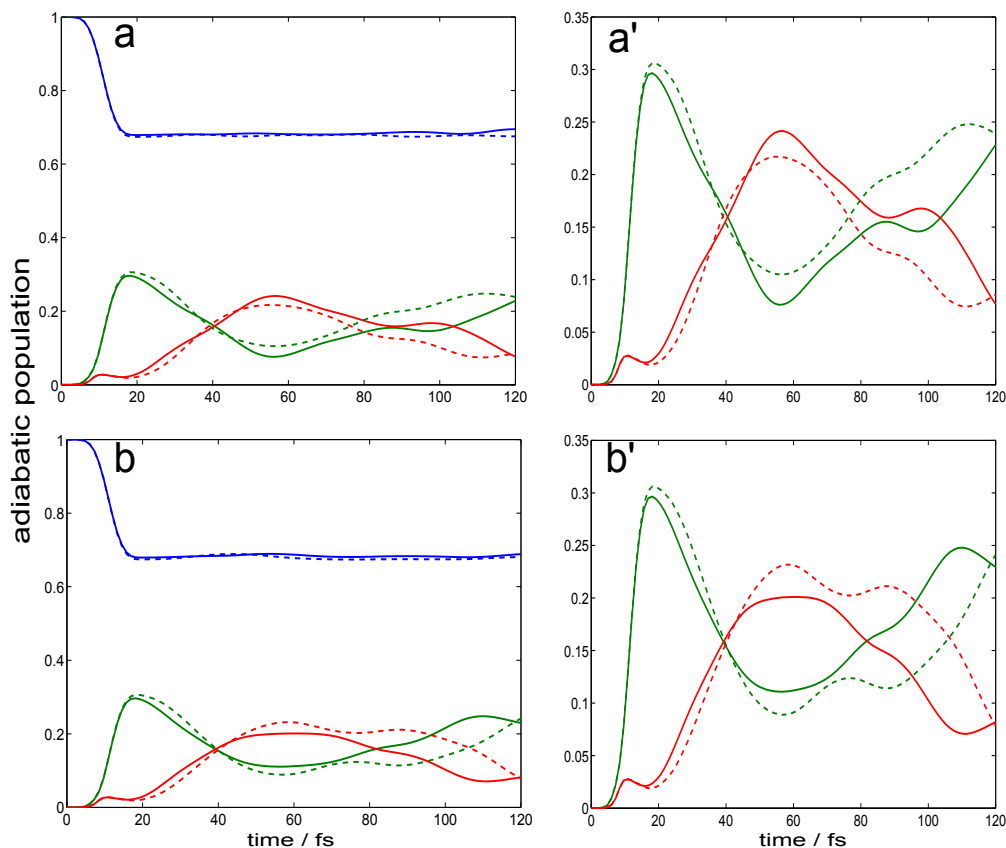


Figure 5.25.: Comparison of the adiabatic population for case I (solid lines) and case II (dashed lines) using (a) the initially symmetric wavefunction, and (b) the initially anti-symmetric wavefunction, (a') and (b') are magnifications. The population dynamics is induced by a laser pulse with intensity  $I \approx 7 \times 10^{12} \frac{W}{cm^2}$ , duration  $t_p = 10$  fs and frequency  $\hbar\omega = 3.4274$  eV. Here, the population of  $S_0$  is shown in blue lines, of  $S_1$  in green lines and of  $S_2$  in red lines for the cut with  $r \approx 1.0$  Å.

## 5.10. Radiation-less Decay in Diabatic and Adiabatic Representation

In this section, we compare the wavepacket dynamics in the adiabatic and diabatic representation. Figure 5.1 (c) and Fig.5.2(c) show that the symmetry of the potentials is not preserved after performing the transformation to the diabatic representation. In particular,  $W_{ii}(\phi = \pi) \neq W_{ii}(\phi = 0)$ , even if the torsion angles  $\phi = 0$  and  $\phi = \pi$  de-

scribe equivalent configurations of the system. The same can be seen for the dipole and transition dipole moments shown in Section 5.7. In the adiabatic representation, they transform according to the IREPs of the MS group but in the diabatic representation, they do not. Since all simulation are performed in the diabatic representation, the question arises whether a diabatic representation, which does not possess the symmetry of the system, can be used to obtain physical meaningful results.

To investigate this, we consider initial wavefunctions which are localized, in adiabatic representation, either in the left or in the right potential well, i.e. they are positive or negative linear combinations of the symmetric and anti-symmetric torsional eigenstates, respectively. Wavefunctions localized in the left and right potential well are physically indistinguishable. However, they "see" different diabatic potentials (see Fig.5.1 (c) and Fig.5.2(c)). The initial states in the adiabatic representation are shown in Fig.5.26, together with the corresponding diabatic functions. If the adiabatic wavefunction is localized in the left well, i.e. syn-form of  $C_5H_4NH$ , then  $\psi_{\text{nuc}}^0 \approx \psi_{\text{nuc}}^{0,d}$  with small contribution of the  $\psi_{\text{nuc}}^{1,d}$  and  $\psi_{\text{nuc}}^{2,d}$ . If the wavefunction is localized in the right well, i.e. anti-form of  $C_5H_4NH$ , the  $\psi_{\text{nuc}}^0 \approx \psi_{\text{nuc}}^{2,d}$  with small contribution of  $\psi_{\text{nuc}}^{0,d}$  and  $\psi_{\text{nuc}}^{1,d}$ . This comes from the fact that  $V_0 \approx W_{00}$  for  $\phi = 0$  and  $V_0 \approx W_{22}$  for  $\phi = \pi$ .

In the following, the nuclear TDSE is solved numerically in diabatic representation for both cases. The simulations are performed with 2024 grid points in the domain  $-\pi/2 \leq \phi \leq 3\pi/2$  using the split operator method as implemented in the program package Wavepacket [134]. The parameters of the laser pulses are defined in Section 5.8.

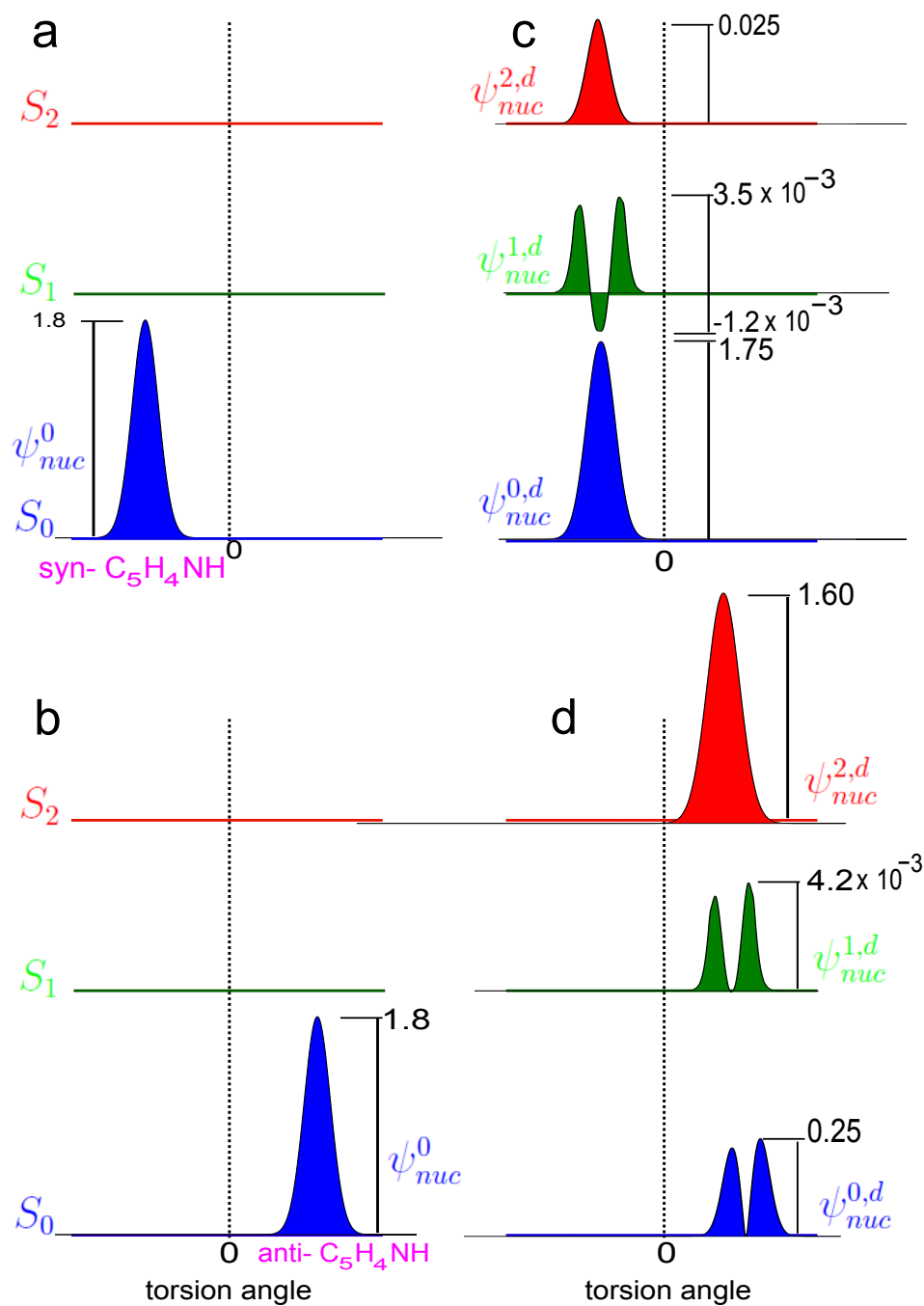


Figure 5.26.: Adiabatic initial wavefunction  $\psi_{nuc}^0(t = 0)$  localized in the left(a) and right (b) well of the potential for the cut with  $r \approx 1.0$  Å. The corresponding diabatic initial wavefunctions are shown in panels (c) and (d) with  $\psi_{nuc}^{0,d}$  in blue colours,  $\psi_{nuc}^{1,d}$  in green colours and  $\psi_{nuc}^{2,d}$  in red colours.



Figure 5.27 shows the population dynamics of the three electronic states during and after the laser pulse in the diabatic (a) and in the adiabatic (a') representation for a wavepacket which is initially localized on the left (solid lines) and on the right (dashed lines) adiabatic potentials for the cut with  $r \approx 0.8 \text{ \AA}$ . The overall dynamics is similar to the cases described before, and therefore not discussed in detail. It can be seen in Fig.5.27(a) that in the diabatic picture, the role of  $P^{0,d}$  and  $P^{2,d}$  is exchange for the left and right initial states. This comes from the fact that  $W_{00}$  and  $W_{22}$  cross at  $\phi = \pm\pi/2$ . Moreover, the diabatic populations show slight differences between  $P^{0,d}$  for the left case (solid blue line) and  $P^{2,d}$  for right case (dashed red line). Also the figure shows small differences between  $P^{2,d}$  for left (solid red line) and  $P^{0,d}$  for the right well potential (dashed blue line). These differences occur due to the small asymmetry of diabatic potentials which can be seen in Fig.5.1(c).

Transforming the result back to the adiabatic picture shows that the populations for the wavepacket localized on the left and right potential well are identical, see Fig.5.27(b). This is consistent with the fact that both situations are indistinguishable.

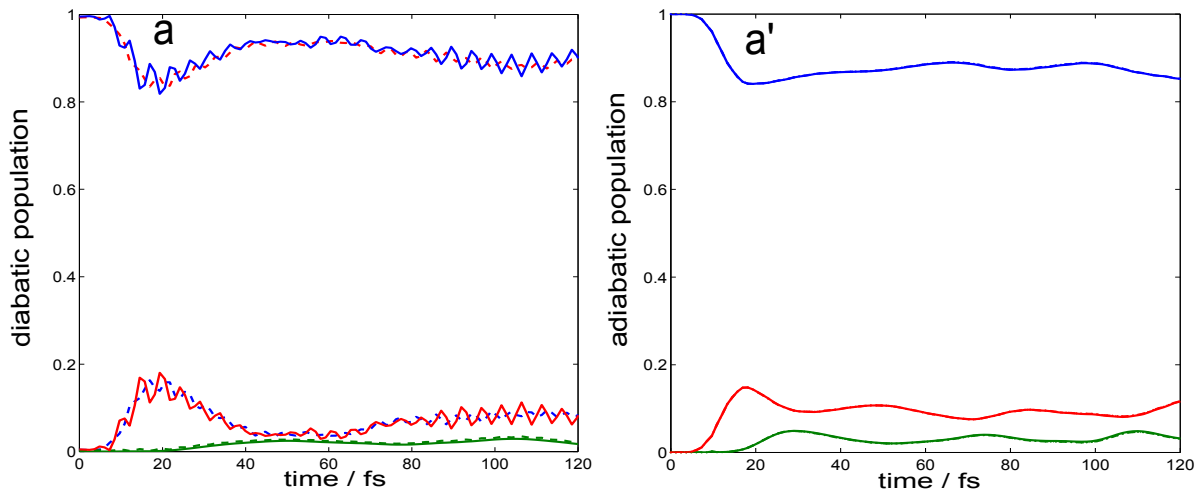


Figure 5.27.: Panels (a) and (a') show the diabatic and adiabatic populations for the cut with  $r \approx 0.8 \text{ \AA}$ , respectively. The wavepacket initially localized on the left adiabatic potential well is shown in solid lines and the one localized on the right in dashed lines. Here, the population of  $S_0$  is depicted in blue lines,  $S_1$  in green lines and  $S_2$  in red lines. The laser pulse parameters are defined in Section 5.8.

Figure 5.2(c) shows the asymmetry of the diabatic potentials for  $r \approx 1.0$  Å. This asymmetry is larger than for  $r \approx 0.8$  Å. This is reflected in the diabatic populations shown in Fig.5.28(a). The diabatic populations of the syn- and anti-forms differ already at  $t=0$ , where  $P^{0,d} \approx 1$ , while the value of  $P^{2,d}$  is only approximately 0.86. The populations of  $S_1$  in both cases are almost identical, this due to the fact that  $W_{11}$  is almost symmetric, as shown in Fig.5.2. The diabatic populations show large differences between  $P^{0,d}$  for the syn-form and  $P^{2,d}$  for the anti-form, and vice versa, because  $W_{00}$  and  $W_{22}$  are not symmetric. Nevertheless, the adiabatic populations of syn- and anti-form are identical, as shown in Fig.5.28(a').

In conclusion, the asymmetry of the diabatic potential leads to differences between the wavepacket dynamics of the syn- and anti-form of  $C_5H_4NH$  in the diabatic representation. Nevertheless, after back-transformation from the diabatic to the adiabatic picture, the time-dependent populations are the same for both indistinguishable cases. The diabatic picture is a mathematical tool for numerical propagation, while the adiabatic representation provide physical meaningful results.

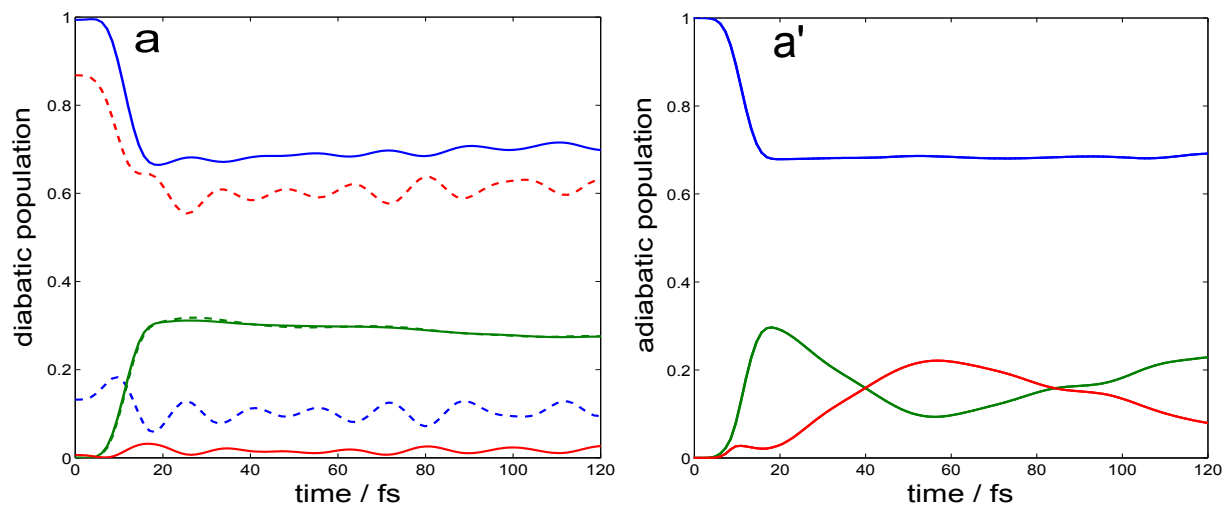


Figure 5.28.: Panels (a) and (a') show the diabatic and adiabatic populations for the cut with  $r \approx 1.0$  Å, respectively. The wavepacket initially localized on the left potential well is shown in solid lines and the one localized on the right in dashed lines. Here, the population of  $S_0$  is depicted in blue lines,  $S_1$  in green lines and  $S_2$  in red lines. The laser pulse parameters are defined in Section 5.8.

## 5.11. Conclusion

In this chapter the effect of the IREPs of the NACTs and transition dipole moments on the photo-induced nuclear dynamics has been investigated. Molecular symmetry affects nuclear dynamics whenever different electronic states are coupled. The coupling can be either internal via the NACTs or due to an external field via the transition dipole moments. To demonstrate the effect of molecular symmetry, the photo-excitation and subsequent nuclear dynamics in three coupled states of the model system  $C_5H_4NH$  have been considered. The radiation-less decay has been simulated for two cases in which the NACTs and transition dipole moments have the same absolute values, and the only difference is their IREPs. In both cases, the quantization rules for the NACTs and the symmetry rules derived in Chapter 4 are obeyed. The time-dependent populations of the electronic states show that the IREPs have significant effects on the photo-induced nuclear dynamics. Also, the calculated angular expectation values which describe the dispersion of the torsional wavefunction support this finding. The quantum chemistry methods usually provide only the absolute values of quantities like the NACTs and transition dipole moments. In this investigation, the importance of the IREPs of these quantities for nuclear dynamics calculation has been demonstrated. Also the results show that the radiation-less decay to the electronic ground states is strongly influenced by the symmetry of the initial nuclear state. Since the symmetry of the initial torsional wavefunction is determined by the nuclear spin of the molecule via the anti-symmetry principle,  $C_5H_4NH$  is also a promising candidate for the investigation of nuclear spin selective nuclear dynamics [50, 136].

The results discussed above have been obtained by quantum dynamics simulations where  $\delta$ -pulse excitation is considered as well as for excitations by laser pulses with finite durations. Taking into account the interaction between the molecule and the electric field explicitly also requires quantum chemical calculations of the dipole and transition dipole moments. It was shown in this Chapter and discussed further in Appendix B, that some of the quantum chemical results for the transition dipole moments are in contradiction to the assignment of the IREPs from Chapter 4. This disagreement has to still to be solved.

Furthermore, the photo-induced dynamics of the syn- and anti-forms of  $C_5H_4NH$  have been investigated in this Chapter. The two forms are indistinguishable and must show the same photochemistry. In the diabatic picture, due to the asymmetry of the diabatic potentials, syn- and anti-forms of  $C_5H_4NH$  show different radiation-less decay. However, in the adiabatic picture, the time-dependent populations of the electronic states are identical for both forms, as they should. We therefore emphasize that the diabatic picture should be viewed only as a mathematical tool for numerical propagation while the adiabatic picture will provide physical meaningful results.



## 6. Summary

In this study, I address the following questions: Does the molecular symmetry imposes constraints on conical intersections and non-adiabatic coupling terms (NACTs) with respect to symmetry-adapted coordinates? Does the corresponding irreducible representations (IREPs) of the NACTs influence photochemical processes related to the conical intersections? To tackle these problems, three fields of research are combined: quantum chemistry, theory of molecular symmetry, and molecular dynamics. This provides better understanding of the role of conical intersections and the related non-adiabatic coupling terms on the dynamics of transitions between different potential energy surfaces in molecules.

For these investigation, the cis-trans isomerization of the model system  $C_5H_4NH$  by torsion of the H-atom around the CN axis is proposed (Fig.4.1). The conical intersections of  $C_5H_4NH$  have been determined by Prof. Zilberg with help of the Longuet-Higgins sign change theorem. The resulting stationary structures have been assigned according to the IREPs of the local molecule point group [71].

This work provides an extension of these symmetry assignments, from the IREPs for local molecular point groups to the global molecular symmetry (MS) group. This opens the door to investigations of molecular properties beyond Born-Oppenheimer in global molecular domains, e.g. mediated by large amplitude motions such as torsion. We discovered several important properties of the CIs and the related NACTs with respect to molecular symmetry-adapted coordinates. For example, if the quantum chemistry calculations of the adiabatic potential energy surfaces have localized one CI between two electronic states, then one can apply the symmetry operations of the MS group in order to generate a complete set of MS-adapted CIs. These global properties can not be derived by pure quantum chemistry, they are a result of its combination with global MS groups.

One of the goals of this study is the determination the IREPs of the NACTs. For this purpose, the PESs and NACTs have been calculated by using an ab initio method of quantum chemistry (CASSCF with cc-pVDZ(10,9)), see Section 4.3 and 4.4. Close to a conical intersection between two electronic states, the corresponding NACT is very large and it decreases rapidly to approximately zero where the gap between the potentials increases. In order to determine the IREPs of NACTs, we derived two theorems (4.14)

and (4.17). These relate the IREPs of different NACTs to each other, e.g. theorem (4.14) implies that one can assign the IREPs of all the NACTs with respect to symmetry-adapted coordinates from the IREPs of a single NACTs for the same electronic states  $i$  and  $j$ , while theorem (4.17) imposes a condition on the IREPs of the NACTs between different electronic states. These two theorems in combination with the quantization rules (4.22), pole property (4.24) and switching property (4.26) were applied to determine the IREPs of the NACTs. By assigning the IREPs of NACTs, we discovered several "global" properties, such as the pattern of the sign of the peak values of the NACTs close to the set of MS-adapted CIs, and the nodal patterns of the NACTs, as shown in Section 4.4.

In Section 4.5, we calculated the matrices for adiabatic-to-diabatic transformation (ADT), based on the MS-adapted NACTs for molecular torsion. In the limit of a torsion by  $2\pi$ , these matrices approaches the so-called topological matrices  $\mathbf{D}$  which have to satisfy a quantization rule, i.e. they must be diagonal, with diagonal elements equal to 1 or -1 where the number of -1's must be even [3]. The fulfilment of the quantization rules can be viewed as a test for self-consistency to confirm the results for all the NACTs and the CIs of the three electronic states  $S_0$ ,  $S_1$  and  $S_2$  of  $C_5H_4NH$ .

In Chapter 5, we addressed the second question proposed in the beginning of this study, i.e. the IREPs of the NACTs influence photochemical processes related to the conical intersections? We investigate the effect of the IREPs of the NACTs and transition dipole moments on nuclear dynamics in the framework of quantum dynamical simulations using the split operator method implemented in program package "wavepacket" [134]. The photo-excitation with subsequent nuclear dynamics on three coupled electronic state of  $C_5H_4NH$  serve as model. To achieve this goal, we proposed different scenarios with same absolute values of the NACTs and transition dipole moments but with different sign depending on the IREPs, see Section 5.2. The scenarios fulfil the quantization rule and other symmetry properties. In the first part of this chapter, we assume that the transition dipole moments are constant in the Frank-Condon region (Condon approximation), but the IREPs of the transition dipole moments are taken into account, see Section 5.5. These the simulation are carried out by considering vertical excitation with a  $\delta$ -pulse. We show that the radiation-less decay to the electronic ground state is strongly influenced by the IREPs of the initial nuclear state. Since the IREPs of the initial torsional wavefunction is determined via the anti-symmetry principle by the nuclear spin of the molecule [50, 136], it must be either symmetric or anti-symmetric. The calculated adiabatic populations of three coupled states and probability densities show differences in the radiation-less decay between symmetric and anti-symmetric initial wavefunction, the effects of nuclear spins on photo-induced nuclear dynamics. Furthermore, in Section 5.5 we investigate the effect of the IREPs of the NACTs, dipole and transition dipole moments on radiation-less decay. The photo-induced dynamics show significant differences between the two scenarios, which can be observed in the time-dependent population of the electronic states, probability

densities, and in the angular expectation values which describe the dispersion of the torsional wavefunctions. The results show the importance of the molecular symmetry for a correct description of the nuclear dynamics.

In the second part of chapter 5, the photo-induced torsional dynamics of  $C_5H_4NH$  is investigated by taking into account the interaction between the molecule and the electric field explicitly, also considering that the dipole and transition dipole moments depend strongly on the torsion angle, beyond the condon approximation. The two scenarios which have been proposed in the first part show differences in the radiation-less decay due to symmetry effects. It is shown that the effect of IREPs of the NACTs, dipole and transition dipole moments on radiation-less decay can also be observed also if the interaction with a laser pulse and the torsional dependence of the transition dipole moments are taken into account. Here, we note a contradiction between the quantum chemical results and the symmetry assignment presented in Chapter 4. In the Appendix, we discuss a possible solution which has to be in the future investigated.

Furthermore, the photo-induced dynamics of the syn- to anti-form of  $C_5H_4NH$  is also investigated. The two forms are indistinguishable and must show the same photochemistry. In the diabatic picture, due to the asymmetry of the diabatic potentials, the syn- and anti-forms of  $C_5H_4NH$  show different radiation-less decays. However, in the adiabatic picture, the time-dependent populations of the electronic states are identical for both forms, as they should. We therefore emphasize that the diabatic picture should be viewed only as a mathematical tool for numerical propagation while the adiabatic picture will provide the physical meaningful results.

In this study, we considered a model with one nuclear degree of freedom for a proof of principle that the IREPs of the NACTs, dipole and transition dipole moments affect non-adiabatic nuclear dynamics. In future studies, more realistic models including several nuclear degrees of freedom will have to be considered in order to investigate how the effect of molecular symmetry can be revealed in experiments. Since the IREPs of the initial torsional wavefunction is determined by the nuclear spin of the molecule via the anti-symmetry principle [50, 136],  $C_5H_4NH$  is also a promising candidate for the investigation of nuclear spin selective nuclear dynamics.





# A. Appendix A

The z-components of the transition dipole moments between electronic states  $i$  and  $j$  where  $i \neq j$ , is calculated via

$$\mu_z^{i,j} = \langle \psi_{el}^i(\phi) | \hat{\mu}_z | \psi_{el}^j(\phi) \rangle. \quad (\text{A.1})$$

The transition dipole moments  $\mu_z^{i,j}$  well as the NACTs of  $\text{C}_5\text{H}_4\text{NH}$  must transform according to the IREPs of  $\text{C}_{2v}(\text{M})$ . In particular, we have shown in Section 5.3 that

$$\Gamma(\mu_z^{i,j}) = \Gamma(\tau_\phi^{i,j}) \times A_2 \quad (\text{A.2})$$

The resulting IREPs of the transition dipole moments are summarized in Tabel 5.1 for the two cases, i.e. case I and case II, discussed in Chapter 5.

As we have seen in Fig. 5.19, the quantum chemical data for the transition dipole moments  $\mu_z^{0,2}$  for  $r \approx 1.0 \text{ \AA}$  seems to be in contradiction to the IREPs required in case I. Therefore, the transition dipole moments are calculated for additional values of  $r$ . Fig.A.1 shows  $\mu_z^{i,j}$  for  $r \approx 0.8 \text{ \AA}$  (a and a'),  $r \approx 0.9 \text{ \AA}$  (b and b'),  $r \approx 1.0 \text{ \AA}$  (c and c'),  $r \approx 1.1 \text{ \AA}$  (d and d'),  $r \approx 1.2 \text{ \AA}$  (e and e') for case I (left column) and case II (right column).

For case I, the transition dipole moments for all cases except  $\mu_z^{0,2}$  for  $r \approx 1.0 \text{ \AA}$  (green curve in Fig.A.1(c)) are in accordance with Eq.(A.2). In particular,  $\mu_z^{0,2}$  for  $r \approx 1.2 \text{ \AA}$  (green curve in Fig.A.1(e)) changes smoothly from positive to negative values around  $\phi = \pi/2$ . Since  $\mu_z^{i,j}(\phi)$  must have the same IREPs for all values of  $r$ , this suggest that  $\mu_z^{i,j}(\phi)$  for  $r \approx 1.0 \text{ \AA}$  is a limiting case where the smooth transition which is observed for  $r \approx 1.2 \text{ \AA}$  becomes a sudden jump. A similar argument can be applied also to case II. Here, all functions  $\mu_z^{i,j}(\phi)$  are in accordance with Eq.(A.2) except  $\mu_z^{1,2}$  for  $r \approx 1.2 \text{ \AA}$  (red lines in Fig.A.1(e')). Here, the  $\mu_z^{1,2}$  is supposed to change its sign at  $\phi = \pm\pi/2$ , which is not supported by the quantum chemical data. However, a smooth transition from negative to positive values can be observed for  $\mu_z^{1,2}(\phi)$  for  $r \approx 1.0 \text{ \AA}$  (Fig. A.1(c'), red line). Since  $\mu_z^{1,2}$  must have the same symmetry for all  $r$ , this might became a sudden jump at  $r \approx 1.2 \text{ \AA}$ .

Concluding, it seems that the quantum chemical calculation of the transition dipole moments lead to a contradiction to the symmetry assignment from Chapter 4. The transition from a smooth sign change to a sudden jump is a possible explanation which has to be

explored by further investigation.

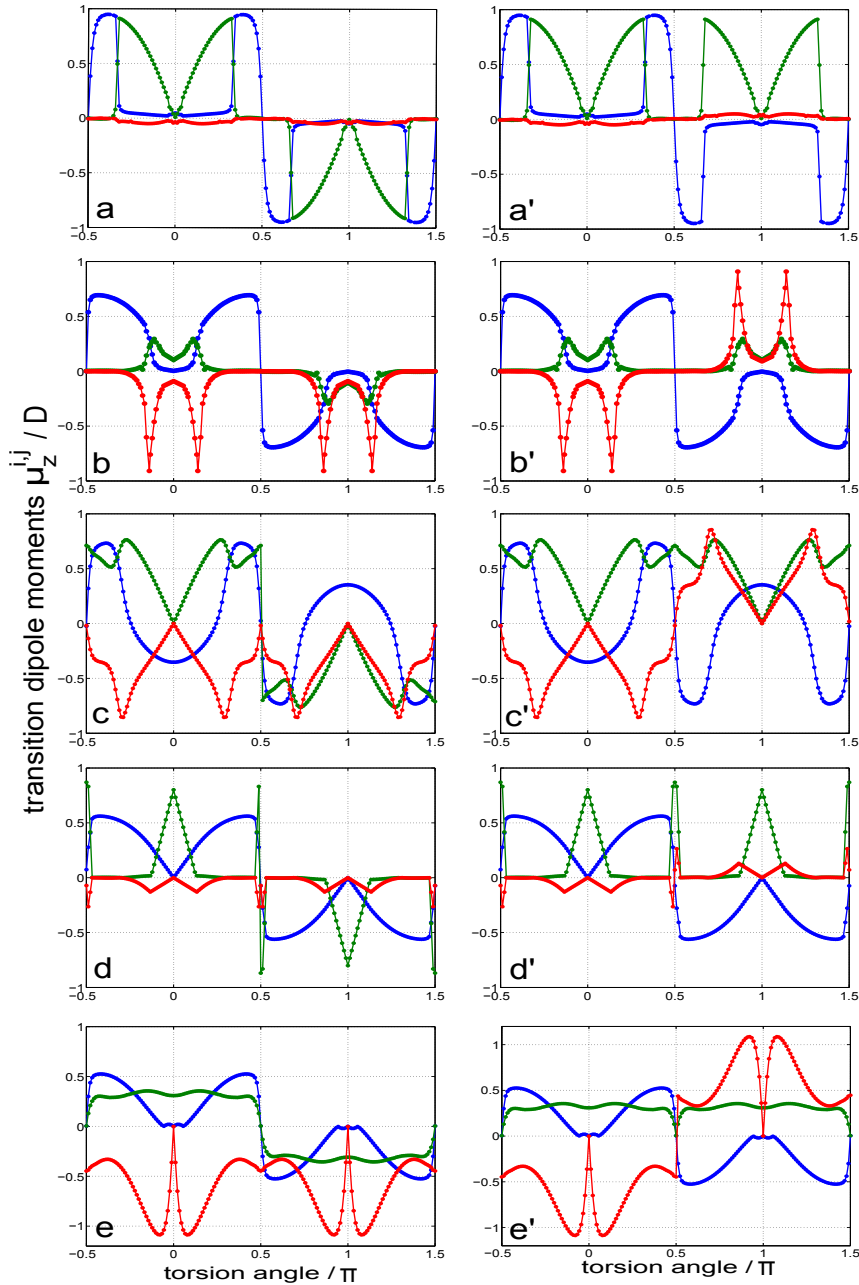


Figure A.1.: The transition dipole moments  $\mu_z^{i,i}$  for different values of  $r$ , i.e.  $r \approx 0.8 \text{ \AA}$  (a, a')  $r \approx 0.9 \text{ \AA}$  (b, b')  $r \approx 1.0 \text{ \AA}$  (c, c')  $r \approx 1.1 \text{ \AA}$  (d, d')  $r \approx 1.2 \text{ \AA}$  (e, e'). The two cases discussed in Chapter 5 are shown, i.e. case I (left column) and case II (right column). The transition dipole moments  $\mu_z^{0,1}$ ,  $\mu_z^{0,2}$  and  $\mu_z^{1,2}$  are shown in blue, green and red lines, respectively.

# Bibliography

- [1] Trommsdorff, H., *Ann. Chem. Pharm.* (**1834**), 11.
- [2] Schinke, R., *Photodissociation Dynamics*, Cambridge University Press, Cambridge, (**1993**).
- [3] Baer, M., *Beyond Born-Oppenheimer: Electronic Nonadiabatic Coupling Terms and Conical Intersection*. John Wiley & Sons, Hoboken (**2006**).
- [4] Renner, R., *Z. Physik.* (**1934**), 92, 172.
- [5] Teller, E., *J. Phys. Chem.* (**1937**), 41, 109.
- [6] Jahn, H.A., Teller, E., *Stability of Polyatomic Molecules in Degenerate Electronic States. I. Orbital Degeneracy*. *Proc. R. Soc. Lond. A . Mathematical and Physical Science*, (**1937**), 161, 220.
- [7] Landau, L., *Phys. Sov. Union* (**1932**), 2, 46.
- [8] Zener, C., *Proc. Roy. Soc. of London A* (**1932**), 137, 696.
- [9] Köppel, H., Cederbaum, L.S., Domcke, W., Shaik, S.S, *Angew. Chem. Int. Ed.* (**1983**), 22, 210.
- [10] Domcke, W., Yarkony, D.R., Köppel, H., *Conical Intersections: Electronic Structure, Dynamics and Spectroscopy*. World Science, Singapore. (**2004**).
- [11] Abrol, R., Kuppermann, A., (**2002**), 116, 1035.
- [12] Sobolewski, A.L., Domcke, W., *Europhysics News* (**2006**), 37, 20.
- [13] Lönn, U., *Radiation Research* (**1984**), 99, 659.
- [14] Schultz, T., Samoylova, E., Radloff, W., Hertel, I.V., Sobolewski, A.L., Domcke, W., *Science* (**2004**), 306, 1765.
- [15] Herzberg, G., Longuet-Higgins, H.C., *Discuss Faraday Soc.* (**1963**), 35, 77.
- [16] Longuet-Higgins, H.C., *Proc. R. Soc. London, Ser. A* (**1975**), 344, 147.

- [17] Zilberg, S., Haas, Y., *Adv. Chem. Phys.* (**2002**), 124, 433.
- [18] Zilberg, S., Haas, Y., *J. Phys. Chem. A* (**2003**), 107, 1222.
- [19] Mahapatra, S., Köppel, H., Cederbaum, L.S., Stampfus, P., Wenzel, W., *Chem. Phys.* (**2000**), 259.
- [20] Mebel, A.M., Baer, M., Lin, S.H., *J. Chem. Phys.* (**2000**), 112, 10703.
- [21] Sobolewski, A.L., Domcke, W., *Chem. Phys.* (**2001**), 259, 181.
- [22] Yarkony, D.R., *J. Phys. Chem. A.* (**2001**), 105, 6277.
- [23] Domcke, W., Stock, G., *Adv. Chem. Phys.* (**1997**), 100, 1.
- [24] Köppel, H., Domcke, W., Cederbaum, L.S., *Adv. Chem. Phys.* (**1984**), 57, 59.
- [25] Worth, G.A., Cederbaum, L.S., *Annu. Rev. Phys. Chem.* (**2004**), 55, 127.
- [26] Mahapatra, *Acc. Chem. Res.* (**2009**), 42, 1004.
- [27] Thiel, A., Köppel, H., *J. Chem. Phys.* (**1999**), 110, 9371.
- [28] Köppel, H., Gronki, J., Mahapatra, S., *J. Chem. Phys.* (**2001**), 115, 2377.
- [29] Köppel, H., *Faraday. Discuss.* (**2004**), 127, 35.
- [30] Hofmann, A., de Vivie-Riedle, R., *J. Chem. Phys.* (**2000**), 112, 5054; *Chem. Phys. Lett.* (**2001**), 34, 299.
- [31] de Vivie-Riedle, R., Hofmann, A., Domcke, W., Yarkony, D.R., Köppel, H., Eds. *Conical Intersections: Electronic Structure, Dynamics and Spectroscopy*, Singapore: World Sci. (**2004**).
- [32] *MOLPRO is a package of abinitio programs written by* Werner, H-J., Knowles, P.J., Lindh, R., Manby, F.R., Schütz, M., Celani, P., Korona, T., Rauhut, G., Amos, R.D., Bernhardsson, A., Berning, A., Cooper, D.L., Deegan, M.J.O., Dobbyn, A. J., Eckert, F., Hampel, C., Hetzer, G., Lloyd, A.W., McNicholas, S.J., Meyer, W., Mura, M.E., Nickla, A., Palmieri, P., Pitzer, R., Schumann, U., Stoll, H., Stone, A.J., Tarroni, R., Thorsteinsson, T.
- [33] Baer, M., *Chem. Phys. Lett.* (**1980**), 35, 112; *Mol. Phys.* (**1980**), 40, 1011.
- [34] Halász, G.J., Vibók, Á., Hoffman, D.K., Kouri, D.J., Baer, M., *J. Chem. Phys.* (**2007**), 126, 154309.
- [35] Meyer, H.D., Worth, G.A., *Theor. Chem. Acc.* (**2003**), 109, 251.

- [36] Hofmann, A., de Vivie-Riedle, R., *J. Inf. Recordings* (**2000**), 25, 397.
- [37] Kroes, G.J., vanHemert, M.C., Billing, G.D., Neuhauser, D., *J. Chem. Phys.* (**1997**), 107, 5757.
- [38] Schmidt, B., *Chem. Phys. Lett.* (**1999**), 301, 207.
- [39] Ben-Nun, M., Molnar, F., Lu, H., Phillips, J.C., Martinez, T.J., Schulten, K., *Faraday Discuss.* (**1999**), 110, 447.
- [40] Seidner, L., Domcke, W., *Chem. Phys.* (**1994**), 186, 27.
- [41] Hahn, S., Stock, G., *J. Phys. Chem.* (**2000**), 104, 1146.
- [42] Longuet-Higgins, H.C., *Mol. Phys.* (**1963**), 6, 445.
- [43] Bunker, P.R., Jensen, P., *Fundamentals of Molecular Symmetry*, Taylor & Francis, (**2004**).
- [44] Hougen, J.T., *J. Chem. Phys.* (**1962**) 37, 1433; (**1963**) 39, 358.
- [45] Levine, B.J., Martinez, T.J., *Annu. Rev. Phys. Chem.* (**2007**), 58, 613.
- [46] Fennimore, A.M., Yuzvinsky, T.D., Han, W.-Q., Fuhrer, M.S., Cumings, J., Zettl, A., *Nature* (**2003**), 424, 408.
- [47] Demirok, U., Laocharoensuk, R., Manesh, K.M., Wang, J., *Angew. Chemie* (**2008**), 47, 9349.
- [48] Ross, K.T., De Silva, H., Richard, A., *Nature* (**1999**), 401, 150.
- [49] Grohmann, T., Deeb, O., Leibscher, M., *Chem. Phys.* (**2007**), 338, 252.
- [50] Deeb, O., Leibscher, M., Manz, J., von Muellern, W., Seideman, T., *ChemPhysChem* (**2007**), 8, 322.
- [51] Szabo, A., Ostlund, N.S., *Modern Quantum Chemistry*. Dover Publications, Mineola. New York. (**1996**).
- [52] Born, M., Oppenheimer, R., *Ann. Phys.* (**1927**), 84, 457.
- [53] Roothaan, C.C.J., *Rev. Mod. Phys.* (**1951**), 23, 69.
- [54] Löwdin, P. O., *Adv. Chem. Phys.* (**1959**), 2, 207.
- [55] Jensen, F., *Introduction to Computational Chemistry*. John Wiley & Sons. (**1999**).
- [56] Slater, J.C., *Phys. Rev.* (**1930**), 36, 57.

- [57] Boys, S.F., Proc. R. Soc. London A. (1950), 200, 542.
- [58] Huzinaga, S., J. Chem. Phys. (1965), 42, 1293.
- [59] Rosenberg, B.J., Shavitt, I., J. Chem. Phys. (1975), 63, 2162.
- [60] Grimaldi, F., Lecourt, A., Moser, C., Int. J. Quantum Chem. (1967), 1, 153.
- [61] Roos, B.O., Taylor, P.R., Chem. Phys. (1980), 48, 157.
- [62] Smith, F.T., Phys. Rev. (1969), 179, 111.
- [63] Simah, D., Hartke, B., Werner, H.J., J. Chem. Phys. (1999), 111, 4523.
- [64] Hirsch, G., Buenker, R.J., Petrongolo, C., Mol. Phys. (1990), 70, 835.
- [65] Werner, H.-J., Meyer, W., J. Chem. Phys. (1981), 74, 5802.
- [66] Hendekovic, J., Chem. Phys. Lett. (1982), 90, 193.
- [67] Atchity, G.J., Ruedenberg, K., Theor. Chem. Acc. (1997), 97, 47.
- [68] Ruedenberg, K., Atchity, G.J., J. Chem. Phys. (1993), 99, 3799.
- [69] Baer, M., Chem. Phys. Lett. (1975), 35, 112.
- [70] Hirsch, G., Bruna, P.J., Buenker, R.J., Peyerimhoff, S.D., Chem. Phys. (1980), 45, 335.
- [71] Al-Jabour, S., Baer, M., Deeb, O., Leibscher, M., Manz, J., Xu, X., Zilberg, S., J. Phys. Chem. A. (2010) 114, 2991.
- [72] Fischer, E., Chem. Ber. (1984), 27, 2985.
- [73] Marston, C.C., Balint-Kurti, G.G., J. Chem. Phys. (1989), 91, 3571.
- [74] Stare, J., Balin-Kurt, G.G., J. Phys. Chem. (2003), 107, 7204.
- [75] Merzbacher, E., *Quantum Mechanics*, John Wiley & Sons, New York (1970).
- [76] Kosloff, D., Kosloff, R., J. Comput. Phys. (1983), 52, 35.
- [77] Bisseling, R.H., Kosloff, R., Manz, J., J. Chem. Phys. (1985), 83, 993.
- [78] Kosloff, R., Tal-Ezer, H., Chem. Phys. Lett. (1982), 89, 483.
- [79] Feit, M.D., Fleck, J.A., Steiger, A., J. Comput. Phys. (1982), 47, 412.
- [80] Feit, M.D., Fleck, J.A., J. Chem. Phys. (1983), 78, 301.

- [81] Alvarellos, J., Metiu, H., J. Chem. Phys. (1988), 88, 4957.
- [82] Bandrauk, A.D., Shen, H., J. Chem. (1992), 70, 555.
- [83] Bandrauk, A.D., Shen, H., J. Chem. Phys. (1993), 99, 1185.
- [84] Schwendner, P., Seyl, F., Schinke, R., Chem. Phys. (1997), 217, 233.
- [85] Tannor, D.J., *Introduction to Quantum Chemistry, A Time-Dependent Perspective*, University Science Book, California, (2007).
- [86] Tannor, D.J., Rice, S.A., J. Chem. Phys. (1985), 83, 5013.
- [87] Tannor, D.J., Kosloff, R., Rice, S.A., J. Chem. Phys. (1986), 85, 5805.
- [88] Paramonov, G.K., Savva, V.A., Phys. Lett. (1983), 97, 340; Barth, I., Lasser, C., J. Phys. B: At. Mol. Opt. Phys. (2009), 42, 235101.
- [89] Leforestier, C., Bisseling, R.H., Cerjan, C., Feit, M.D., Friesner, R., Guldberg, A., Hammerich, A., Jolicard, G., Karrlein, W., Meyer, H.-D, Lipkin, N., Roncero, O., Kosloff, R., J. Comput. Phys. (1991), 94, 59.
- [90] Holthaus, M., Just, B., Phys. Rev. (1994), 49, 1950.
- [91] Löwdin, P.O., J. Chem. Phys. (1950), 18, 365.
- [92] Shavitt, I., Mol. Phys. (1998), 94, 3.
- [93] Møller, C., Plesset, M.S., Phys. Rev. (1934), 46, 618.
- [94] Baer, M., *Theory of Chemical Reaction Dynamics*, CRC Press. (1985).
- [95] Baer, M., Alijah, A., Chem. Phys. Lett. (2000), 319, 489.
- [96] Baer, M., Chem. Phys. (2000), 259, 123.
- [97] Baer, M., Phys. Repts. (2002), 358, 75.
- [98] Slanina, Z., Adv. Quantum Chem. (1981), 13, 89.
- [99] Granovsky, A.A., PC GAMESS version 7.0,  
<http://classic.chem.msu.su/gran/games/index.html>.
- [100] Baer, M., Billing, G.D., *The Role of Degenerate States in Chemistry*. Adv. Chem. Phys. (2002), 124; Child, M.S., p. 1; Adhikari, S., Billing, G.D., p.143; Englman, R., Yahalom, A., p. 197; Kuppermann, A., Abrol, R., p. 323; Worth, G.A., Robb, M.A., p. 355.

- [101] Barbatti, M., Belz, S., Leibscher, M., Lischka, H., Manz, J., Chem. Phys. (2008), 350, 145.
- [102] Abe, M., Ohtsuki, Y., Fujimura, Y., Lan, Z., Domcke, W., J. Chem. Phys. (2006), 124, 224316.
- [103] Mead, C.A., Chem. Phys. (1980), 49, 23.
- [104] Wu, Y.M., Kuppermann, A., Chem. Phys. Lett. (1993), 201, 178; (1995), 235, 105.
- [105] Berry, M.V., Proc. R. Soc. London, Ser. A (1984), 392, 45.
- [106] Baer, M., Lin, S.H., Alijah, A., Adhikari, S., Billing, G.D., Phys. Rev. A. (2000), 62, 032506.
- [107] Alfalah, S., Belz, S., Deeb, O., Leibscher, M., Manz, J., Zilberg, S., J. Chem. Phys. (2009), 130, 124318.
- [108] Kuppermann, A., *Dynamics of Molecules and Chemical Reactions*; Wyatt, R. E., Zhang, Z. H., Eds. Marcel, New York (1996), p. 411.
- [109] Baer, R., Charutz, D.M., Kosloff, R., Baer, M., J. Chem. Phys. (1996), 105, 9141; Adhikari, S., Billing, G.D., J. Chem. Phys. (1999), 111, 40.
- [110] Baer, M., Vertesi, T., Halász, G.J., Vibók, Á., Suhai, S., Farad. Discuss.(2004), 127, 337; Halász, G.J., Vibók, Á., Suhai, S., Baer, M., J. Chem. Phys. (2005), 126, 134109.
- [111] Halász, G.J., Vibók, Á., Baer, R., Baer, M., J. Phys. A: Math. Theor. (2007), 40, F267.
- [112] Sadykov, R.G., Yarkony, D.R., J. Chem. Phys. (1998), 109, 20; Yarkony, D.R., J. Chem. Phys. (2001), 114, 2614.
- [113] Mead, C.A., Truhlar, D.G., J. Chem. Phys. (1982), 77, 6090; Mead, C.A., J. Chem. Phys. (1983), 78, 807.
- [114] Davidson, E.R., J. Am. Chem. Soc. (1977), 99, 397.
- [115] Barragan, P., Errea, L.F., Macias, A., Mendez, L., Riera, A., Lucas, J.M., Aguilar, A., J. Chem. Phys. (2004), 121, 11629; Sevryuk, M.B.; Rusin, L.Y., Cavalli, S., Aquilanti, V., J. Phys. Chem. A (2004), 108, 8731.
- [116] Englman, R., Vertesi, T., Phys. Lett. A (2006), 354, 196; Vertesi, T., Englman, R., J. Phys. B (2008), 41, 025102.



- [117] Amaran, S., Kumar, S., *J. Chem. Phys.* (**2008**), 128, 154325; Amaran, S., Kumar, S., Köppel, H., *J. Chem. Phys.* (**2008**), 128, 124305; Gomez-Carrasco, S., Aquado, A., Paniaqua, M., Roncero, O., *J. Chem. Phys.* (**2006**), 125, 104105.
- [118] Hu, C., Hirai, H., Sugino, O., *J. Chem. Phys.* (**2008**), 128, 144111; Hu, C., Hirai, H., Sugino, O., *J. Chem. Phys.* (**2007**), 127, 064103.
- [119] Gadea, X., Pellisier, M., *J. Chem. Phys.* (**1990**), 93, 545; Romero, T.; Aguilar, A., Gedeo, X., *J. Chem. Phys.* (**1999**), 110, 6219; Mozhayskiv, V.A., Babikov, D., Krylov, A.I., *J. Chem. Phys.* (**2006**), 124, 224309.
- [120] Abrahamsson, E., Groenenboom, G.C., Krems, R.V., *J. Chem. Phys.* (**2007**), 126, 184309; Rozgonyi, T., González, L., *J. Phys. Chem. A* (**2008**), 112, 5573.
- [121] Puzari, P., Sarkar, B., Adhikari, S., *J. Chem. Phys.* (**2004**), 121, 707; Sarkar, B., Adhikari, S., *J. Chem. Phys.* (**2006**), 124, 074101.
- [122] Godsi, P.O., Evenhuis, C.R., Collins, M., *J. Chem. Phys.* (**2006**), 125, 164321.
- [123] Kryachko, E.S., Varandas, A.J.C., *Int. J. Quantum Chem.* (**2002**), 89, 255; Kryachko, E.S., *Adv. Quantum Chem.* (**2003**), 44, 119; Varandas, A.J.C., Xu, Z.R., *Int. J. Quantum Chem.* (**2004**), 99, 385.
- [124] Levi, C., Halász, G.J., Vibók, Á., Bar, I., Zeiri, Y., Kosloff, R., Baer, M., *J. Chem. Phys.* (**2008**), 128, 244302; Levi, C., Halász, G.J., Vibók, Á., Bar, I., Zeiri, Y., Kosloff, R., Baer, M., *Int. J. Quantum Chem.* (**2009**), 109, 2482.
- [125] Haas, Y., Cogan, S., Zilberg, S., *Int. J. Quantum Chem.* (**2005**), 102, 961.
- [126] Roos, B.O., *Adv. Chem. Phys.* (**1987**), 69, 399.
- [127] Mebel, A.M., Baer, M., Lin, S.H., *J. Chem. Phys.* (**2001**), 114, 5109.
- [128] Mebel, A.M., Yahalom, A., Englman, R., Baer, M., *J. Chem. Phys.* (**2001**), 115, 3673.
- [129] Soldan, P., *J. Meth. Chem.* (**1996**), 20, 331.
- [130] Hougen, J.T., Dekoven, B.M., *J. Mol. Spectrosc.* (**1983**), 98, 375.
- [131] Poisson, L., Raffael, K.D., Soep, B., Mestdagh, J.M., Buntinx, G., *J. Am. Chem. Soc.* (**2006**), 126, 10.
- [132] Poisson, L., Roubin, P., Coussan, S., Soep, B., Mestdagh, J.M., *J. Am. Chem. Soc.* (**2008**), 130, 10.

- 
- [133] Tishchenko, O., Truhlar, D.G., Ceulemans, A., Nguen, M.T., JACS. (2008), 130, 7000.
- [134] Schmidt, B., Lorenz, U., WAVEPACKET 4.5, A program package for quantum-mechanical wavepacket propagation and time-independent spectroscopy, (2008), see <http://wavepacket.sourceforge.net>.
- [135] Bonačić-Koutecký, V., Bruckmann, P., Hiberty, P., Koutecký, J., Leforestier, C., Salem, L., Angew. Chem. Int. Ed. (1975), 14, 575.
- [136] Belz, S., Grohmann, T., Leibscher, M., J. Chem. Phys. (2009), 131, 034305.
- [137] Holmegaard, L., Hansen, J.L., Kalhøj, L., Kragh, S.L, Stapelfeldt, H., Filsinger, F., Küpper, J., Meijer, G., Dimitrovski, D., Abu-Samha, M., Martiny, C.P.J., Madsen, B., Nature Phys. (2010), 6, 428.